SÃO PAULO STATE UNIVERSITY
"JÚLIO DE MESQUITA FILHO"
SCHOOL OF ENGINEERING, SÃO JOÃO DA BOA VISTA

ELÍGIA SIMIONATO

Electromagnetic Analysis and Optimization of a Coaxial Horn Antenna Operating at Millimetre Wave Frequencies

São João da Boa Vista
2023

Elígia Simionato

Electromagnetic Analysis and Optimization of a Coaxial Horn Antenna Operating at Millimetre Wave Frequencies

Undergraduate thesis presented to the Undergraduate Course Council in Electronics and Telecommunications Engineering of the School of Engineering in São João da Boa Vista, São Paulo State University, as part of the requirements for obtaining the Bachelor of Science degree in Electronics and Telecommunications Engineering.

Advisor: Professor Rafael Abrantes Penchel, PhD

São João da Boa Vista
2023

S589e

Simionato, Elígia
Electromagnetic Analysis and Optimization of a Coaxial Horn Antenna Operating at Millimetre Wave Frequencies / Elígia Simionato. -- São João da Boa Vista, 2023
68 p. : il., tabs., fotos

Trabalho de conclusão de curso (Bacharelado - Engenharia de Telecomunicações) - Universidade Estadual Paulista (Unesp), Faculdade de Engenharia, São João da Boa Vista
Orientador: Rafael Abrantes Penchel

1. Telecommunications. 2. Millimeter wave devices. 3. Microwave antennas. I. Título.

Sistema de geração automática de fichas catalográficas da Unesp. Biblioteca da Faculdade de Engenharia, São João da Boa Vista. Dados fornecidos pelo autor(a).

Essa ficha não pode ser modificada.

UNIVERSIDADE ESTADUAL PAULISTA “JÚLIO DE MESQUITA FILHO”
FACULDADE DE ENGENHARIA - CÂMPUS DE SÃO JOÃO DA BOA VISTA
GRADUAÇÃO EM ENGENHARIA ELETRÔNICA E DE TELECOMUNICAÇÕES

TRABALHO DE CONCLUSÃO DE CURSO

ELECTROMAGNETIC ANALYSIS AND OPTIMIZATION OF A COAXIAL HORN ANTENNA OPERATING AT MILLIMETRE WAVE FREQUENCIES

Aluna: Elígia Simionato
Orientador: Prof. Dr. Rafael Abrantes Penchel

Banca Examinadora:

- Rafael Abrantes Penchel (Orientador)
- Ivan Aritz Aldaya Garde (Examinador)
- Guilherme Simon da Rosa (Examinador)

A ata da defesa com as respectivas assinaturas dos membros encontra-se no prontuário do aluno (Processo nº 256/2023)

São João da Boa Vista, 15 de dezembro de 2023

To the memory of Edevino Simionato

ACKNOWLEDGEMENTS

I would like to express my gratitude to everyone who, in any form, encouraged and supported my research and education, and collaborated on the project meticulously organized hereinafter.

To my advisor, Professor Rafael Abrantes Penchel, for guiding me through my research, providing support throughout the five years of my undergraduate studies, and offering opportunities beyond my imagination when I initially started my scientific initiation.

To Professors José Augusto de Oliveira and Ivan Aldaya, who, alongside Professor Rafael, kindly welcomed me to the Center for Advanced and Sustainable Technologies, and encouraged me to embark on my research career.

To Professor Guilherme Simon da Rosa, for the meticulous and masterful efforts dedicated to the measurements of the device resulting from this work.

To Ana Júlia Nora and Marcela Thaiane Pires, for the friendship and companionship throughout many endeavours during our undergraduate studies.

To my family, for always encouraging my pursuit of higher education.

To the team at Biofabris Institute, for conducting the fabrication process used in this work, and to Professor Julian Avila, who collaborated on the studies for the fabrication process.

And finally, I would like to thank São Paulo Research Foundation (FAPESP) for funding this project.

This work received support from the following entity:
Grant #2019/20209-8, São Paulo Research Foundation (FAPESP)
Grant #2020/09889-4, São Paulo Research Foundation (FAPESP)

The opinions, hypotheses, conclusions, or recommendations expressed in this material are the responsibility of the authors and do not necessarily reflect the views of FAPESP.

ABSTRACT

This undergraduate thesis is contextualized by the recent expansion of mobile communication systems towards operation at millimetre wave frequencies. This expansion, proposed as a means to provide greater spectrum availability and support multiple current and emerging use cases, has encouraged research into the development of antennas and devices capable of overcoming the challenges of operating at extremely high frequencies. One of the proposed antennas capable of providing the sought-after wideband behaviour and omnidirectional high-gain characteristic is the dual-reflector antenna fed by a coaxial horn. This work aims to conduct electromagnetic analyses and optimizations of a coaxial horn operating in the Ka band (26 GHz to 40 GHz), a portion of the spectrum being allocated worldwide for future international mobile telecommunications. Ultimately, this work will evaluate the design of two coaxial horn models: the standard coaxial horn, serving as a practical prototype of the device previously presented in the literature, utilizing the same dimensions but incorporating essential elements to enable its fabrication without compromising performance; and the shaped coaxial horn, an optimized version aiming for a broader bandwidth and a more uniform radiation pattern. This work will also report the fabrication of the standard coaxial horn through additive manufacturing, and its characterization, from which measurements revealed a relative impedance bandwidth of 79% and a peak realizable gain of 11.53 dBi.

KEYWORDS: Telecommunications. Millimeter wave devices. Microwave antennas.

RESUMO

Este trabalho de conclusão de curso está contextualizado pela recente expansão da operação dos sistemas de comunicação móvel para frequências de ondas milimétricas. Essa expansão, proposta como uma forma de proporcionar maior disponibilidade de espectro e apoiar diversos casos de uso atuais e emergentes, incentivou pesquisas para o desenvolvimento de antenas e dispositivos capazes de superar os desafios de operar em frequências extremamente elevadas. Uma das antenas propostas capaz de fornecer o comportamento banda larga desejado e a característica de alto ganho omnidirecional é a antena duplo-refletora alimentada por uma corneta coaxial. Este trabalho visa realizar análises eletromagnéticas e otimizações de uma corneta coaxial operando na banda Ka (26 GHz a 40 GHz), uma parte do espectro que vem sendo alocada mundialmente para futuros sistemas de telecomunicações móveis internacionais. Em suma, este trabalho avaliará o projeto de dois modelos de cornetas coaxiais: a corneta coaxial padrão, servindo como um protótipo prático do dispositivo previamente apresentado na literatura, utilizando as mesmas dimensões, mas incorporando elementos essenciais para viabilizar sua fabricação sem comprometer o desempenho; e a corneta coaxial modelada, uma versão otimizada visando uma largura de banda mais ampla e um diagrama de radiação mais uniforme. Este trabalho também relatará a fabricação da corneta coaxial padrão por manufatura aditiva e sua caracterização, a partir da qual as medições revelaram uma largura de banda de impedância relativa de 79% e um ganho realizável máximo de 11,53 dBi.

PALAVRAS-CHAVE: Telecomunicações. Dispositivos de ondas milimétricas. Antenas de microondas.

LIST OF FIGURES

LIST OF TABLES

LIST OF ABBREVIATIONS AND ACRONYMS

3GPP	Third Generation Partnership Project
dB	Decibels
dBi	Decibels relative to isotropic radiator
ETSI	European Telecommunications Standards Institute
FEM	Finite Element Method
FeMBB	Further Enhanced Mobile Broad Band
GA	Genetic Algorithm
HFSS	High Frequency Structure Simulator
IMT	International Mobile Telecommunications
ITU	International Telecommunications Union
L-PBF	Laser Powder Bed Fusion
MBBLL	Mobile Broad Band and Low Latency
mLLMT	Massive Low-Latency Machine-Type Communications
mm-wave	Millimetre Wave
PEC	Perfect Electric Conductor
PMC	Perfect Magnetic Conductor
TEM	Transverse Electromagnetic
umMTC	Ultra-Massive Machine-Type Communications
WRC	World Radiocommunication Conference

CONTENTS

1 INTRODUCTION

1.1 THE USE OF MILLIMETRE WAVE FREQUENCIES IN THE ADVANCEMENT OF MOBILE COMMUNICATIONS

Over the past few decades, mobile communications have played a crucial role in both technical evolution and economic development (FERNÁNDEZ-ARDÈVOL, 2011; ITU, 2015). Beyond its technological and economic impact, the advancement of mobile communications significantly influences social development. Since our societies heavily rely on communication, the widespread availability of this specific communication tool affects various social aspects (FERNÁNDEZ-ARDÈVOL, 2011). Mobile communications, therefore, represent a multifaceted topic, and the ongoing evolution of mobile communication technologies positively impacts other areas of high relevance, laying the groundwork for future societal foundations.

This interconnected landscape is evident in the recent surge of mobile traffic. As mobile devices become increasingly indispensable for communication, entertainment, and productivity, the sheer volume of data transferred over mobile networks has surged dramatically. From the beginning of this study in 2019 to its current presentation in 2023, mobile data traffic has grown from around 32 Exabytes (EB) per month to over 134 EB/month, a remarkable 320% growth (ERICSSON, 2019; ERICSSON, 2023). This surge underscores not only the growing reliance on mobile communication, but also its pivotal role in shaping our interconnected world. The increase in mobile traffic serves as a tangible manifestation of the societal, technical, and economic transformations driven by the ample presence of mobile communications.

In response to this surge, institutions like the International Telecommunications Union (ITU) and the European Telecommunications Standards Institute (ETSI), through the Third Generation Partnership Project (3GPP), began laying the groundwork for current and upcoming advancements (ITU, 2017; ETSI, 2019). They introduced daring requirements for the next generations of mobile communications (5G, 6G, and beyond) as a path to support countless emerging use cases with a high variety of applications and variability of their performance, delivered across a fully heterogeneous environment and across a wide range of devices (NGMN ALLIANCE, 2015). Figure 1(a) exemplifies 5G and 6G requirements compared to each other and to the more widely available 4G, while Figure 1(b) illustrates the use cases envisioned for current and emerging applications.

As illustrated in Figure 1(b) different configurations were introduced in 5G, each involving trade-offs on latency, energy consumption, costs, hardware complexity, throughput, and end-to-end reliability. In contrast, 6G will be developed to jointly meet rigorous network demands and requirements, including Further enhanced Mobile Broad Band (FeMBB), ultra-massive Machine-Type Communications (umMTC), Mobile Broad Band and Low Latency (MBBLL), and massive Low-Latency Machine-Type communications (mLLMT) (ALSABAH et al., 2021; GIORDANI et al., 2020; ALWIS et al., 2021).

To meet the aforementioned requirements, carefully managing the frequency spectrum becomes a necessity (PI; KHAN, 2011). For presenting favourable propagation conditions, the sub-6GHz

Figure 1 – (a) Comparison between 4G, 5G and 6G requirements, and (b) envisioned usage scenarios for future International Mobile Telecommunications.

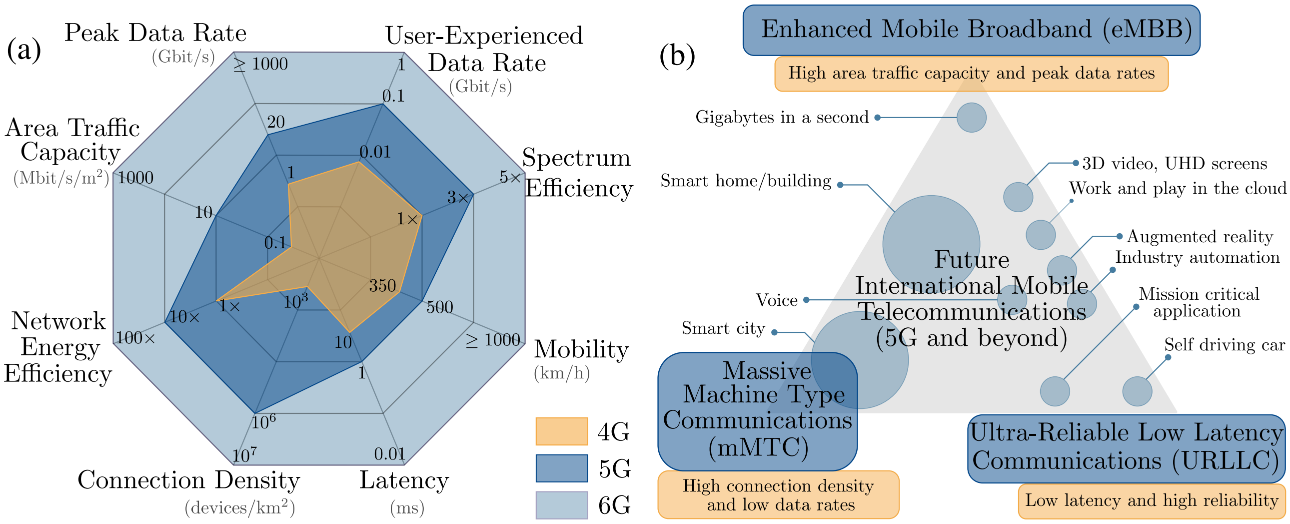

Source: Adapted from ITU (2015), Alwis et al. (2021), and Giordani et al. (2020)

frequencies are in high demand by mobile systems and other wireless services such as fixed, broadcasting and satellite communications (CHOUDHURY, 2015). As a result, sub-6GHz bands became unattractive for the development of innovative technology that is highly dependent on spectrum availability. The millimetre wave (mm-wave) frequencies (30 GHz to 300 GHz), however, were largely unexploited for commercial wireless applications up until a decade ago (PI; KHAN, 2011). The potential available bandwidth within the mm-wave spectrum encouraged research towards enabling the development of new transmission architectures (PI; KHAN, 2011; WEI et al., 2014; MARCUS; PATTAN, 2005; MA et al., 2018; RAPPAPORT et al., 2017; WELLS, 2009).

Still, mm-waves are more significantly affected by the free-space path loss, as a direct result of the Friis transmission law, in addition to attenuation caused by atmospheric gases, dust, and rain (WEI et al., 2014; MARCUS; PATTAN, 2005). For a cellular system, this presents both a challenge to overcome and an opportunity to derive benefits. On one hand, the same frequency can be reused at short distances due to higher attenuation, and the limited transmission range enhances security and privacy (WEI et al., 2014). On the other hand, this implies the need for a greater number of antennas and base stations for the same coverage had at lower frequencies, resulting in higher power consumption, augmenting the need to design energy-efficient devices and systems.

In the pursuit of sustainable and energy-efficient mobile communication systems, one of multiple strategies is to minimize the effects of attenuation at mm-waves and offset the aforementioned benefits and drawbacks. This can be achieved by leveraging frequencies where there are valleys in the attenuation caused by atmospheric gases. As depicted in Figure 2, a valley exists in the Ka band (26 GHz to 40 GHz), starting at sub-mm-waves around 25 GHz and extending up to approximately 40 GHz. Notably, during the World Radiocommunication Conference (WRC) of 2019, the ITU adopted two resolutions introducing three new frequency bands for International Mobile Telecommunications (IMT) services: 24.25 GHz to 27.5 GHz, 37 GHz to 43.5 GHz, and 47.2 GHz to 48.2 GHz (ITU, 2019a; ITU, 2019b; ITU, 2019c). These bands are now being allocated for mobile services in many countries (ANATEL, 2022a; ANATEL, 2022b; ISED, 2022; OFCA, 2023; NTRA, 2021; FCC; NTIA, 2016).

Figure 2 – Specific attenuation as a function of frequency for dry and wet atmosphere, considering the frequency ranges of (a) 10 GHz to 300 GHz, and (b) 10 GHz to 50 GHz.

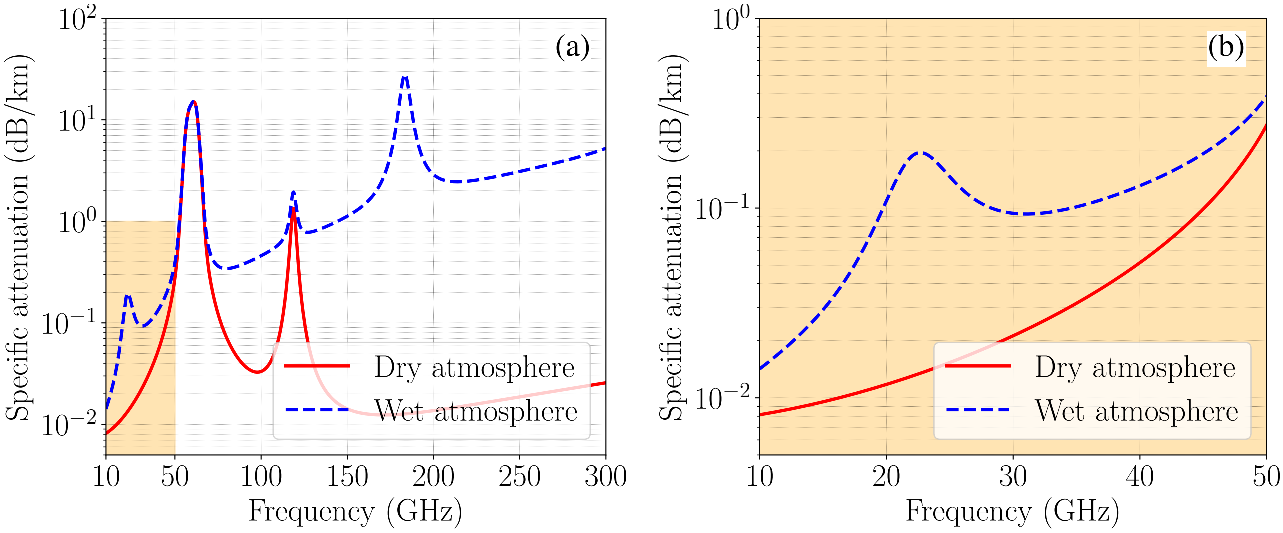

Source: Author, with data from ITU (2022), utilizing Python library provided by Portillo (2017).

Another solution that could contribute to the energy-efficiency of mm-wave systems involves the use of a dual-reflector antenna fed by a coaxial horn operating in transverse electromagnetic mode (TEM). This antenna, depicted in Figure 3, possesses an omnidirectional high-gain characteristic. This characteristic contributes to extending the coverage range of a communication cell, potentially reducing the need for numerous base stations. Additionally, its wideband behaviour, which is dictated by the coaxial horn, allows for the shared utilization of the same radio systems by multiple providers. Hence, the emphasis of this work will be on investigating the wideband behaviour of the coaxial horn, considering its operation within the Ka band.

Figure 3 – Illustration of a cross-sectional view of the dual-reflector antenna and the coaxial horn, alongside their respective radiation patterns.

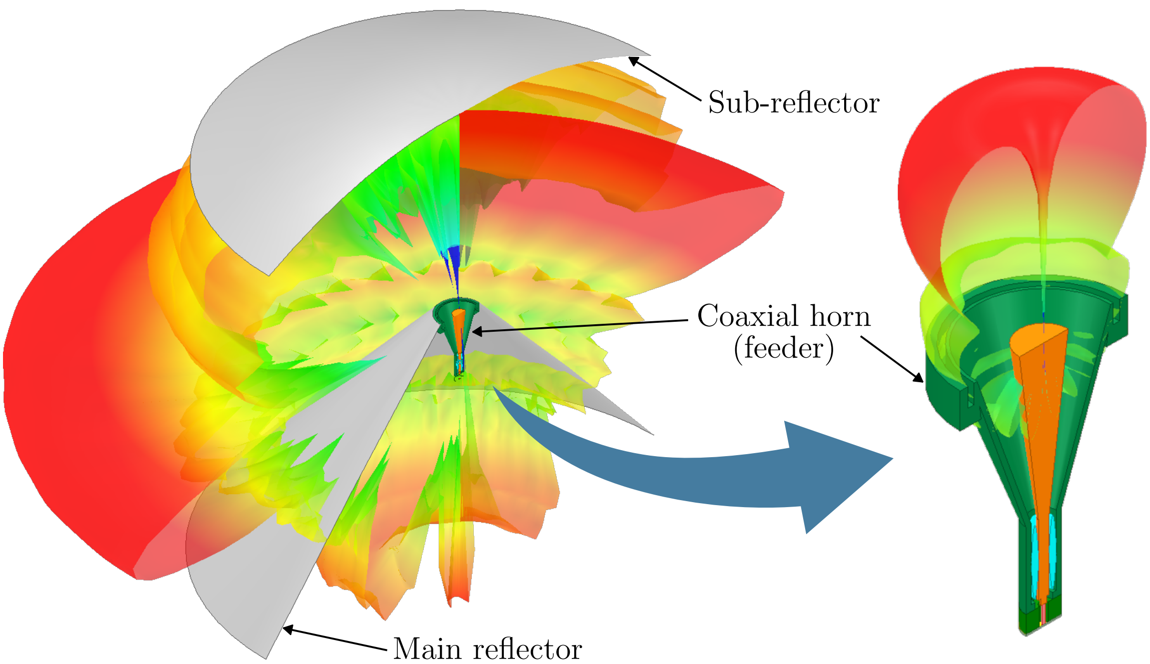

Source: Author.

1.2 STATE-OF-THE-ART OF OMNIDIRECTIONAL ANTENNAS OPERATING IN MILLIMETRE WAVES

Recent developments have demonstrated several antennas for operation within the Ka band, reporting a wideband behaviour and an omnidirectional high-gain characteristic. Examples include the biconical antenna with an annular metal lens (ZHANG; LEUNG; LU, 2023), the 3D printed quadruple-ridged conical horn (WU et al., 2020); an antenna primarily composed of radiation circular loops and a conical reflector (FAN et al., 2018); a monopole with planar annular-distributed side reflectors (PHAM; LEE; LIM, 2021), and the shared-aperture antenna (FENG et al., 2023). These antennas exhibit a relative impedance bandwidth ranging from 11% to 60% and a maximum peak gain between 6 dBi and 11.6 dBi. Commercial solutions are also available, exhibiting a typical relative bandwidth of 40% and peak gain between 3 dBi and 7.5 dBi (PASTERNACK, 2019; ERAVANT, 2018a; ERAVANT, 2018b).

As stated previously in Section 1.1, the dual-reflector antenna presents an efficient solution for operation in mm-waves. This antenna and its advantages are investigated by Bergmann and Moreira (2004), Moreira and Bergmann (2006), Zang and Bergmann (2014), Penchel et al. (2018), and Penchel et al. (2019). Typically, the entire dual-reflector antenna exhibits a relative impedance bandwidth larger than 45% and a maximum peak gain ranging between 9 dBi and 13 dBi, depending on the reflector and sub-reflector configuration. The feeder for the dual-reflector antenna, the TEM coaxial horn, which is the focus of this work, was explored more deeply by Zang and Bergmann (2014) and Penchel et al. (2019).

Penchel et al. (2019) conducted a study on the primary regions of the coaxial horn for operation in frequencies from 25 GHz to 40 GHz. This study resulted in a device with a simulated return loss greater than 20 dB throughout the entire intended frequency band and a simulated maximum peak gain of around 12 dBi. However, the presented device does not represent a functional model, as it still lacks the supporting structure for the inner conductor and an appropriate coupler to a standardized feed access. Additionally, the radiation pattern of the model exhibits large variations along the band and nulls at the sub-reflector direction, compromising the efficiency of the antenna.

Zang and Bergmann (2014) present a complete working model for the coaxial horn operating in the X band, including a transition to an N-type connector and a dielectric support structure for the inner conductor. The model achieved a relative impedance bandwidth of 30% and a peak gain of 10 dBi. Nonetheless, the implementation of the proposed dielectric structure led to a complex manufacturing process, requiring the coaxial horn to be fabricated in two separate parts that are assembled after the dielectric is inserted.

1.3 OBJECTIVES OF THIS WORK

This work centres on the role of the coaxial horn as a feeder for dual-reflector antennas operating within the Ka band (26 GHz to 40 GHz). It encompasses three primary objectives: firstly, optimizing the wideband behaviour of the coaxial horn, with the magnitude of the reflection coefficient and $|S_{11}| \leq -20$ dB impedance bandwidth serving as benchmarks; secondly, achieving a uniform radiation pattern throughout the Ka band, avoiding nulls in elevation angles lower than 55° to ensure proper illumination of the sub-reflector (MOREIRA; BERGMANN, 2006; PENCHEL; BERGMANN; MOREIRA, 2013; ZANG; BERGMANN, 2014; PENCHEL et al., 2018; PENCHEL et al., 2019); and thirdly, designing the geometry of the coaxial horn to facilitate fabrication, with a specific focus on additive manufacturing.

Ultimately, this work proposes the design of two coaxial horn models: the standard coaxial horn, serving as a practical prototype of the device presented in the literature by Penchel et al. (2019), utilizing the same dimensions but incorporating essential elements to enable its fabrication without compromising performance; and the shaped coaxial horn, an optimized version considering the aforementioned objectives.

1.4 ORGANIZATION OF THIS DOCUMENT

This document is structured into seven chapters. Chapter 1 (this chapter) introduces the motivations and context of this work, as well as its objectives, and cites publications that resulted from parts of this work. Chapter 2 provides a general overview of the numerical analysis and optimization methods employed. Chapter 3 describes and illustrates the geometries of the three main coaxial horn models assessed in this work. Chapter 4 presents the analysis of the aperture, cylindrical region, and transition region, explains applied modifications and presents optimization results leading to the final model for the standard coaxial horn. Chapter 5 presents modifications made to the conical region and the optimization process leading to the final model for the shaped coaxial horn. Chapter 6 details the fabrication of the standard coaxial horn through additive manufacturing, presents its characterization, explores discrepancies between simulated and measured results, and concludes with a performance comparison against state-of-the-art designs and commercial solutions operating within the Ka band. Lastly, Chapter 7 concludes this document.

1.5 PUBLICATIONS DERIVED FROM THIS WORK

Several publications have outlined the objectives and findings of this work, as summarized below:

2019

- SIMIONATO, E.; PENCHEL. R. A. Otimização de uma Corneta Coaxial TEM Operando na Faixa de Ondas Milimétricas. **XI Encontro Sanjoanense de Engenharia e Tecnologia (ENSET)**, 2019.
- SIMIONATO, E.; PENCHEL. R. A. Análise do Diagrama de Radiação de uma Corneta Coaxial TEM. In: **XXXI Congresso de Iniciação Científica da Unesp**, 2019. Anais do XXXI Congresso de Iniciação Científica da Unesp, 2019. ISSN 2178-860X.

2020

- SIMIONATO, E.; PENCHEL. R. A. Design e Otimização de Estruturas de Suporte e Transição para uma Corneta Coaxial TEM Operando em Ondas Milimétricas. In: **XXXII Congresso de Iniciação Científica da Unesp**, 2020. Anais do XXXII Congresso de Iniciação Científica da Unesp, 2020. ISSN: 2178-860X. DOI: 10.29327/143068.

- SIMIONATO, E. et al. Design and Optimization of a TEM Coaxial Horn for Wideband Operation in Millimeter Waves. In: **XXXVIII Simpósio Brasileiro de Telecomunicações e Processamento de Sinais**, 2020. Anais de XXXVIII Simpósio Brasileiro de Telecomunicações e Processamento de Sinais. DOI: 10.14209/SBRT.2020.1570661682.

2021

- SIMIONATO, E.; PENCHEL. R. A. Otimização do diagrama de radiação de uma corneta coaxial TEM ao longo da banda Ka. In: **XXXIII Congresso de Iniciação Científica da Unesp: Agenda 2030 e as Perspectivas da Iniciação Científica da Unesp**, 2021. Anais do XXXIII Congresso de Iniciação Científica da Unesp: Agenda 2030 e as Perspectivas da Iniciação Científica da Unesp, 2021. ISSN: 2178-860X. DOI: 10.5016/2178-86X.XXXIIICIC2021a.
- SIMIONATO, E.; PENCHEL. R. A. Design and Analysis of a TEM Coaxial Horn. **Proceeding Series of the Brazilian Society of Computational and Applied Mathematics**, v. 8, p. 100, 2021.

2022

- SIMIONATO, E. et al. Estudo do Comportamento Eletromagnético de uma Corneta Coaxial Operando em Ondas Milimétricas. In: Denilson Paulo Souza dos Santos. (Org.). **Tendências e avanços científicos nas engenharias: aeronáutica, aeroespacial, eletrônica e de telecomunicações.** 1ed. Campina Grande: Amplla, 2022, v. 1, p. 70-90. ISBN: 978-65-5381-037-2. DOI: 10.51859/amplla.tac372.1122-0.
- SIMIONATO, E.; PENCHEL. R. A. Electromagnetic Analysis of a Complete Omnidirectional Dual-Reflector Antenna fed by a Coaxial Horn. **Proceeding Series of the Brazilian Society of Computational and Applied Mathematics**, v. 9, p. 67, 2022.
- SIMIONATO, E. et al. Novel coaxial transition for shaped coaxial horn antennas operating at millimeter wave frequencies. In: **2022 IEEE International Symposium on Antennas and Propagation and USNCURSI Radio Science Meeting (APS/USNCURSI)**, 2022, Denver. p. 551. DOI: 10.1109/AP-S/USNC-URSI47032.2022.9886866.

2023

- SIMIONATO, E. et al. Antena Banda Larga Operando em Ondas Milimétricas Fabricada Via Manufatura Aditiva de Matais e Polímeros. In: **XXXV Congresso de Iniciação Científica da Unesp**, 2023.
- SIMIONATO, E. et al. Ka-Band Coaxial Horn Antenna Fabricated via Plastic and Metal Laser Powder Bed Fusion. **IEEE Transactions on Antennas and Propagation**. Unpublished. Submitted nov. 2023, under review.

2 NUMERICAL ANALYSIS AND OPTIMIZATION METHODS

This work will rely on the commercial simulation software Ansys Electronics Desktop to analyse and optimize the electromagnetic behaviour of the coaxial horn. Ansys Electronics Desktop offers a comprehensive environment for designing and simulating various electronic components and devices in a unified user interface, covering electromagnetic designs, thermal designs, and circuits (ANSYS, 2023a). In particular, the High Frequency Structure Simulator (HFSS) module will be utilized — a multipurpose, full-wave 3D electromagnetic simulation software designed for the creation and simulation of high-frequency electronic products. This chapter provides a description of the general workflow, setup, and definitions used in HFSS.

The design process (Figure 4) commences by selecting a solution type, which in this case was a Terminal Network Analysis. Subsequently, the geometry of the coaxial horn is constructed in HFSS integrated CAD environment, with generic values assigned to all relevant dimensions (see Chapter 3) to create a parameterized model. Material characteristics, boundaries, and sources of electromagnetic fields (excitations) are then assigned to the model. In this work, a perfect electric conductor (PEC) is used for the conducting parts of the coaxial horn, and Teflon ($\epsilon_r = 2.1$) is employed to model the dielectric structure (detailed in Section 4.2). The coaxial horn model is enclosed by an autogenerated radiation boundary, and a wave port excitation is applied. The solution setup involves solving for broadband, spanning from 25 GHz to 40 GHz. Two frequency sweeps are specified: one of interpolating type, with a linear step distribution from 25 GHz to 40 GHz, employing a step of 0.001 GHz, primarily used to verify the reflection coefficient; and one of discrete type, with a linear step distribution from 26 GHz to 40 GHz, with a step of 2 GHz, utilized to verify the radiation pattern throughout the Ka band. HFSS, employing Finite Element Method (FEM), generates the tetrahedral mesh, solves Maxwell's equations for each tetrahedron, generates the necessary field solutions, associated port characteristics, and S-parameters, and repeats for every frequency of interest (ANSYS, 2023b; SADIKU, 1989).

Figure 4 – General workflow in HFSS.

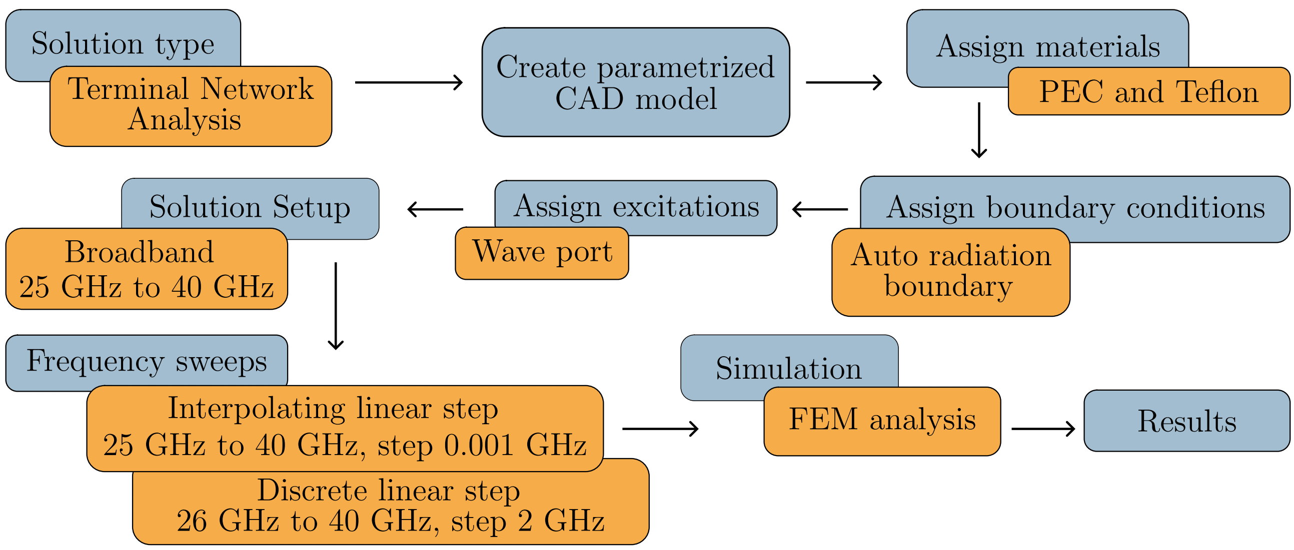

Source: Author.

To delve into the electromagnetic behaviour of the coaxial horn, two techniques available in HFSS Optimetrics section were utilized. The first technique was parametric analysis, where one or more variable sweeps are defined, specifying a series of variable values within a given range (ANSYS, 2023b). The second technique was heuristic optimization, employed to use resources more efficiently due to the elevated number of optimization variables and the time-consuming FEM analysis. The optimizer used was the Genetic Algorithm (GA), built into HFSS Optimetrics, which allows the specification of the cost function and optimization goals based on any solution quantity that can be computed (ANSYS, 2023b). In summary, the GA is a widely used iterative method that emulates the natural evolution of species. It considers a population of provisional solutions to a given problem, refined at each generation by selecting the best individuals — those presenting the best value of the figure of merit. The iterative process continues until the goal is attained or the maximum number of iterations is reached. In this project, GA optimization was used merely as a tool to identify a narrow range of values from which a satisfactory solution could be obtained; therefore, HFSS default configuration was used (refer to Figure 5). This document will provide details for both parametric analysis and GA optimization whenever they were applicable to the development of the project.

Figure 5 – Default options for HFSS genetic algorithm optimizer.

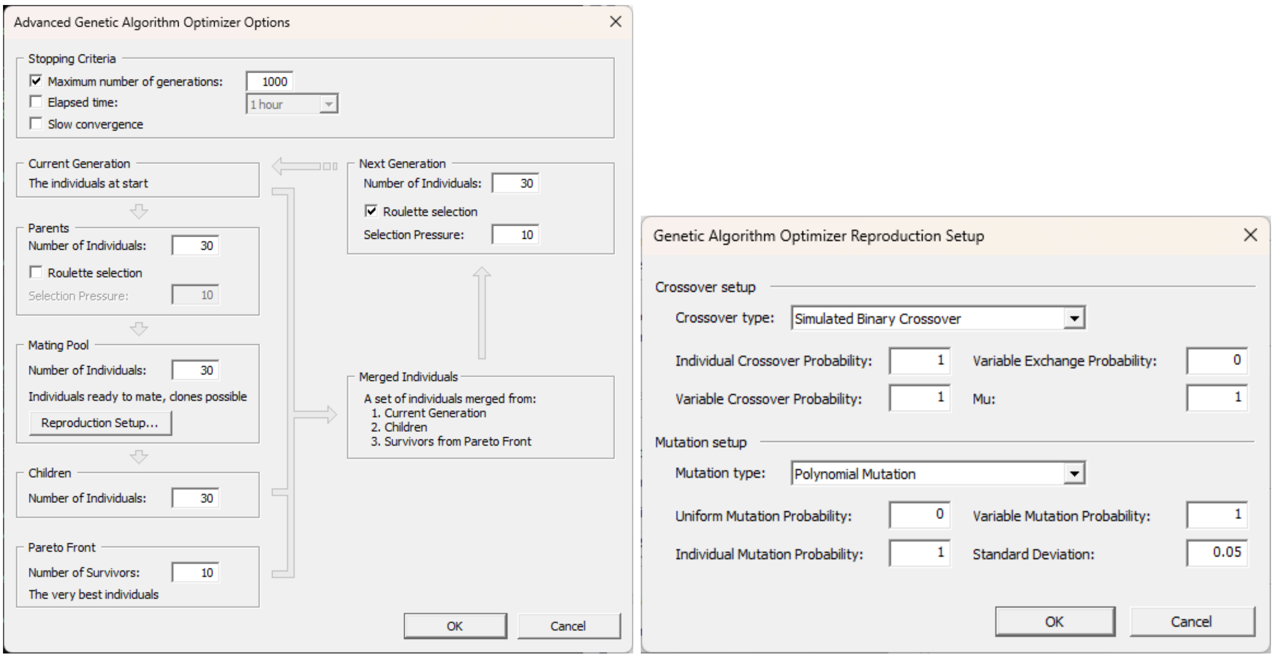

Source: Author.

Seeking to reduce the time required for simulating each iteration in GA, symmetry boundaries were defined to leverage the axisymmetric geometry of the coaxial horn. This involved using the Modal solution type instead of the Terminal solution type used for the rest of the analyses. The Modal solution type allows the simulation to consider only a fraction of the geometry specified in the CAD environment, reducing the necessary number of elements to form the finite element mesh and, consequently, reducing the simulation time. Initially, simulations with symmetry boundaries were conducted considering half and one-quarter of the geometry of the coaxial horn. The resulting magnitude of the reflection coefficients ($|S_{11}|$) were then compared to those obtained with the Terminal solution to verify their accuracy (refer to Figure 6). The comparison also included the simulation of the full geometry using Modal solution to validate the excitation setup, and the resulting $|S_{11}|$ is shown in Figure 6. The symmetry condition used was a Perfect Magnetic Conductor (PMC), as the electric field is tangent to the defined symmetry planes, as shown in Figure 7 (ANSYS, 2023b).

Figure 6 – Deviation of the reflection coefficient magnitude for each Modal solution from the reference Terminal solution.

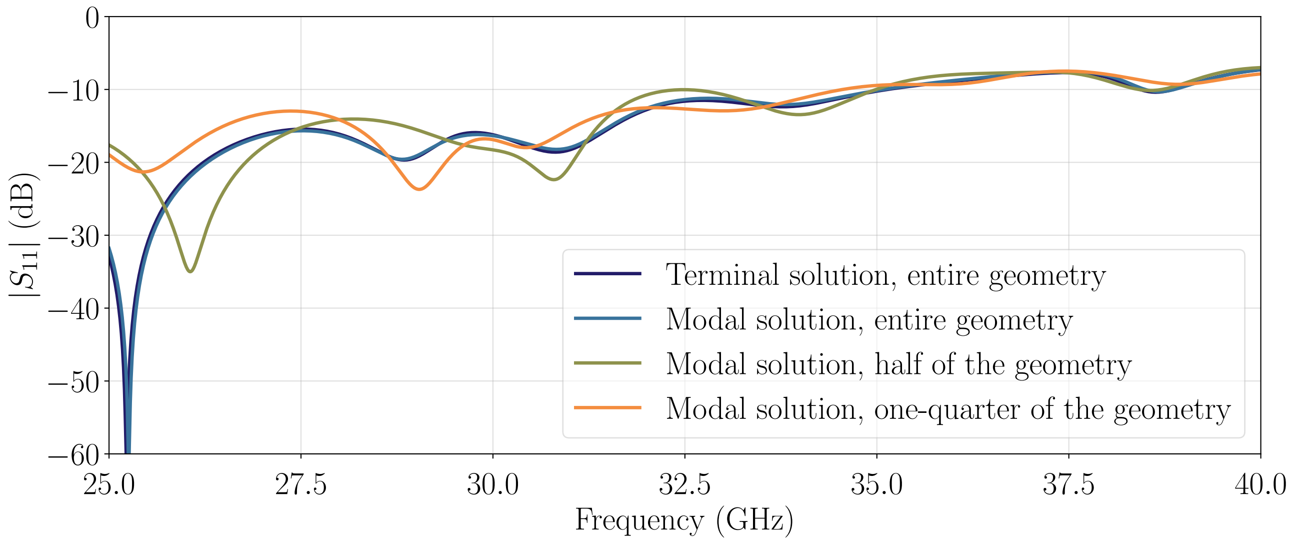

Source: Author.

Figure 7 – Symmetry planes for (a) half of the geometry, and (b) one-quarter of the geometry.

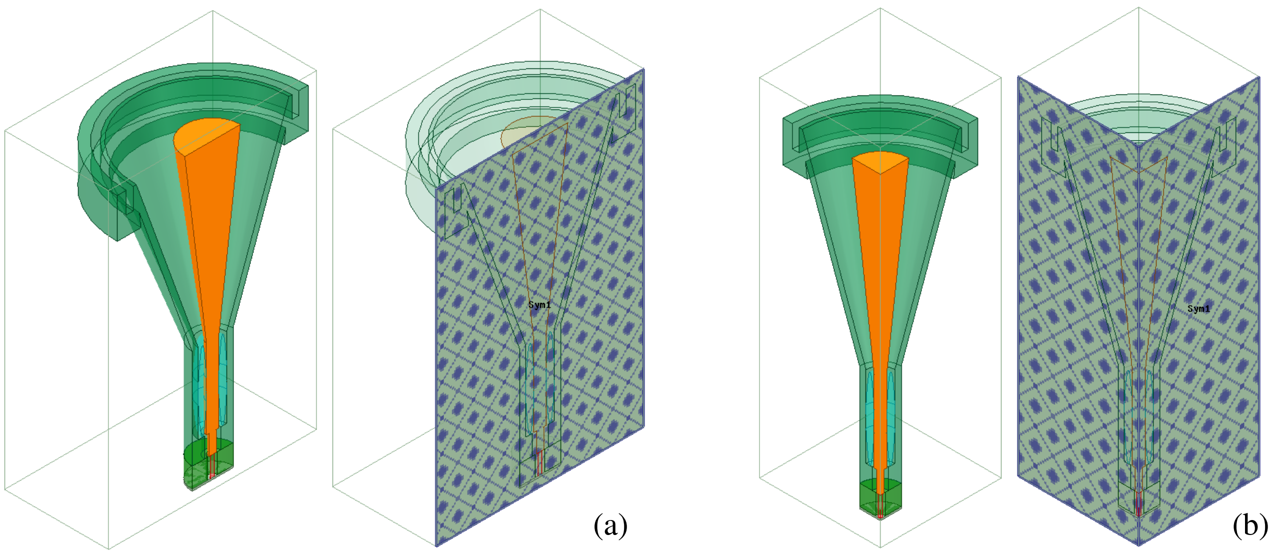

Source: Author.

As observed in Figure 6 the magnitude of the reflection coefficient for the entire geometry, using both Terminal and Modal solutions, remained practically unchanged. The simulation with half of the geometry produced results close to those with the entire geometry, with more significant differences in frequencies below 30 GHz. The result for one-quarter of the geometry is the most distant from the result for the entire geometry across the frequency band. Given the comparable simulation times reported in Table 1 for both half and one-quarter of the geometry, and considering that the result for half the geometry was the closest to the entire structure, the half geometry was employed in GA optimization.

Table 1 – Simulation times for different solution types and fractions of the geometry.

Terminal Solution	**Modal Solution**		
Entire geometry	Entire geometry	Half of the geometry	One-quarter of the geometry
10 min. 20 sec.	9 min. 04 sec.	1 min. 12 sec.	1 min. 05 sec.

Source: Author.

Throughout the development of this work, two key antenna parameters for the coaxial horn were examined: the magnitude of the reflection coefficient ($|S_{11}|$) and the radiation pattern. The magnitude of the reflection coefficient, expressed in decibels (dB), will now be simply referred to as the "reflection coefficient", aligning with the most widely used terminology in the literature. The radiation pattern was assessed for an elevation plane through the gain, measured in decibels relative to an isotropic radiator (dBi); and depicted using the conventional spherical coordinate system (r, θ, ϕ), with elevation angles represented by theta (θ), and azimuth angles represented by phi (ϕ). The gain is proportional to the ratio of the radiation intensity of the antenna in a given direction to the total power accepted by the antenna (ANSYS, 2023b). Therefore, the gain takes into account the radiation efficiency but does not consider losses due to impedance mismatches. The analysed radiation patterns corresponds to one of the E-planes of the coaxial horn (xz in Figure 8), while in the H-plane (xy in Figure 8) the coaxial horn exhibits an omnidirectional radiation pattern. All E-planes of the coaxial horn can be more effectively described in a cylindrical coordinate system, where the E-planes correspond to the ρz plane.

Figure 8 – Illustration of the coaxial horn alongside its azimuthal and elevation radiation patterns.

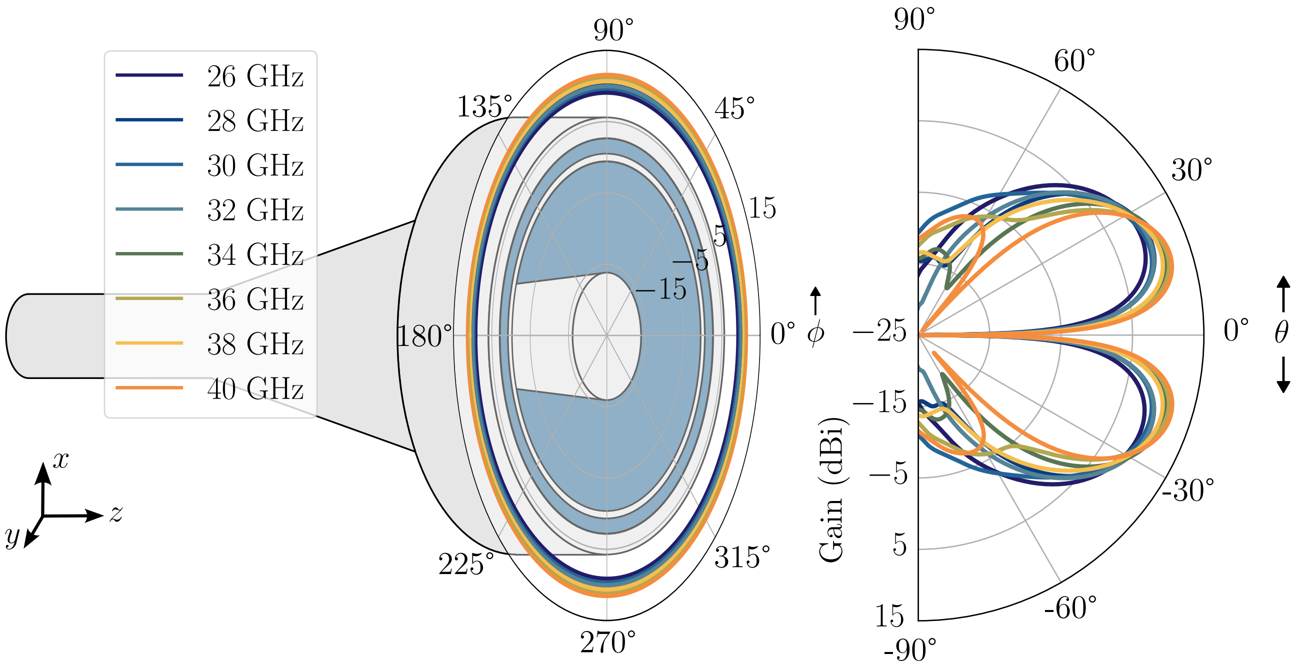

Source: Author.

3 GEOMETRY OF THE COAXIAL HORN

This chapter provides a general overview of the initial geometry of the coaxial horn, along with the two proposed models: the standard and shaped coaxial horn. Table 2 shows a concise overview of each dimension considered relevant, many of which are shared by the three models of the coaxial horn, as will be discussed and illustrated later.

Table 2 – Description of the parameters of the coaxial horn.

Parameter	Description
$r_{a,i}$	Inner radius of the aperture
$r_{a,o}$	Outer radius of the aperture
d_s	Depth of the choke-ring slot
w_s	Width of the choke-ring slot
w_i	Width of the innermost section of the choke-ring (closest to the aperture)
w_o	Width of the outermost section of the choke-ring (farthest from the aperture)
d	Total depth of the choke-ring
l	Length of the conical region
$r_{c,i}$	Inner radius of the cylindrical region
$r_{c,o}$	Outer radius of the cylindrical region
l_c	Length of the cylindrical region
l_s	Total length of the dielectric support
l_{sc}	Length of the cylindrical section of the dielectric support
$r_{t,i}$	Inner radius of the transition region
$r_{t,o}$	Outer radius of the transition region
l_t	Length of the transition region
$r_n, n = 1, 2, 3$	Control points of the spline shaping the inner conductor
$d_n, n = 1, 2, 3$	Control points of the spline shaping the outer conductor

Source: Author.

The initial coaxial horn is described in the literature by Penchel et al. (2019), and showcases outstanding performance ($|S_{11}| < -20$ dB). However, it lacks the necessary structures to function as a prototype. As illustrated in Figure 9, the coaxial horn from the literature consists only of the inner and outer conductors. Relevant dimensions, presented in Table 3 and illustrated in Figure 10, are provided in millimetres and as a function of the free-space wavelength (λ). The frequency associated with λ throughout this document is 28 GHz ($\lambda = 10.714$ mm), in alignment with the reference frequency employed by Penchel et al. (2019). Additionally, Figure 10 highlights the division of the coaxial horn into two key regions: the cylindrical region, functioning as a coaxial waveguide with a 50 Ω impedance, and the conical region that terminates at the aperture, where a choke-ring, or corrugation, is placed.

Figure 9 – Three-dimensional exploded view drawing of the coaxial horn from the literature.

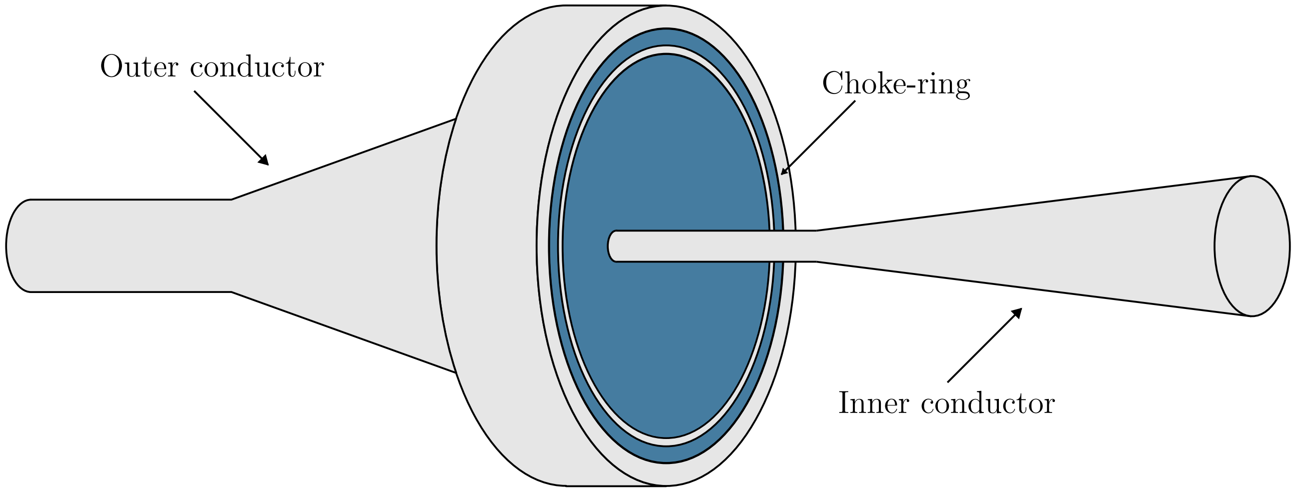

Source: Author.

Table 3 – Dimensions of the literature coaxial horn.

Parameter	Value (λ)	Value (mm)
$r_{a,i}$	0.350	3.750
$r_{a,o}$	0.960	10.280
d_s	0.270	2.893
w_s	0.085	0.911
w_i	0.040	0.428
w_o	0.115	1.232

Parameter	Value (λ)	Value (mm)
d	0.500	5.357
l	2.170	23.250
$r_{c,i}$	0.077	0.825
$r_{c,o}$	0.178	1.907
l_c	1.000	10.714

Source: Author

Figure 10 – Dimensions and regions of the coaxial horn from the literature.

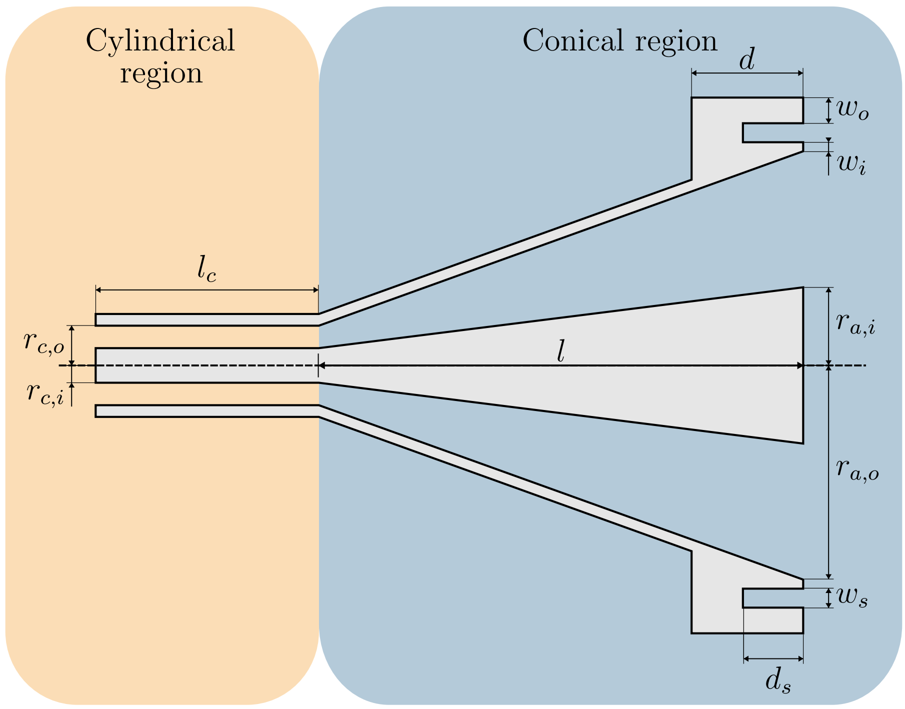

Source: Author.

The standard coaxial horn, depicted in Figure 11, introduces a transition region and a dielectric support to the literature coaxial horn. It aims to serve as a functional prototype while maintaining the dimensions of the cylindrical and conical regions as presented by Penchel et al. (2019). The added structures are optimized to avoid any negative impact on performance, ensuring $|S_{11}| < -20$ dB. The initial dimensions for the added structures are detailed in Table 4, along with the dimensions of the cylindrical and conical regions which will remain the same as the ones reported by Penchel et al. (2019), organized in Table 3. The complete set of dimensions for the standard coaxial horn is illustrated in Figure 12. Further insights into the dielectric support geometry and the rationale behind the initial dimensions will be provided in Chapter 4.

Figure 11 – Three-dimensional exploded view drawing of the standard coaxial horn.

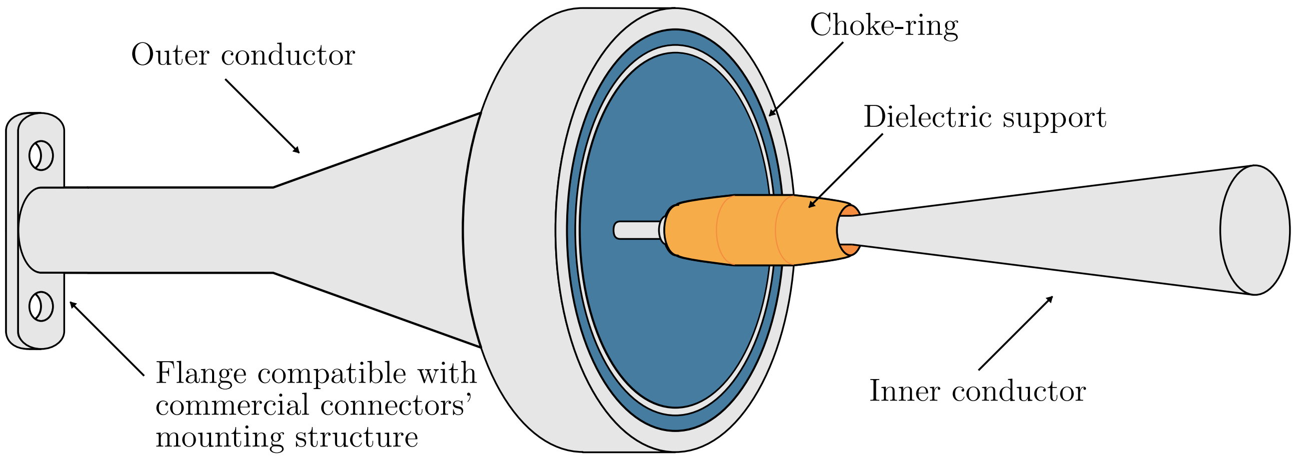

Source: Author.

Table 4 – Initial dimensions of the standard coaxial horn.

Parameter	Value (λ)	Value (mm)	Parameter	Value (λ)	Value (mm)
$r_{a,i}$	0.350	3.750	$r_{c,i}$	0.077	0.825
$r_{a,o}$	0.960	10.280	$r_{c,o}$	0.178	1.907
d_s	0.270	2.893	l_c	1.000	10.714
w_s	0.085	0.911	l_s	1.000	10.714
w_i	0.040	0.428	l_{sc}	0.250	2.678
w_o	0.115	1.232	$r_{t,i}$	0.068	0.728
d	0.500	5.357	$r_{t,o}$	0.156	1.671
l	2.170	23.250	l_t	0.250	2.678

Source: Author.

Figure 12 – Dimensions and regions of the standard coaxial horn.

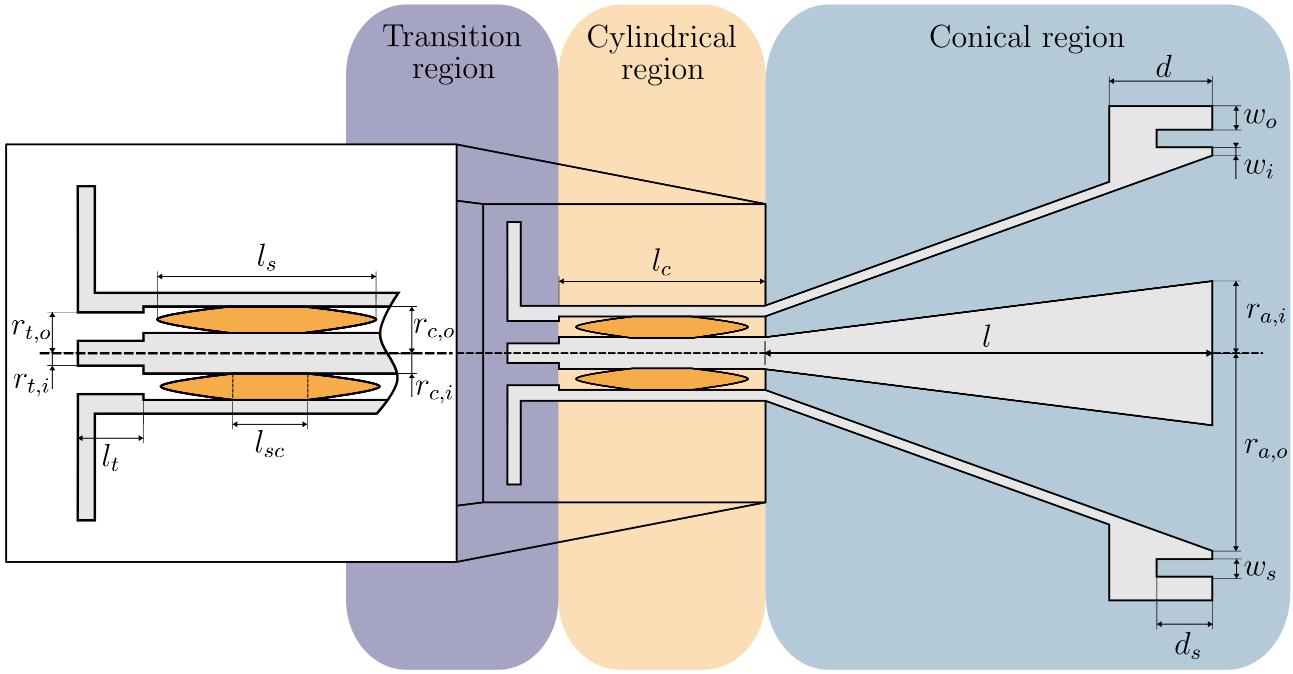

Source: Author.

Lastly, the shaped coaxial horn is presented in Figure 13. It also consists of a dielectric support, and inner and outer conductors, which can be divided into three regions of interest: transition, cylindrical, and conical, as depicted in Figure 14. A distinctive feature of the shaped coaxial horn is the use of a spline with three control points to model the conical region for both inner and outer conductors. This approach aims to enhance the performance and radiation characteristics of the standard coaxial horn. Table 5 provides the initial dimensions for the shaped coaxial horn. For a deeper understanding of the shaped conical region, refer to Chapter 5.

Figure 13 – Three-dimensional exploded view drawing of the shaped coaxial horn.

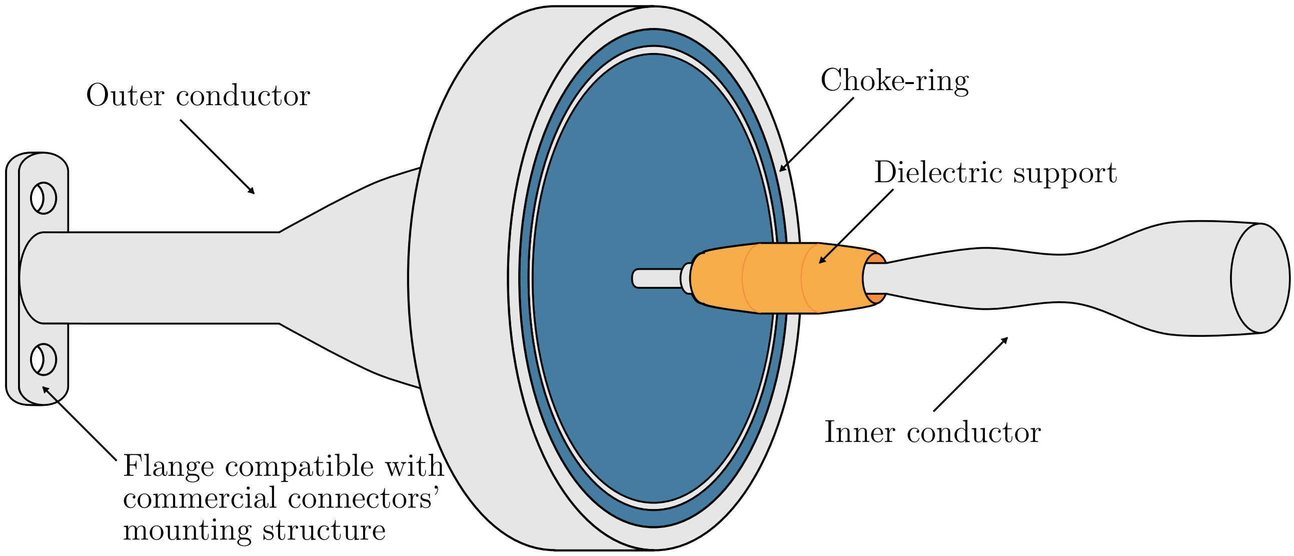

Source: Author.

Figure 14 – Dimensions and regions of the shaped coaxial.

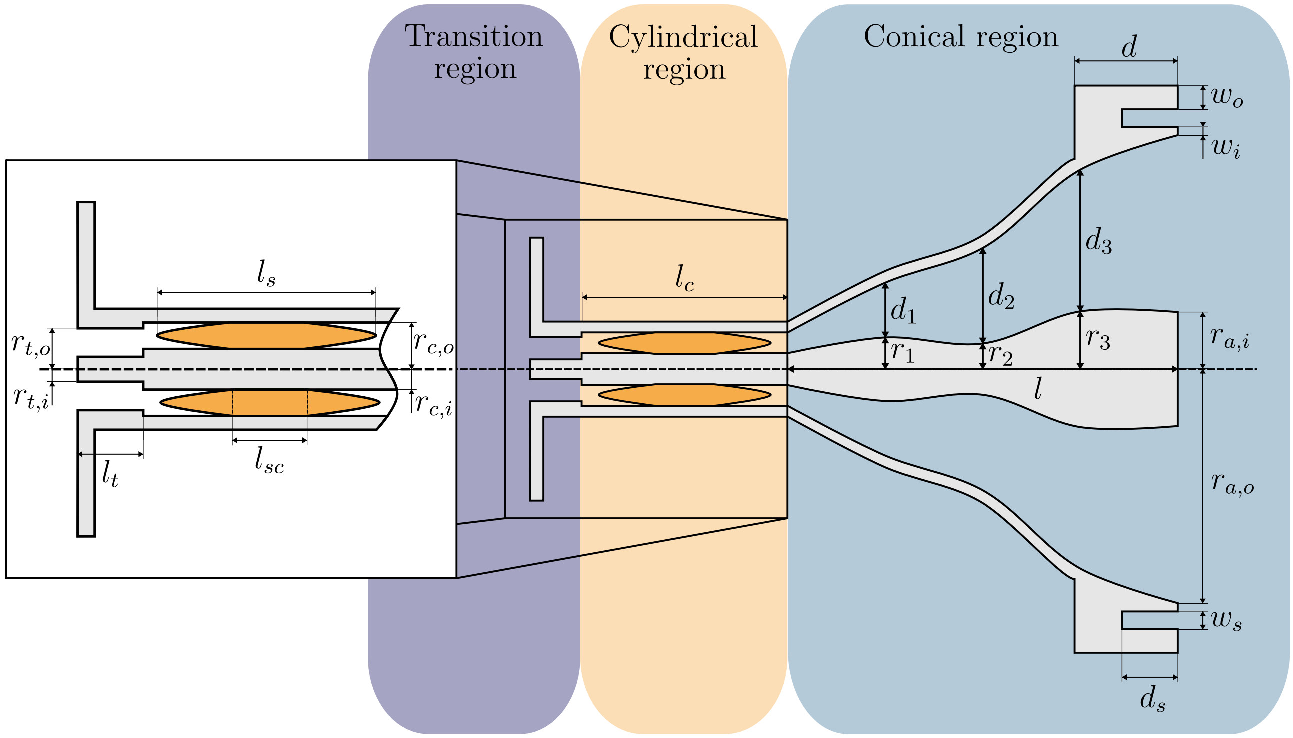

Source: Author.

Table 5 – Initial dimensions of the shaped coaxial horn.

Parameter	Value (λ)	Value (mm)	Parameter	Value (λ)	Value (mm)
$r_{a,i}$	0.290	3.107	l_s	0.924	9.900
$r_{a,o}$	0.960	10.280	l_{sc}	0.187	2.000
d_s	0.270	2.893	$r_{t,i}$	0.040	0.430
w_s	0.085	0.911	$r_{t,o}$	0.126	1.353
w_i	0.040	0.428	l_t	0.085	0.915
w_o	0.115	1.232	r_1	0.146	1.560
d	0.500	5.357	r_2	0.214	2.290
l	2.170	23.250	r_3	0.282	3.020
$r_{c,i}$	0.077	0.825	d_1	0.228	2.441
$r_{c,o}$	0.178	1.907	d_2	0.355	3.804
l_c	1.000	10.714	d_3	0.485	5.197

Source: Author.

4 STANDARD COAXIAL HORN

The study of the standard coaxial horn (see Figure 11) serves two purposes: first, to analyse the impact of different device dimensions on the reflection coefficient and radiation pattern, with the intention of applying this knowledge in a new proposed concept for a shaped coaxial horn (see Chapter 5); and second, to develop a practical prototype of the coaxial horn presented in the literature (PENCHEL et al., 2019), optimizing any implemented modifications to avoid negative effects on the performance of the device. This study starts with the literature coaxial horn (PENCHEL et al., 2019) as a control model, followed by extensive parametric analyses of the aperture and choke-ring, detailed in Section 4.1. For the literature model to become a feasible prototype, a transition region and support for the inner conductor needed to be implemented. Section 4.2 explains the dielectric support structure concept, implemented in the cylindrical region, while Section 4.3 covers the initial transition region and the parametric analysis of its dimensions. Lastly, to establish a prototype for the standard coaxial horn, heuristic optimization was employed to enhance the performance of the device. This optimization is also described in Section 4.3, and focused exclusively on the added transition region and dielectric support, maintaining the dimensions of the aperture.

4.1 APERTURE

The study of the aperture of the standard coaxial horn is conducted to understand the behaviour of the device and later be used in the optimization of the shaped coaxial horn (see Chapter 5). It encompasses the radii of the inner and outer conductors that form the aperture, along with the dimensions of the choke-ring placed at the aperture. To examine the radii that form the aperture, a parametric analysis was employed in two phases: the first explored values where the outer radius of the aperture was less than 1λ, and the second considered values where the outer radius of the aperture exceeded 1λ.

The first parametric analysis considered variations of the outer radius of the aperture ($r_{a,o}$) within the range of 0.80λ to 0.98λ, with a step size of 0.04λ. Simultaneously, the inner radius of the aperture ($r_{a,i}$) varied between 0.25λ and 0.45λ, employing a step size of 0.02λ. This section will present a subset of the produced results to support the subsequent analysis, while comprehensive results can be found in Appendix A.

Upon observing the reflection coefficients resulting from the first analysis, as organized in Figure 15, it becomes apparent that increasing the outer radius generally improves performance. Smaller (0.27λ) and larger (0.43λ, 0.45λ) values of the inner radius favour better performance at higher frequencies, above 32.5 GHz, while intermediary values (0.31λ, 0.35λ, 0.39λ) present better performance at lower frequencies, below 32.5 GHz.

Radiation patterns were verified for each variation in the outer radius of the aperture, considering the lowest, middle, and highest values for the inner radius. Figure 16 displays the radiation patterns for the three values of $r_{a,i}$, considering $r_{a,o} = 0.88\lambda$, for 26 GHz, 34 GHz, and 40 GHz. A tendency for a more directive beam is observed across the analysed frequencies. For example, at 26 GHz

Figure 15 – Reflection coefficients for analysed variations in the inner radius of the aperture ($r_{a,i}$), considering an outer radius ($r_{a,o}$) of (a) 0.88λ, (b) 0.92λ, (c) 0.96λ, and (d) 0.98λ.

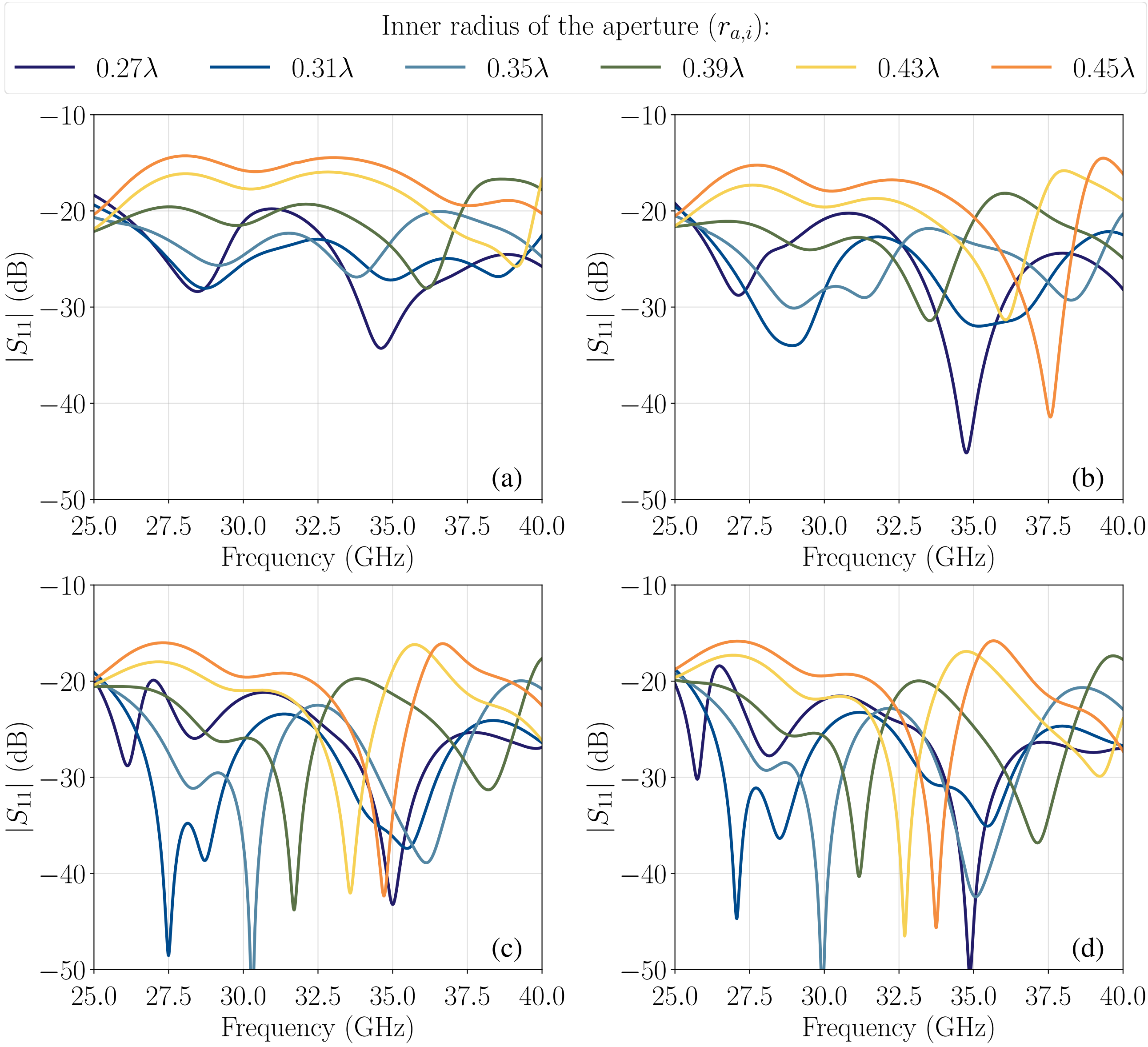

Source: Author.

(Figure 16(a)), a 3 dBi gain is achieved for an elevation angle of 55°, while the same happens for elevation angles up to 45°, at 34 GHz (Figure 16(b)), and angles up to 40°, at 40 GHz (Figure 16(c)). Directivity increases with frequency because, for higher frequencies, the electrical size of the aperture is larger, resulting in a narrower beam (BALANIS, 2016). It would be expected that with a wider physical aperture, which is achieved for smaller values of $r_{a,i}$, a narrower beamwidth is observed in each of the radiation patterns presented in Figure 16. However, the opposite occurs, with higher directivity being associated with a greater value of $r_{a,i}$ and, consequently, a narrower aperture. One possible explanation to this effect is the presence of a higher-order mode at the aperture, as elaborated in more detail by Zang et al. (2018), and by Penchel et al. (2019). These observations remain consistent when considering other values of $r_{a,o}$, as shown in Figure 17, or as observed in the comprehensive results found in Appendix A.

The second parametric analysis initially explored variations of the outer radius of the aperture ($r_{a,o}$)

Figure 16 – Radiation patterns for analysed variations in the inner radius of the aperture ($r_{a,i}$), considering an outer radius ($r_{a,o}$) of 0.88λ, at (a) 26 GHz, (b) 34 GHz, and (c) 40 GHz.

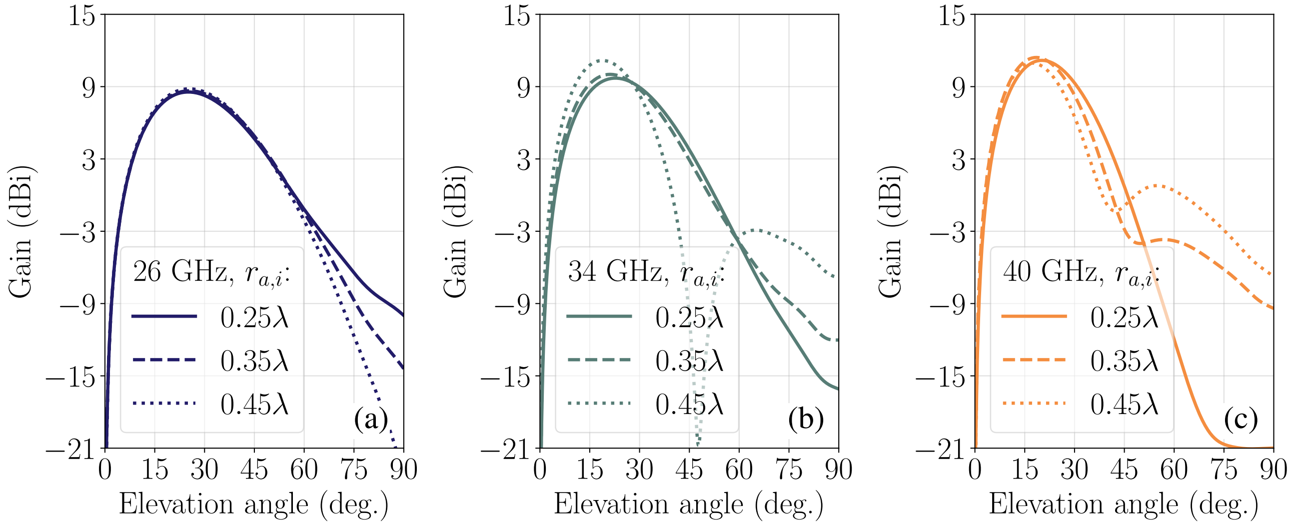

Source: Author.

Figure 17 – Radiation patterns for analysed variations in the inner radius of the aperture ($r_{a,i}$), considering an outer radius ($r_{a,o}$) of 0.96λ, at (a) 26 GHz, (b) 34 GHz, and (c) 40 GHz.

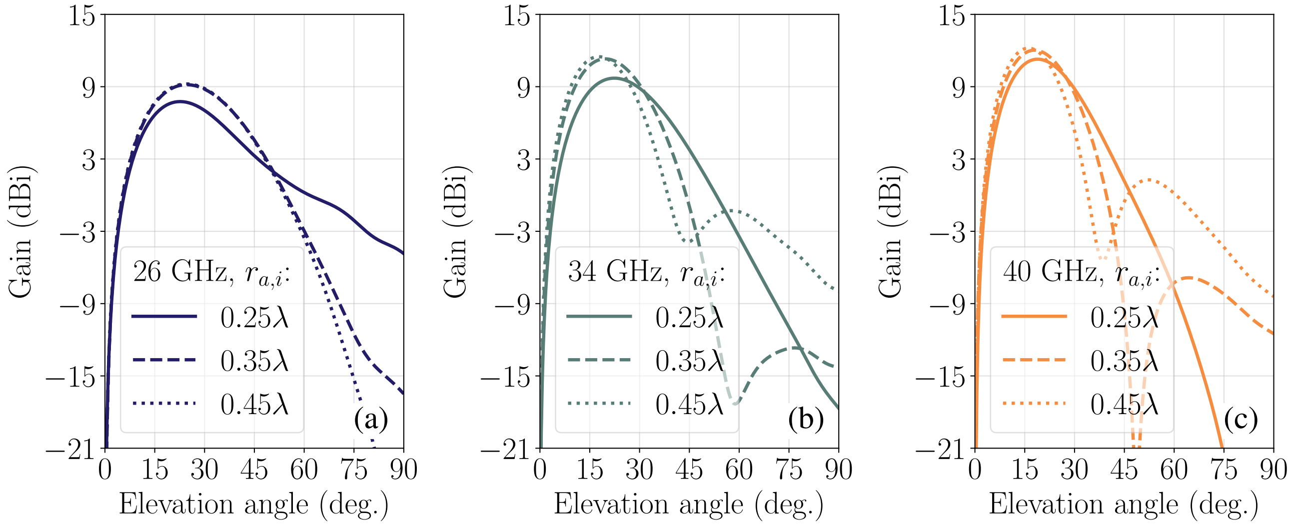

Source: Author.

within the range of 1.10λ to 2.00λ, using a step size of 0.15λ. This section will present a subset of the produced results to support the subsequent analysis, while detailed results can be found in Appendix B. Once again, as shown in Figure 18, a noticeable increase in directivity occurs for higher values of $r_{a,o}$ and a wider aperture. This heightened directivity appears to contribute to a more uniform radiation pattern. However, it is worth noting that the radiation pattern seems to degrade in the direction of higher intensity for values of the outer radius higher than 1.55λ. Examining the reflection coefficient presented in Figure 19, one notices the opposite behaviour of what was observed for the first parametric analysis: a worse performance is obtained as the outer radius of the aperture increases.

For the analysis of variations in the inner radius of the aperture, only $r_{a,o} = 1.10\lambda$, $r_{a,o} = 1.25\lambda$, $r_{a,o} = 1.40\lambda$, and $r_{a,o} = 1.55\lambda$ were considered, as values for the outer radius higher than these led to a noticeably degraded radiation pattern. The inner radius of the aperture ($r_{a,i}$) varied between 0.10λ and

Figure 18 – Radiation patterns considering an outer radius of the aperture ($r_{a,o}$) of (a) 1.10λ, (b) 1.55λ, and (c) 2.00λ.

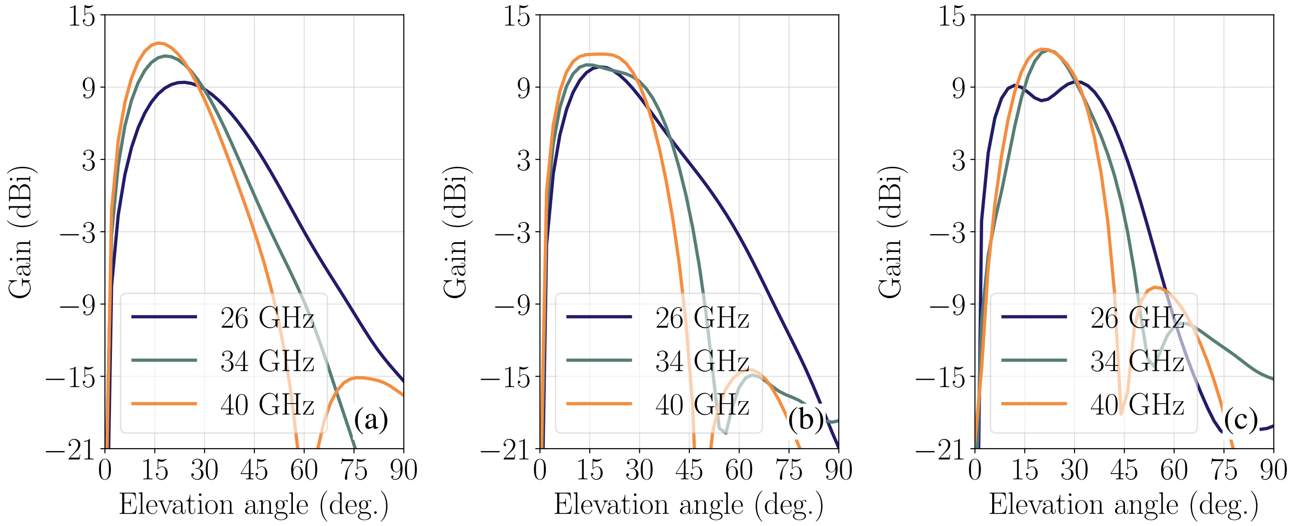

Source: Author.

Figure 19 – Reflection coefficients for analysed variations in the outer radius of the aperture ($r_{a,o}$).

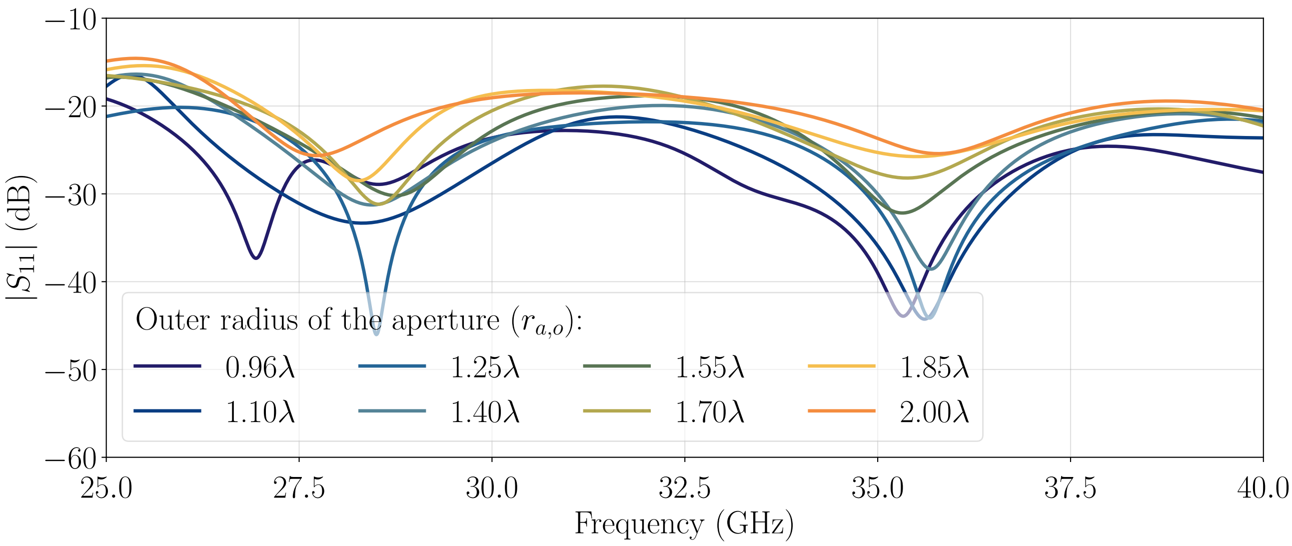

Source: Author.

0.50λ, employing a step size of 0.10λ. Reflection coefficients for this analysis are shown in Figure 20, where it is evident that the results producing the desired behaviour ($|S_{11}| < -20$ dB) were obtained for $r_{a,i} = 0.30\lambda$, a value close to the original (see Table 3). Variations greater than 0.10λ made to the inner radius of the aperture resulted in worse performance, considering $r_{a,o} > 1\lambda$. A clear relationship between the inner radius and the radiation pattern behaviour is not evident from the observations of the comprehensive results presented in Appendix B. Nonetheless, it is noteworthy that a more uniform radiation pattern without degraded behaviour also occurred consistently for $r_{a,i} = 0.30\lambda$, regardless of the value of $r_{a,o}$ considered.

After analysing the radii of the aperture, a parametric analysis of the dimensions of the choke-ring was conducted. This analysis encompassed variations in the depth of the choke-ring slot (d_s), as well as the width of the inner and outermost sections of the choke-ring (w_i and w_o, see Figure 10). The depth of the choke-ring slot and the width of its outermost section were explored within an interval

Figure 20 – Reflection coefficients for analysed variations in the inner radius of the aperture ($r_{a,i}$), considering an outer radius ($r_{a,o}$) of (a) 1.10λ, (b) 1.25λ, (c) 1.40λ, and (d) 1.55λ.

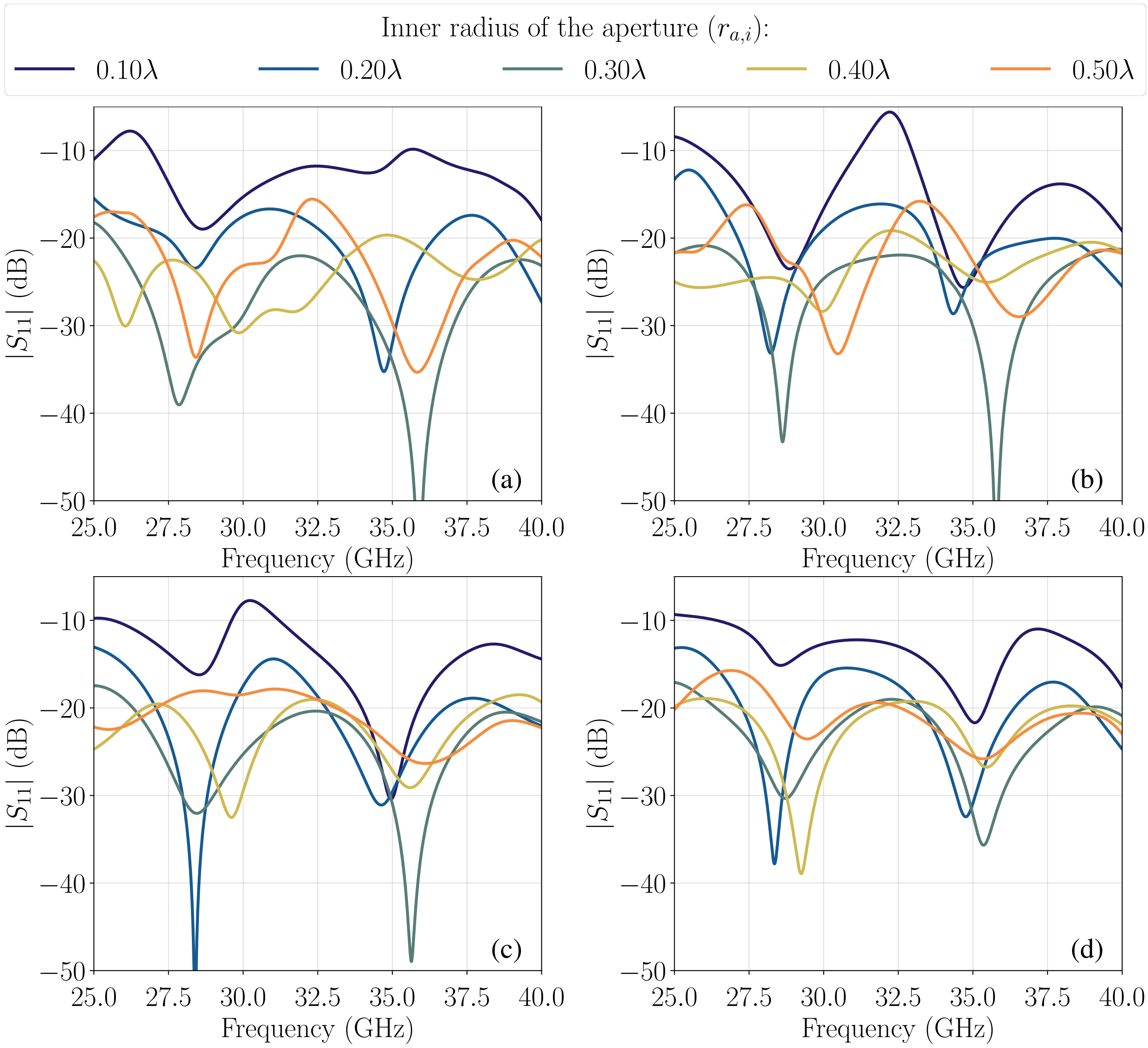

Source: Author.

corresponding to ±50% of their original values (refer to Table 3). As the width of the innermost section of the choke ring originally had a small value, the variation considered one value that was half the original and seven times the original value as an upper limit for the analysis range.

The resulting reflection coefficients are presented in Figure 21, Figure 22, and Figure 23. Notably, more substantial, albeit minor, changes occur with variations in the depth of the choke-ring slot. As seen in Figure 21, values for the depth of the slot lower than the original (1.45 mm, 1.81 mm, and 2.17 mm) generally result in poorer performance in frequencies up to around 35 GHz, with a reflection coefficient slightly above -20 dB for frequencies up to 32.5 GHz. On the other hand, values for the depth of the slot greater than the original did not cause noticeable changes. Varying the width of the innermost section (w_i) resulted in minor changes, particularly at lower frequencies for $w_i = 0.2$ mm, $w_i = 0.434$ mm, and $w_i = 0.6$ mm (see Figure 22). The reflection coefficient remained practically unaltered for variations in the width of the outermost section (w_o), as evidenced in Figure 23.

Figure 21 – Reflection coefficients for analysed variations in the depth of the choke-ring slot (d_s).

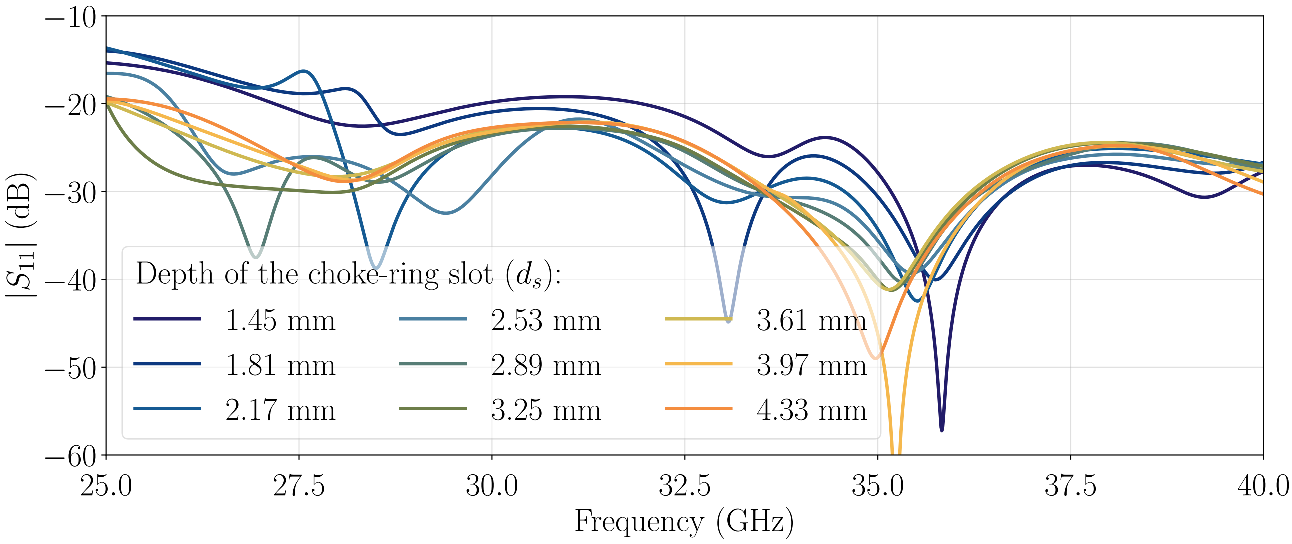

Source: Author.

Figure 22 – Reflection coefficients for analysed variations in the width of the innermost section of the choke-ring (w_i).

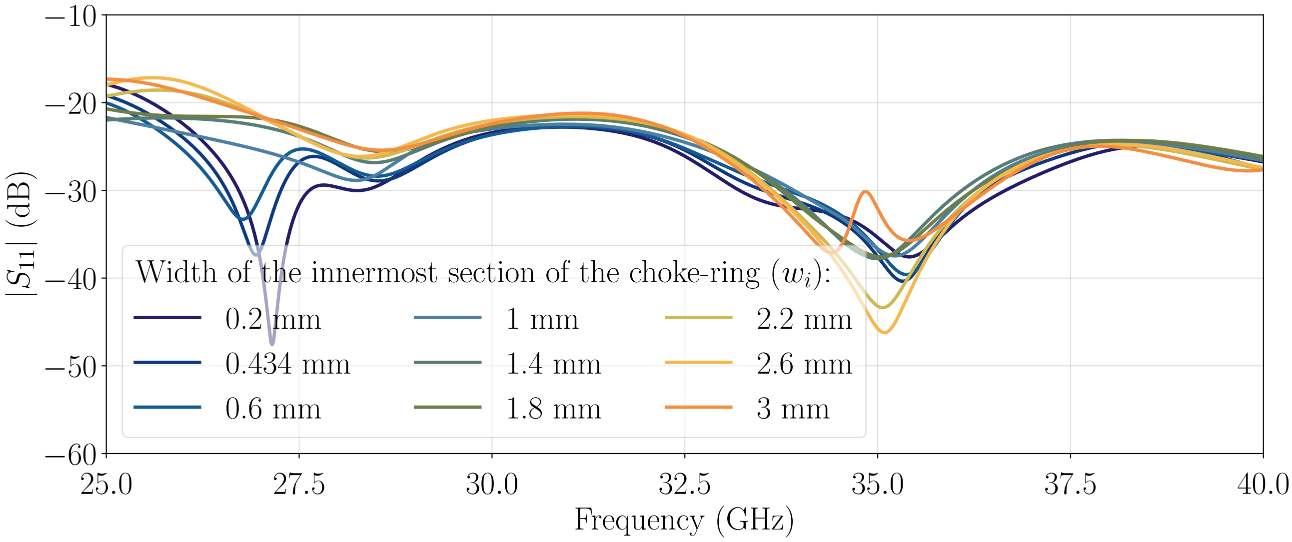

Source: Author.

Examining the radiation patterns presented in Appendix C for variations in the depth of the slot (d_s), in the width of the innermost section (w_i), and in the width of the outermost section (w_o), a similar behaviour to the analysis of the reflection coefficient is observed. More significant, yet small, modifications occur for variations in d_s, while variations in w_i and w_o do not lead to observable changes.

To further investigate the impact of the choke-ring in the coaxial horn, a simulation was conducted with a coaxial horn completely without the choke-ring. The resulting radiation pattern and reflection coefficient are compared to the version with choke-ring in Figure 24 and Figure 25. It can be concluded that the choke-ring has no significant effect on the reflection coefficient, nor in the region of interest of the radiation pattern for this study (elevation angles below 90°). However, Figure 24 shows that the choke-ring aids in reducing secondary lobes level by approximately 3 dB for elevations greater than 90°, as also observed by Bergmann and Moreira (2004), Zang and Bergmann (2014), and Penchel et al. (2019). In further analysis, the choke-ring is kept in its original dimensions.

Figure 23 – Reflection coefficients for analysed variations in the width of the outermost section of the choke-ring (w_o).

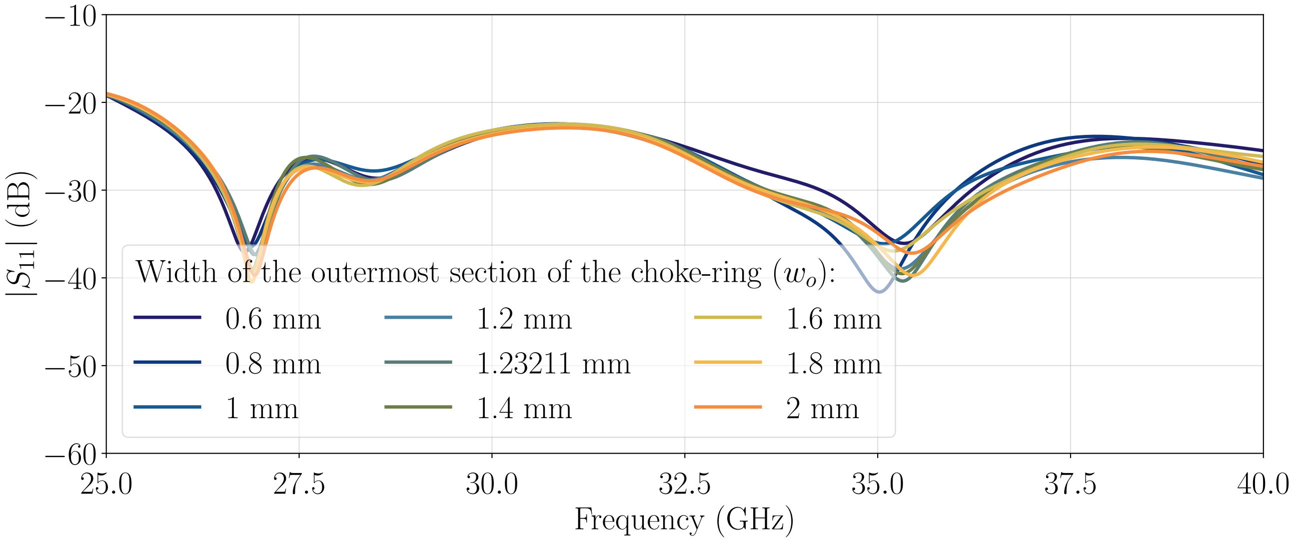

Source: Author.

Figure 24 – Radiation patterns of the coaxial horn (a) with choke-ring, and (b) without choke-ring.

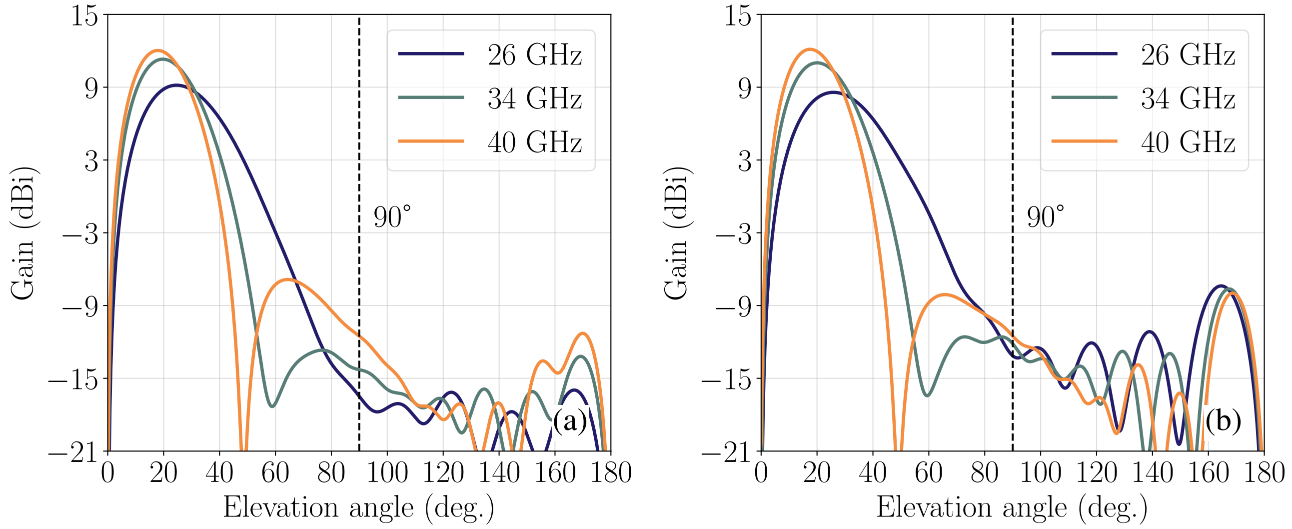

Source: Author.

Figure 25 – Reflection coefficient of the coaxial horn with and without a choke-ring.

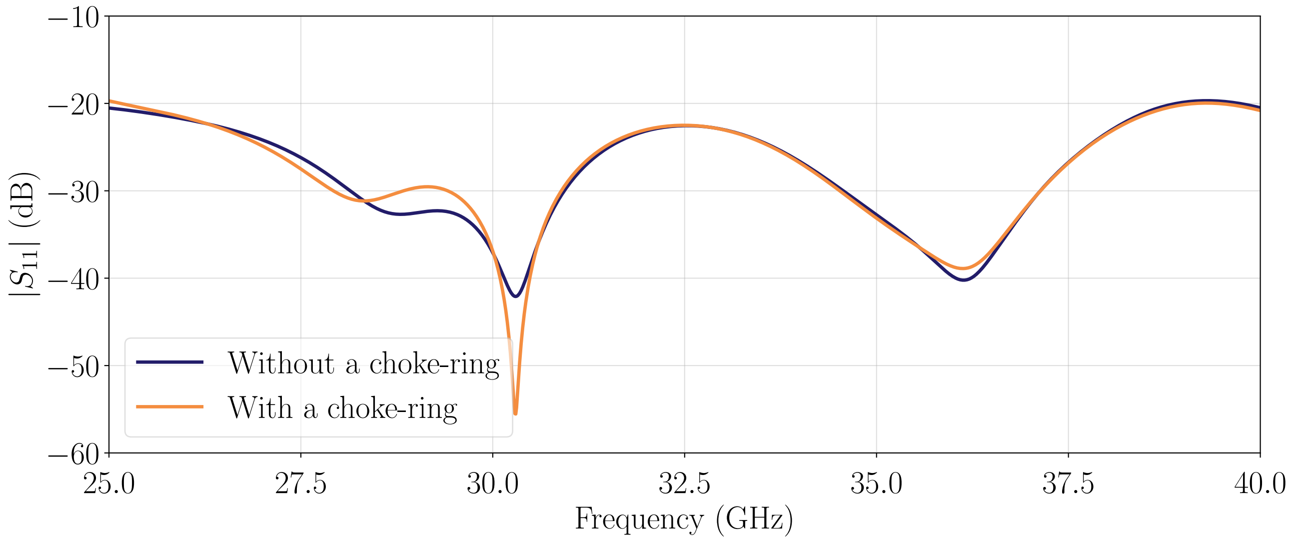

Source: Author.

4.2 CYLINDRICAL REGION

The cylindrical region is essentially a coaxial waveguide with a 50 Ω impedance termination. Modifications required in this region involved adding a mechanical support to the inner conductor. Nonetheless, the introduction of a dielectric with $\epsilon_r > 1$ in a region previously filled by air alters the impedance, requiring a solution for matching. Zang and Bergmann (2014) employed a cylindrical Teflon ($\epsilon_r = 2.1$) structure to achieve this by altering the cylindrical region radii and dimensioning the Teflon structure to minimize reflections. However, this approach resulted in a geometry posing manufacturing difficulties.

Several geometries, all illustrated in Figure 26, were tested with the aim of developing a new structure. This structure needed to serve as both a mechanical support for the inner conductor and an impedance matching element. Importantly, it should not negatively impact the performance of the coaxial horn and should also facilitate the manufacturing process. To achieve this, all geometries were designed to fit precisely in the space between the inner and outer conductor within the cylindrical region. Teflon was used as the material in the simulations.

Figure 26 – Geometries considered in the development of the impedance matching structure: (a) geometry 1, (b) geometry 2, (c) geometry 3, (d) geometry 4, (e) geometry 5, (f) geometry 6, (g) geometry 7, and (h) geometry 8.

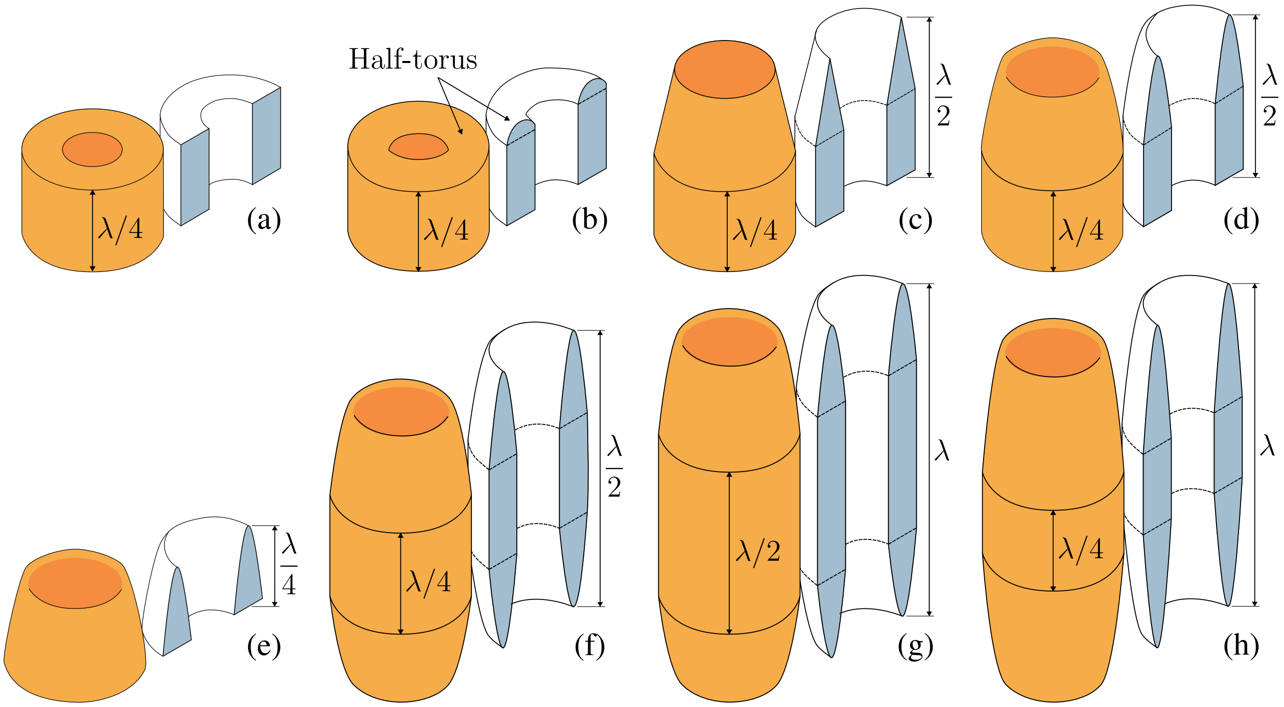

Source: Author.

Initially, the same cylindrical geometry used by Zang and Bergmann (2014) was applied in this work, but without altering the radii corresponding to the inner and outer conductor. This geometry is depicted in Figure 26(a). The dielectric cylinder was placed at the centre of the cylindrical region, its length was initially set to $\lambda/4$, and subsequently, a parametric analysis was conducted considering its length. Given that modifications to the cylindrical region do not result in significant changes in the radiation pattern, only the reflection coefficient was verified. The reflection coefficients for the parametric analysis of the length of the cylindrical support are presented in Figure 27. Observing the results, an increase in the length of the support improves performance at lower frequencies, whilst decreasing the support's length yields better results at higher frequencies. Generally, the use of the cylindrical support degrades the performance of the coaxial horn, leading to an increased reflection coefficient that remains between -20 dB and -10 dB for most of the frequency band.

Figure 27 – Reflection coefficients for the analysed variations in the length of the cylindrical support (geometry 1 in Figure 26).

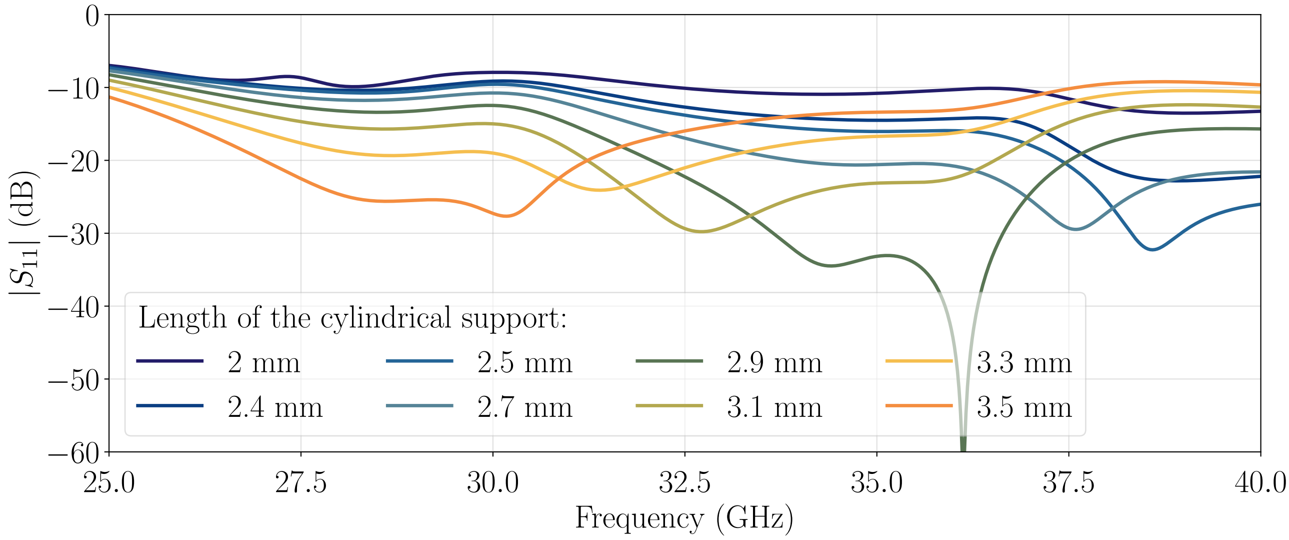

Source: Author.

Subsequently, the cylindrical support was positioned at the beginning of the cylindrical region (opposite to the start of the conical region), and additional elements were incorporated into the support geometry to ensure a smooth transition from Teflon to air. Geometry 2 included the addition of a half-torus, as illustrated in Figure 26(b); geometry 3 featured a triangle-shaped end part, depicted in Figure 26(c); geometry 4 introduced a half-ogival shape, as shown in Figure 26(d); and geometry 5 exclusively considered the half-ogival shape without the cylindrical component, presented in Figure 26(e). The half-ogival parts can be described in Cartesian coordinates by

$$x(t) = t, \tag{1}$$

$$y(t) = 0, \tag{2}$$

$$z(t) = \frac{l_s - l_{sc}}{2} - \frac{(l_s - l_{sc}) \cdot [2t - r_{c,o} - r_{c,i})]^2}{2 \cdot (r_{c,o} - r_{c,i})^2}, \tag{3}$$

where $r_{c,i} \leq t \leq r_{c,o}$, and the additional parameters are illustrated in Figure 12, and described in Table 2.

Afterwards, the performance of the coaxial horn was assessed with the support designed to provide a soft transition from air to Teflon and back to air. Three similar support geometries were examined, each comprising a cylindrical section and half-ogival end parts with equal lengths, positioned at the beginning and end of the cylindrical section. In Geometry 6 (Figure 26(f)), the total length was $\lambda/2$, with a $\lambda/4$-long cylindrical section, and each of the half-ogival shapes had a length of $\lambda/8$. Geometry 7

(Figure 26(g)) had a total length of λ and featured a $\lambda/2$-long cylindrical section. Lastly, Geometry 8 (Figure 26(h)) also had a total length of λ but featured a $\lambda/4$-long cylindrical section.

The reflection coefficient of the coaxial horn for each geometry is presented in Figure 28. Geometries 7 and 8 were observed to have the least negative impact on the performance of the coaxial horn, as evidenced by reflection coefficients that remained below -20 dB for the majority of the analysed frequency band. Both geometries are essentially the same, differing only in the proportions of the cylindrical and half-ogival sections. Therefore, later analyses will consider geometry 8.

Figure 28 – Reflection coefficients obtained for each geometry illustrated in Figure 26.

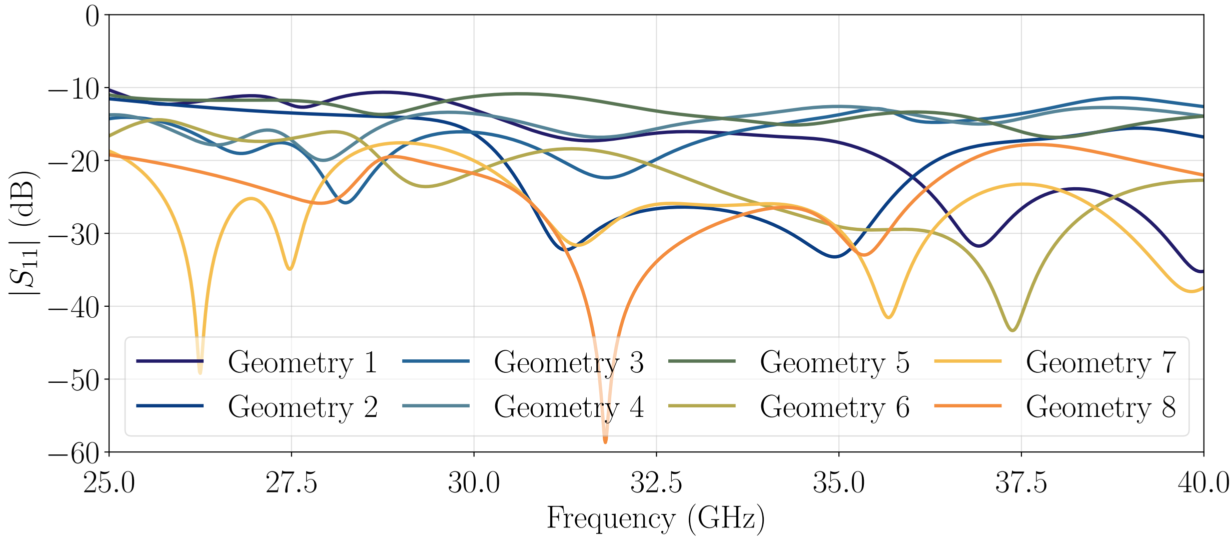

Source: Author.

4.3 TRANSITION REGION

Introducing the transition region was required due to a disparity between the radii in the cylindrical region and those of a standard commercial connector. Consequently, a region providing gradual adjustment in the radii was necessary to facilitate the connection of the coaxial horn with a commercial connector, preserving performance and ultimately transforming it into a functional prototype. As evident from Figure 29, simply inserting a connector without a transition region led to a degradation in the performance of the coaxial horn.

Initially, the transition region took the form of a $\lambda/4$-long section of coaxial waveguide, with inner and outer radii determined by the geometric mean between the radii of the cylindrical region and those of a commercial 2.92 mm connector, these initial dimensions are organized in Table 4, presented in Chapter 3. Following this, a parametric analysis explored variations in the length of the transition region (l_t), as well as in its inner ($r_{t,i}$) and outer ($r_{t,o}$) radii.

In the parametric analysis of l_t, seven variations were explored within a $\pm 50\%$ range of the original value (refer to Table 4). The parametric analysis of the transition region's radii, involved five variations of $r_{t,o}$ and five variations of $r_{t,i}$. The considered range ensured that the minimum value corresponded to the radii of a commercial 2.92 mm connector, while the maximum value aligned with the radii in the cylindrical region: $r_{t,o}^{\max} = r_{c,o}$ and $r_{t,i}^{\max} = r_{c,i}$. Since the addition of a transition region or any

Figure 29 – Reflection coefficients for the initial coaxial horn and for the coaxial horn with a connector but no transition region.

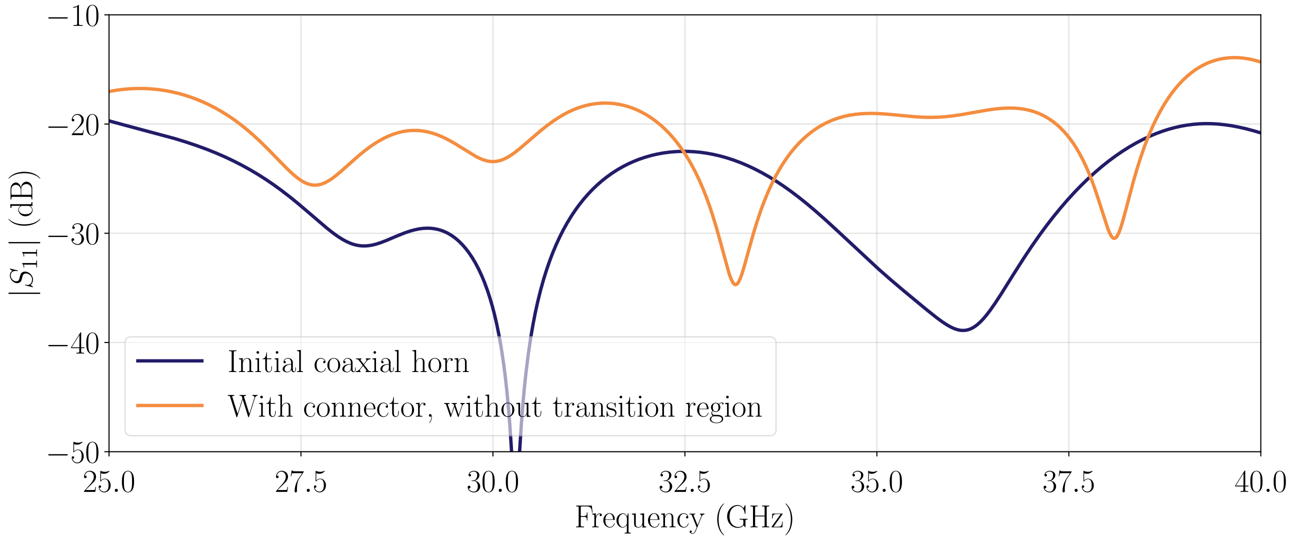

Source: Author.

modifications to it do not result in significant changes in the radiation pattern, only the reflection coefficient was verified.

The effect of modifying the length of the transition region is observed in Figure 30, which shows a frequency shift in the reflection coefficient, yet it consistently stays below −20 dB across the majority of the frequency band.

Figure 30 – Reflection coefficients for analysed variations in the transition region's length (l_t).

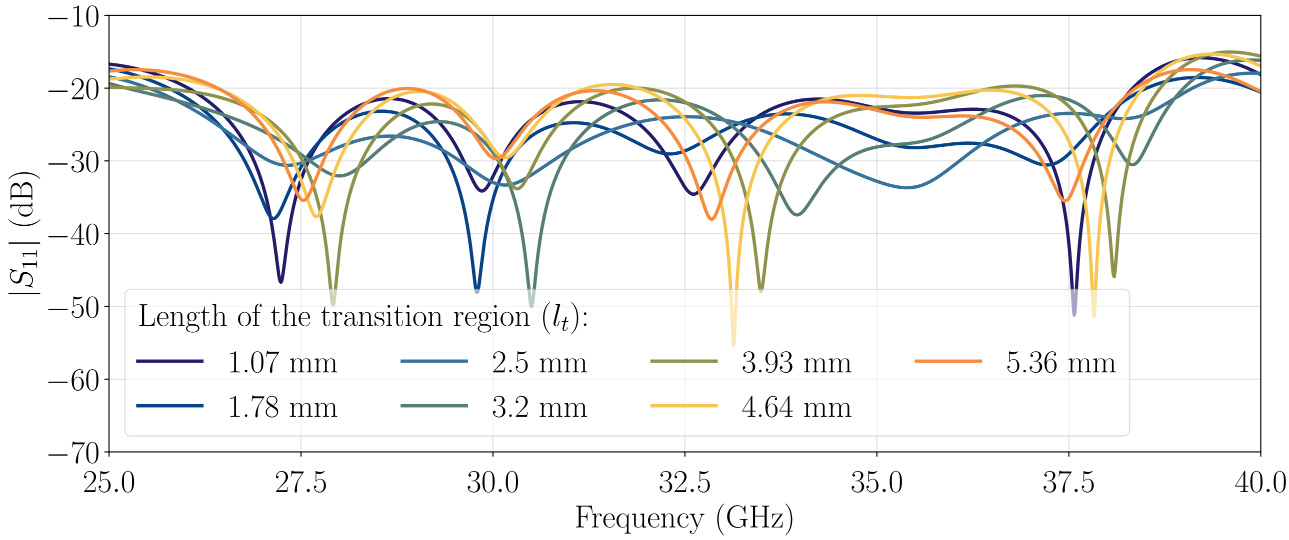

Source: Author.

The parametric analysis of the transition region's radii is presented in Figure 31. Generally, the smallest and largest values of $r_{t,o}$ resulted in higher reflection coefficients, while intermediary values exhibited lower reflection coefficients. Notably, smaller $r_{t,o}$ values correlated with lower reflection coefficients when $r_{t,i}$ was also minimized (refer to Figure 31(a) and Figure 31(b)), whereas the opposite trend was observed for larger $r_{t,o}$ (see Figure 31(e)). Values that led to the desired performance ($|S_{11}| < -20$ dB), such as the combination of $r_{t,o} = 1.59$ mm and $r_{t,i} = 0.68$ mm shown in Figure 31(c), closely matched the initial values (see Table 4).

Figure 31 – Reflection coefficients for analysed variations in the inner radius of the transition region ($r_{t,i}$), considering an outer radius ($r_{t,o}$) of (a) 1.27 mm, (b) 1.43 mm, (c) 1.59 mm, (d) 1.75 mm, and (e) 1.91 mm.

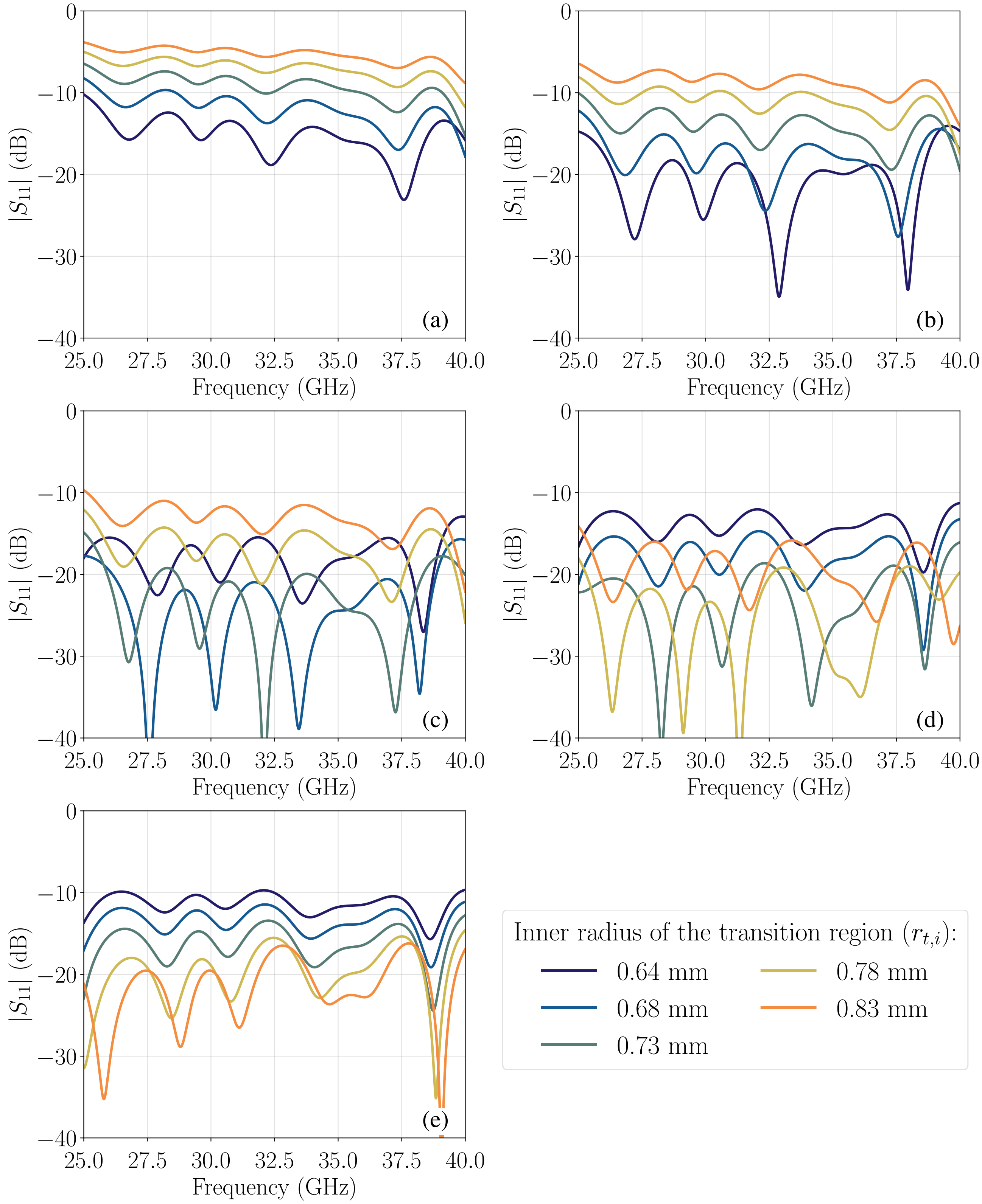

Source: Author.

After examining the coaxial horn, dielectric support, and transition region through parametric analysis, one can deduce the presence of a considerable number of variables to manage and optimize in alignment with the objectives outlined in Section 1.3. Consequently, to determine the optimized dimensions of the standard coaxial horn, GA was employed, as outlined in detail in Chapter 2.

Given that the goal of the standard coaxial horn was to convert the device presented by Penchel et al. (2019) into a functional prototype, the optimization focused exclusively on dimensions related to the added elements — the dielectric support and transition region. Simultaneously, dimensions related to the aperture were maintained as specified in Table 3. The dimensions considered for the GA optimization of the standard coaxial horn include: the transition region's inner radius ($r_{t,i}$), outer radius ($r_{t,o}$), and length (l_t); the total length of the support (l_s), and the length of the cylindrical section of the support (l_{sc}). These dimensions are illustrated in Figure 12. Since the considered parameters predominantly affected the reflection coefficient, a single goal was set in the GA algorithm: $|S_{11}| < -20$ dB for frequencies between 25 GHz and 40 GHz.

To establish the parameters' initial values and variation range for input into the GA algorithm, the results from the previously presented parametric analysis were taken into account. In the analysis of the dielectric support (Section 4.2), it was found that geometry 8 with $l_t = \lambda$ and $l_{sc} = \lambda/4$ produced the desired results ($|S_{11}| < -20$ dB), and these values were consequently considered. In the parametric analysis of the transition region presented in this section, it was noted that the values yielding the desired performance closely resembled the initial values specified in Table 4. Therefore, these initial values were retained as the starting values in the algorithm.

The optimization process was conducted in three steps, with each step considering a more refined variation range. In the initial step, parameters were allowed broader variations, approximately $\pm 50\%$ of their initial values. However, precautions were taken to limit these variations, ensuring that values chosen randomly by the algorithm in each iteration wouldn't lead to an impossible geometry, triggering errors and stopping the process. The total length of the dielectric support was constrained to not exceed the length of the cylindrical region, setting $l_t^{\text{max}} = l_c = \lambda$, and a minimum length of $l_t^{\text{min}} = \lambda/4$ was deemed suitable to adequately support the coaxial horn's inner conductor. The length of the support's cylindrical section was specified as a fraction of the support's total length, ranging from 0% to 90%. While a $\pm 50\%$ variation was permissible for the transition region's length and inner radius, careful attention was given to ensuring that the minimum value for the outer radius was slightly greater than the maximum value of the inner radius.

Upon observing parameter values nearing convergence in the initial step, the algorithm was stopped, and a second step commenced, considering the values that led to the best result in the first step as the initial values for the subsequent step. In this second step, GA was once again employed, allowing $\pm 10\%$ variations to the values of the parameters, while also considering the earlier observed limitations if applicable. After a sufficient number of iterations in the preceding step, where results closely approached convergence, a third and final step in the optimization process was initiated. In this step, a parametric analysis was conducted for each optimized parameter, simulating variations within $\pm 5\%$ of the values that produced the best result. This three-step approach aims to discover enhanced solutions by analysing the most relevant values, thus optimizing the use of computational resources.

A total of 745 and 750 iterations were analysed in the first and second optimization steps, respectively. The lowest cost obtained in the first step was slightly higher than one, and in the second step, a cost on the order of 10^{-2} was achieved. A cost equal to zero signifies that the objectives given to the algorithm are entirely fulfilled. Therefore, none of the analysed iterations fully met the defined objective. However, a slight improvement was observed in the third step with the parametric analysis, ultimately achieving the desired behaviour. The reflection coefficient and radiation pattern for the optimized standard coaxial horn are shown in Figure 32, while the values of the dimensions that produced this result are organized in Table 6.The optimized reflection coefficient consistently stayed below -20 dB across the entire frequency band, and as anticipated, the radiation pattern did not exhibit significant changes.

Figure 32 – (a) Reflection coefficient and (b) radiation patterns for the optimized standard coaxial horn.

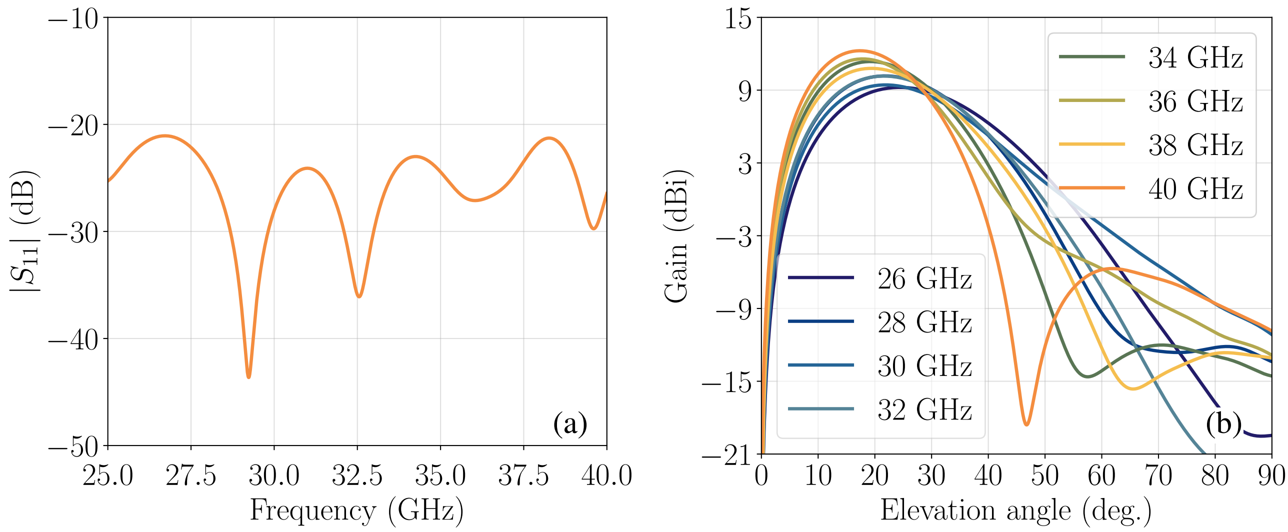

Source: Author.

Table 6 – Optimized dimensions of the standard coaxial horn.

Parameter	Value (λ)	Value (mm)	Parameter	Value (λ)	Value (mm)
$r_{a,i}$	0.350	3.750	$r_{c,i}$	0.077	0.825
$r_{a,o}$	0.960	10.280	$r_{c,o}$	0.178	1.907
d_s	0.270	2.893	l_c	1.000	10.714
w_s	0.085	0.911	l_s	0.924	9.900
w_i	0.040	0.428	l_{sc}	0.187	2.000
w_o	0.115	1.232	$r_{t,i}$	0.040	0.430
d	0.5	5.357	$r_{t,o}$	0.126	1.353
l	2.170	23.250	l_t	0.085	0.915

Source: Author.

5 SHAPED COAXIAL HORN

The shaped coaxial horn (see Figure 13) is primarily proposed to optimize the radiation pattern of the coaxial horn, aligning with the objectives of achieving more uniformity and the absence of nulls in elevation angles lower than 55°, as outlined in Section 1.3. This chapter will detail the modifications made to the conical region to realize these goals and provide insights into how the optimization process was conducted.

5.1 CONICAL REGION

A distinguishing feature of the shaped coaxial horn is the conical region for both inner and outer conductors, shaped by a cubic spline. The spline of the inner conductor comprises three control points, $r_n, n = 1, 2, 3$, representing the radial distance between each control point and the symmetry axis of the coaxial horn. For the outer conductor, three additional control points, $d_n, n = 1, 2, 3$, indicate the distance to the corresponding control point in the inner conductor, as illustrated in Figure 14, previously presented in Chapter 3. These three control points for both inner and outer conductors are evenly spaced along the length of the conical region.

After a thorough examination of the coaxial horn's behaviour using the literature or standard model, the primary goal for the shaped coaxial horn shifted to enhance its radiation characteristics. Consequently, GA optimization was promptly applied to achieve this objective, considering a broader set of dimensions. The dimensions considered for the GA optimization of the shaped coaxial horn include: the spline control points (r_n and d_n); the aperture's inner ($r_{a,i}$) and outer ($r_{a,o}$) radii; the length of the conical region (l); the cylindrical region's inner ($r_{c,i}$) and outer ($r_{c,o}$) radii; the transition region's inner radius ($r_{t,i}$), outer radius ($r_{t,o}$), and length (l_t); the total length of the support (l_s), and the length of the support's cylindrical section (l_{sc}). All dimensions are illustrated in Figure 14.

Recognizing the relevance of both the reflection coefficient and radiation pattern in this optimization process, two objectives were defined in the GA algorithm: one, $|S_{11}| < -20$ dB for frequencies between 25 GHz and 40 GHz; and two, maintaining a standard deviation of the gain below 0.5 dB for elevation angles between 5° and 40° throughout the analysed frequencies. The initial values entered into the algorithm were a combination of the values that yielded the best performance in the previous analyses, given in Section 4.1 for the aperture, in Section 4.2 for the dielectric support, and in Section 4.3 for the transition region. The initial values of the spline's control points were chosen to approximate the shape of the conical region to the original shape. All initial values for the shaped coaxial horn are detailed in Table 5, as introduced in Chapter 3.

The optimization process followed a three-step approach similar to the one outlined for the standard coaxial horn in Section 4.3. In the first step, a GA algorithm was applied, allowing a broad variation within a $\pm 50\%$ range of the initial values, with the same precautions detailed in Section 4.3. The second step involved another round of GA, narrowing down the parameter variations to within $\pm 10\%$ of the initial values, which were the values that led to the best result in the previous step. Finally, the third and final step utilized a parametric analysis to fine-tune the dimensions, considering a $\pm 5\%$ range of the initial values, which, once again, were the values that led to the best result in the previous step.

After 450 iterations, a cost on the order of 10^{-2} was already achieved in the first step. Refining the optimization interval in the second step further lowered the cost to the order of 10^{-4} after simulating 250 iterations. This result was subsequently enhanced through parametric analysis in the third step, successfully meeting the defined objective. The reflection coefficient and radiation pattern for the optimized standard coaxial horn are shown in Figure 33, while the values of the dimensions that produced this result are organized in Table 7. The optimized reflection coefficient consistently stayed below -20 dB across the entire frequency band, and as desired, the radiation pattern is now substantially more uniform, without nulls for elevation angles below 55°.

Figure 33 – (a) Reflection coefficient and (b) radiation patterns for the optimized shaped coaxial horn.

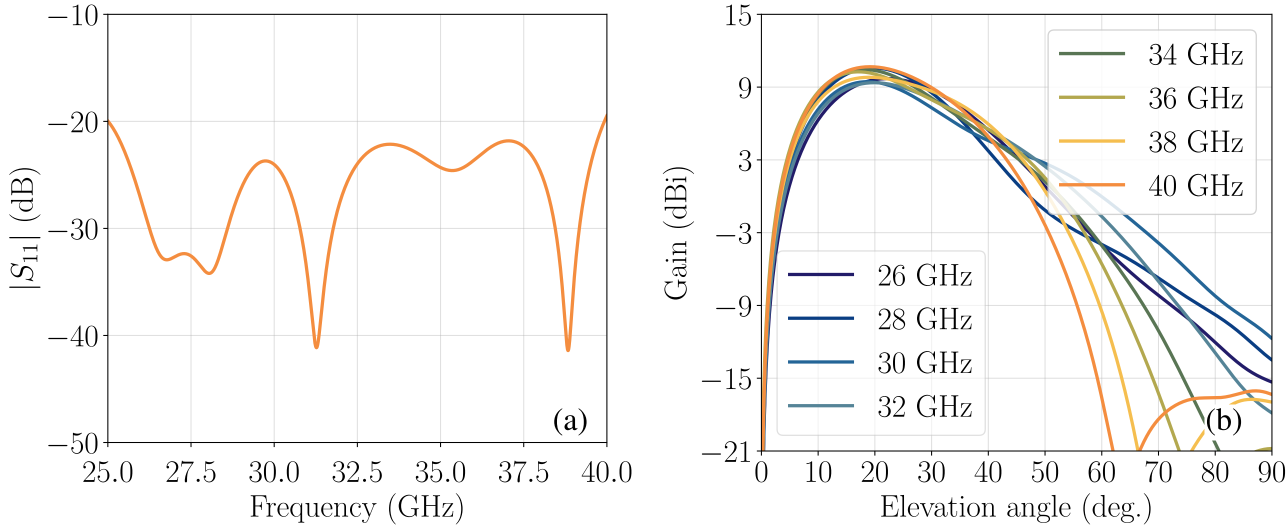

Source: Author.

Table 7 – Optimized dimensions of the shaped coaxial horn.

Parameter	Value (λ)	Value (mm)	Parameter	Value (λ)	Value (mm)
$r_{a,i}$	0.276	2.957	l_s	0.986	10.568
$r_{a,o}$	1.134	12.150	l_{sc}	0.168	1.800
d_s	0.270	2.893	$r_{t,i}$	0.039	0.418
w_s	0.085	0.911	$r_{t,o}$	0.109	1.164
w_i	0.040	0.428	l_t	0.125	1.340
w_o	0.115	1.232	r_1	0.126	1.346
d	0.500	5.357	r_2	0.148	1.585
l	1.890	20.249	r_3	0.245	2.626
$r_{c,i}$	0.065	0.697	d_1	0.250	2.678
$r_{c,o}$	0.173	1.857	d_2	0.481	5.158
l_c	1.000	10.714	d_3	0.722	7.731

Source: Author.

6 FABRICATION AND CHARACTERIZATION

The analysis and optimizations conducted thus far have resulted in two models for the coaxial horn, including all the mechanical elements required for a functioning prototype. Consequently, there is an intention for fabrication, with additive manufacturing being considered for this project. As of the preparation of this document, only the fabrication and characterization of the standard coaxial horn are available. This chapter will introduce the fabrication process, characterization, and present a parametric analysis investigating the discrepancies between measured and simulated results.

6.1 CONSIDERATIONS ABOUT THE FABRICATION PROCESS

While additive manufacturing may not offer high precision, it does result in less material waste compared to subtractive manufacturing. Intuitively, one might infer that additive manufacturing has a lower environmental impact, which is a primary motivation for its application in this project. However, it is important to note that this remains a research question under study. This project is anticipated to contribute to this investigation, but for this analysis, the focus has been specifically on the technical performance of the coaxial horn.

This project utilized a laser-based powder bed fusion process (L-PBF) for additive manufacturing. Among all the additive manufacturing processes reported for metallic materials, L-PBF is the most commonly consolidated variation for thin-diameter struts (thinner than 1 mm) or walls (MASKERY et al., 2015; PATTANAYAK et al., 2011). The metallic components (inner and outer conductors) were fabricated using an EOS M280 machine and gas-atomized maraging steel powder feedstock. No post-heat treatments or machining were applied to these components. The polymer component (dielectric support) was produced in a Formiga P110 machine using EOS polyamide 12 powders. The polymeric parts were fully dense with good-quality surfaces, and no post-processing was required. The fabricated coaxial horn is shown in Figure 34.

Figure 34 – (a) Fabricated standard coaxial horn with commercial connector, and (b) parts of the fabricated standard coaxial horn next to a ruler with millimetre and centimetre graduations.

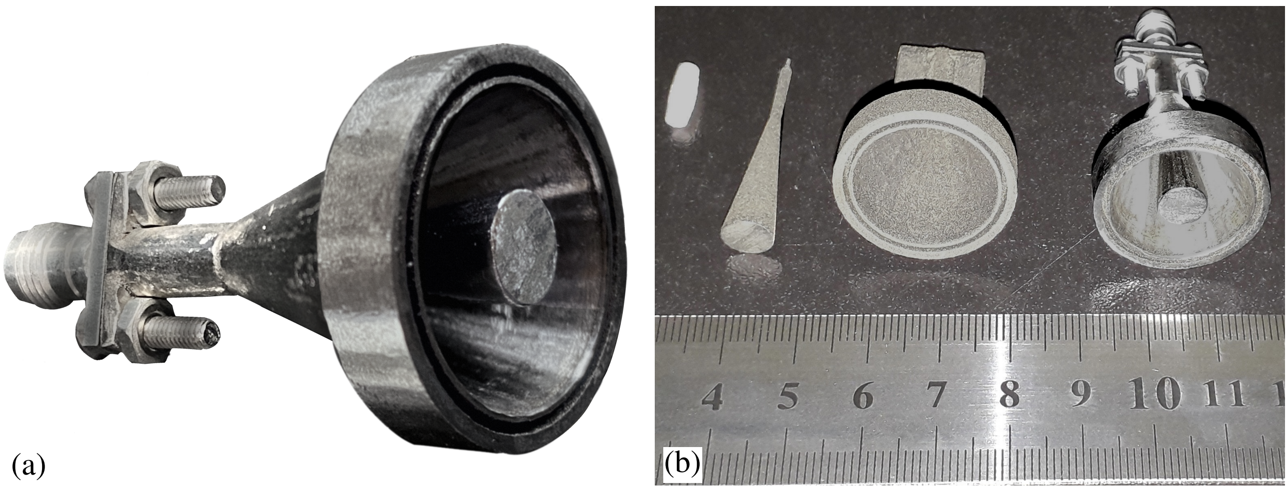

Source: Author and Guilherme Simon da Rosa.

6.2 CHARACTERIZATION

In the course of developing the two proposed prototypes, a 2.92 mm connector was considered, because it is suitable for frequencies up to 40 GHz, precisely the upper limit of the Ka band verified in all analyses. However, a possibility of evaluating the performance of the coaxial horn beyond 40 GHz became available. This is particularly interesting because, during development, a 20 dB impedance bandwidth was achieved throughout the Ka band, a more stringent requirement than the more commonly used 10 dB bandwidth. This suggests that the commercially acceptable bandwidth is larger than the Ka band, and the coaxial horn is operational beyond 40 GHz. Consequently, for the measurements, a 2.4 mm connector, which can be used up to 50 GHz (FAIRVIEW MICROWAVE, 2020), was used instead of the initially considered 2.92 mm connectors. The change in connector altered the performance of the coaxial horn, that was optimized to work with 2.92 mm connectors. Nonetheless, with new simulations performed considering a 2.4 mm connector, it is still valid to consider the altered result with the objective of validating the design process.

The measurements were performed with a Keysight FieldFox N9951A network analyser, and the obtained results are then compared with the simulated outcomes in Figure 35. One can note that the measured reflection coefficient (see Figure 35(a)) exhibits poorer performance at higher frequencies. Similarly, the radiation pattern (Figure 35(b)) shows good alignment between measurements and simulations at lower frequencies, but discrepancies become more noticeable at higher frequencies, especially for elevation angles higher than 40°.

Figure 35 – Comparison between measured and simulated results of the (a) reflection coefficient, and the (b) radiation patterns.

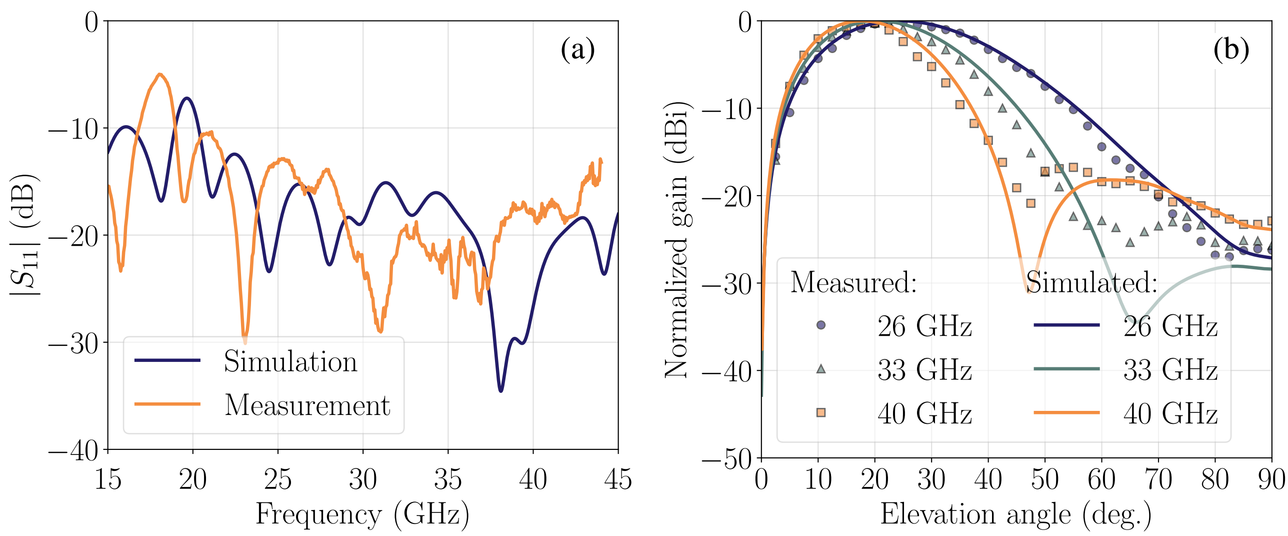

Source: Author.

Discrepancies between measurement and simulation results may be attributed to factors in the fabrication process, such as different roughness values on surfaces based on the building fabrication direction or crystallographic textures, as reported for additive manufacturing by L-PBF (LIU et al., 2023). While these influencing factors could impact antenna performance, future studies are required to comprehend and quantify their role in the reflection coefficient and radiation patterns.

Still, in order to investigate some other features affecting the performance of the antenna, several parametric analyses were conducted and are presented in Figure 36 and Figure 37.

Figure 36 – Simulated reflection coefficients for variations in the (a) dielectric constant (ϵ_r), (b) dielectric loss tangent ($\tan\delta$), (c) position of the dielectric support, and (d) position of the inner conductor.

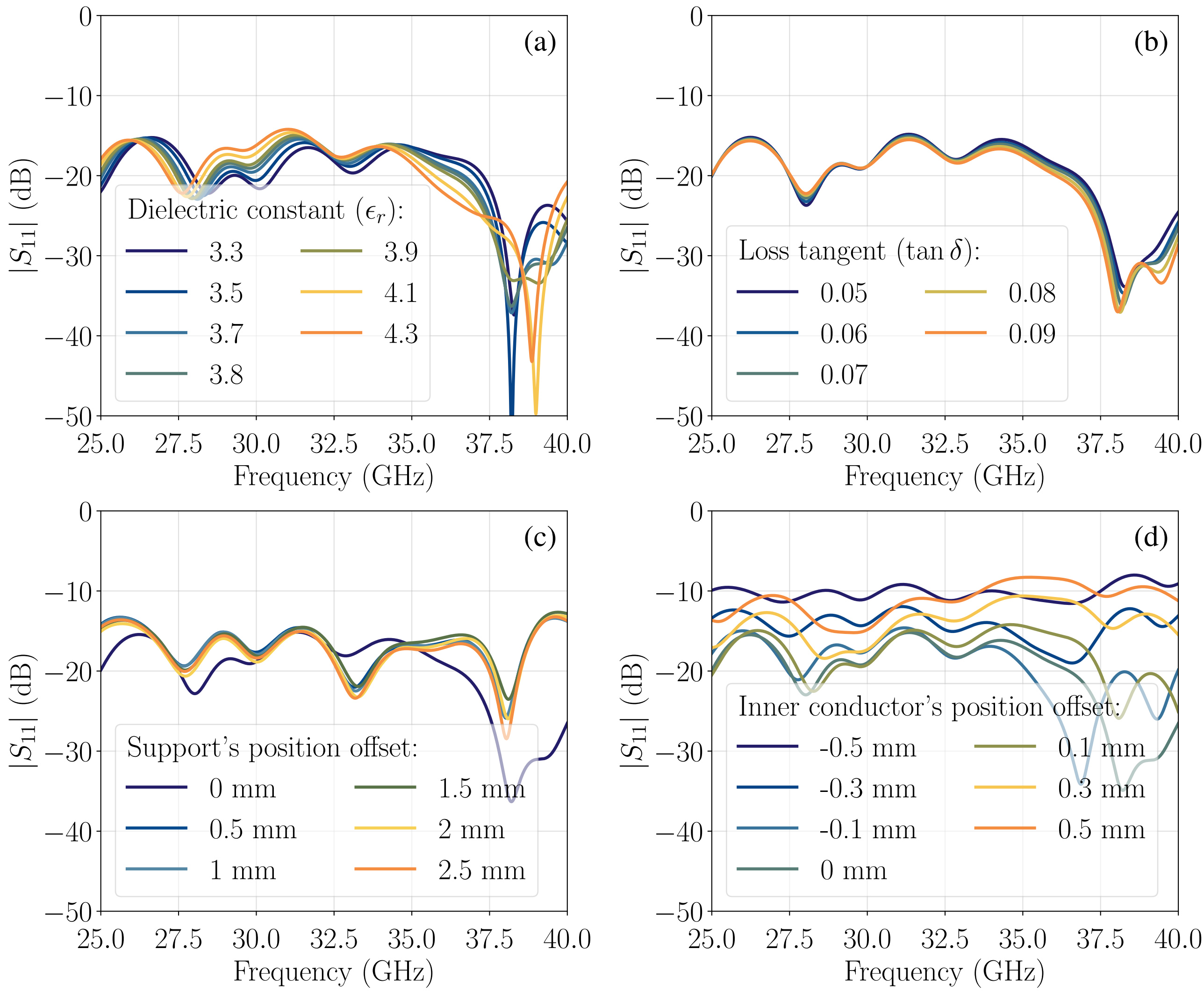

Source: Author.

The first two analyses involved varying the electrical properties (ϵ_r and $\tan\delta$) of the dielectric support material, as these properties were not well-documented at high frequencies for the material used in the fabrication (EOS GMBH, 2010). In Figure 36(a), where variations in ϵ_r were examined, a slight frequency shift in the reflection coefficient can be observed. The discrepancies become more pronounced above 37.5 GHz, but they do not fully explain the observed differences in the measurements shown in Figure 35(a). Similarly, as shown in Figure 36(b), variations of the dielectric loss tangent do not lead to significant changes in the reflection coefficient.

During the assembly of the coaxial horn, it is possible that the dielectric support is not perfectly centred within the cylindrical region. This could potentially lead to an impedance mismatch and affect the performance of the coaxial horn. To investigate this, a parametric analysis was conducted to examine the effect of offsetting the support position along the cylindrical region. However, only offsets towards the conical region were considered, as the opposite direction, towards the connector, does not

Figure 37 – Simulated radiation patterns for variations in the position of the inner conductor for (a) 26 GHz, (b) 33 GHz, and (c) 40 GHz.

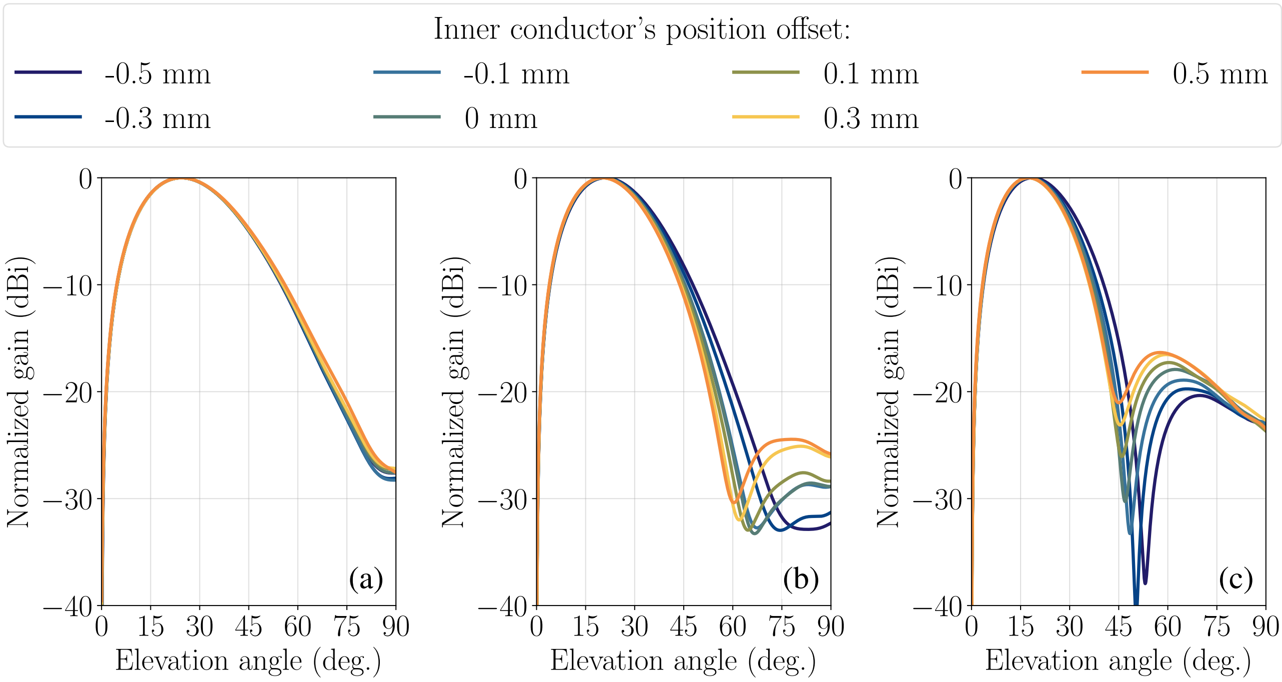

Source: Author.

allow for significant deviations due to the presence of the transition region (see Figure 12). The results presented in Figure 36(c) indicate that the offset does have a small impact on the reflection coefficient.

The positioning of the inner conductor can also be affected in the assembly process. This has the potential to impact both the reflection coefficient and radiation pattern, as it directly changes the geometry of the aperture. To investigate this effect, deviations in the position of the inner conductor were analysed, considering positive offsets when the movement is towards the aperture and negative offsets in the opposite direction. Figure 36(d) presents the reflection coefficient for each analysed offset. Significant changes in performance are observed even for offsets that are a small fraction of the wavelength. Additionally, we examined the impact of the inner conductor's positioning on the radiation pattern, as shown in Figure 37. At 26 GHz (Figure 37(a)), the position of the inner conductor has a negligible effect on the radiation pattern. However, as the frequency increases, the intensity of the observable impact on the radiation pattern also increases. This is particularly evident when examining the behaviour of the radiation pattern at 40 GHz, as depicted in Figure 37(c). This observation may help to explain the discrepancies observed between the measurements at the highest frequencies.

6.3 COMPARISON WITH STATE-OF-THE-ART AND COMMERCIAL SOLUTIONS

Table 8 presents a performance comparison between the fabricated standard coaxial horn and other state-of-the-art antenna designs from the literature, along with commercial solutions for omnidirectional antennas operating at the Ka band. The coaxial horn proposed in this work stands out with the largest 10 dB impedance bandwidth and the second-highest peak realized gain, surpassed only by the antenna presented by Feng et al. (2023). Additionally, it occupies the third-smallest volume, following behind Fan et al. (2018) and Wu et al. (2020), which demonstrates a very competitive performance.

Table 8 – Performance comparison of the fabricated standard coaxial horn antenna with other conical-beam antenna designs and commercial solutions for mm-wave applications.

Reference	f_0 (GHz)	BW (%)	$G_{\text{re,peak}}$ (dBi)	Dimensions (λ_0^3)
(ZHANG; LEUNG; LU, 2023)	32.50	43.90	9.20	$5.60 \times 5.60 \times 5.70$
(WU et al., 2020)	35.75	60.70	11.40	$2.38 \times 2.38 \times 1.88$
(FAN et al., 2018)	44.15	22.90	6.00	$0.82 \times 0.82 \times 0.02$
(PHAM; LEE; LIM, 2021)	28.30	11.60	8.51	$4.53 \times 4.53 \times 0.47$
(FENG et al., 2023)	26.00	11.40	11.60	$5.48 \times 5.48 \times 0.78$
(PASTERNACK, 2019)	28.75	15.65	7.50	$14.48 \times 14.48 \times 8.61$
(ERAVANT, 2018a)	34.75	30.22	3.00	$5.29 \times 5.29 \times 4.02$
(ERAVANT, 2018b)	33.25	40.60	3.00	$4.79 \times 4.79 \times 5.16$
This work	31.50	79.36	11.53	$2.61 \times 2.61 \times 3.66$

f_0: centre frequency, BW: 10 dB impedance bandwidth, $G_{\text{re,peak}}$: peak realized gain

Source: Author, Rafael Abrantes Penchel and Guilherme Simon da Rosa.

7 CONCLUSIONS

This work presented the electromagnetic analysis and optimization of a coaxial horn operating in the Ka band, aligning with the trend towards the development of millimetre wave devices for future generations of international mobile telecommunications. Two models of coaxial horns were analysed and optimized: the standard coaxial horn and the shaped coaxial horn.

The study of the standard coaxial horn served two purposes: first, to analyse the impact of different device dimensions on the reflection coefficient and radiation pattern; and second, to develop a practical prototype of the coaxial horn previously presented in the literature. Analyses for its aperture, cylindrical, and transition regions were conducted.

The study of the aperture considered the radii of the inner and outer conductors forming the aperture, along with the dimensions of the choke-ring placed at the aperture. The analyses revealed that the choke-ring had a significant effect only in the radiation pattern, for elevation angles higher than 90°, and variations in the aperture's radii were associated with patterns of improvement or degradation in the reflection coefficient and radiation pattern, in preparation for subsequent stages in this work.

Modifications to the cylindrical region involved the addition of a mechanical support to the inner conductor, which also served as an impedance-matching element. Eight geometries precisely fitting between the cylindrical region of inner and outer conductors were considered. The aim was to provide a soft transition between air and Teflon, and the final geometry chosen was the one that least negatively affected the performance.

The transition region was introduced to provide a gradual adjustment of the radii from the cylindrical region to those of a standard commercial connector. Lastly, an optimization using a GA was conducted to define the final dimensions for the standard coaxial horn. The optimization considered the transition region's inner radius, outer radius, and length, along with the total length of the dielectric support and the length of the support's cylindrical section. The optimized reflection coefficient consistently stayed below -20 dB across the entire frequency band, and as anticipated, the radiation pattern did not exhibit significant changes.

The primary purpose of the shaped coaxial horn is to optimize its radiation pattern. Characterized by a conical region for both inner and outer conductors shaped by a cubic spline, the shaped coaxial horn promptly went through a GA optimization process which involved a broader set of dimensions. Initial values and variation ranges for the dimensions were determined based on previous analysis of the standard coaxial horn. Dimensions considered for the optimization included the control points of the spline, radii of the aperture, length of the conical region, radii of the cylindrical region, dimensions of the transition region, and lengths of the dielectric support. The optimized shaped coaxial horn achieved a reflection coefficient below -20 dB across the frequency band, and the radiation pattern is now substantially more uniform, without nulls for elevation angles below 55°.

This document concludes by presenting the fabrication process and characterization of the standard coaxial horn, along with a parametric analysis addressing discrepancies between measured and simulated results. The fabricated standard coaxial horn proposed in this work stands out among the consulted references for having the largest 10 dB impedance bandwidth, the second-highest peak realized gain, and the third-smallest volume.

REFERENCES

ALSABAH, M. et al. 6G Wireless Communications Networks: A Comprehensive Survey. **IEEE Access**, v. 9, p. 148191–148243, 2021. ISSN 2169-3536.

ALWIS, C. D. et al. Survey on 6G Frontiers: Trends, Applications, Requirements, Technologies and Future Research. **IEEE Open Journal of the Communications Society**, v. 2, p. 836–886, 2021. ISSN 2644-125X.

ANATEL. **Ato nº 8995**. 2022. Agência Nacional de Telecomunicações, Brasil. Online, accessed 19 nov. 2023. Available at: <https://sei.anatel.gov.br/sei/publicacoes/controlador_publicacoes.php?acao=publicacao_visualizar&id_documento=9841413&id_orgao_publicacao=0>.

ANATEL. **Consulta Pública nº 11**. 2022. Agência Nacional de Telecomunicações, Brasil. Online, accessed 19 nov. 2023. Available at: <https://sistemas.anatel.gov.br/SACP/Contribuicoes/TextoConsulta.asp?CodProcesso=C2590&Tipo=1&Opcao=andamento>.

ANSYS. **Ansys Electronics: Electromagnetic, Signal Integrity, Thermal and Electro-Mechanical Simulation Solutions**. 2023. Online, accessed 28 nov. 2023. Available at: <https://www.ansys.com/products/electronics>.

ANSYS. **HFSS Help Release 2023 R1**. 2023.

BALANIS, C. A. **Antenna Theory: Analysis and Design**. Hoboken, New Jersey - United States of America: John Wiley & Sons, 2016. ISBN 978-1-118-642060-1.

BERGMANN, J. R.; MOREIRA, F. J. S. An Omnidirectional ADE Reflector Antenna. **Microwave and Optical Technology Letters**, v. 40, n. 3, p. 250–254, 2004. ISSN 1098-2760.

CHOUDHURY, D. 5G Wireless and Millimeter Wave Technology Evolution: An Overview. In: **2015 IEEE MTT-S International Microwave Symposium**. [S.l.: s.n.], 2015. p. 1–4. ISSN: 0149-645X.

EOS GMBH. **Product Information: PA2200**. 2010. Online, accessed 05 dec. 2023. Available at: <https://www.epmi-impression-3d.com/pdf/EOS_PA12.pdf>.

ERAVANT. **SAO-2434030345-KF-R1 Ka-Band Omnidirectional Antenna Datasheet**. 2018. Online, accessed 25 aug. 2023. Available at: <https://sftp.eravant.com/content/datasheets/SAO-2434030345-KF-R1.pdf>.

ERAVANT. **SSAO-2734033045-KF-C1-BL Ka-Band Omnidirectional Amplified Antenna Datasheet**. 2018. Online, accessed 25 aug. 2023. Available at: <https://sftp.eravant.com/content/datasheets/SAO-2734033045-KF-C1-BL.pdf>.

ERICSSON. **Ericsson Mobility Report June 2019**. 2019. Online, accessed 28 nov. 2023. Available at: <https://www.ericsson.com/4ac661/assets/local/reports-papers/mobility-report/documents/2019/ericsson-mobility-report-june-2019.pdf>.

ERICSSON. **Ericsson Mobility Report June 2023**. 2023. Online, accessed 28 nov. 2023. Available at: <https://www.ericsson.com/en/reports-and-papers/mobility-report/reports/june-2023>.

ETSI. **3GPP TR 21.915 version 15.0.0 Release 15**. France, 2019. 120 p. European Telecommunications Standards Institute. Online, accessed 28 nov. 2023. Available at: <https://www.etsi.org/deliver/etsi_tr/121900_121999/121915/15.00.00_60/tr_121915v150000p.pdf>.

FAIRVIEW MICROWAVE. **FMCN1679 2.4 mm Connector Datasheet**. 2020. Online, accessed 05 dec. 2023. Available at: <https://www.fairviewmicrowave.com/images/productPDF/FMCN1679.pdf>.

FAN, K. et al. Wideband Horizontally Polarized Omnidirectional Antenna With a Conical Beam for Millimeter-Wave Applications. **IEEE Transactions on Antennas and Propagation**, v. 66, n. 9, p. 4437–4448, 2018.

FCC; NTIA. **United States Frequency Allocations**. 2016. Federal Communications Comission and National Telecommunications and Information Administration. Online, accessed 19 nov. 2023. Available at: <https://www.ntia.gov/sites/default/files/publications/january_2016_spectrum_wall_chart_0.pdf>.

FENG, B. et al. A Dual-Polarized Shared-Aperture Antenna With Conical Radiation Patterns and High Gain for 5G Millimeter-Wave Ceiling Communications. **IEEE Transactions on Antennas and Propagation**, v. 71, n. 3, p. 2278–2289, 2023.

FERNÁNDEZ-ARDÈVOL, M. **Mobile Communication and Socio-Economic Development: A Latin American Perspective**. 2011. Online, accessed 05 nov. 2023. Available at: <https://www.un.org/en/chronicle/article/mobile-communication-and-socio-economic-development-latin-american-perspective>.

GIORDANI, M. et al. Toward 6G Networks: Use Cases and Technologies. **IEEE Communications Magazine**, v. 58, n. 3, p. 55–61, mar. 2020. ISSN 1558-1896.

ISED. **Canadian Table of Frequency Allocations – GHz**. 2022. Innovation, Science and Economic Development Canada. Online, accessed 19 nov. 2023. Available at: <https://ised-isde.canada.ca/site/spectrum-management-telecommunications/en/learn-more/key-documents/consultations/canadian-table-frequency-allocations-sf10759#s2.3>.

ITU. **IMT Vision – Framework and Overall Objectives of the Future Development of IMT for 2020 and Beyond**. Geneva, 2015. 21 p. International Telecommunication Union. Online, accessed 26 apr. 2021. Available at: <https://www.itu.int/dms_pubrec/itu-r/rec/m/R-REC-M.2083-0-201509-I!!PDF-E.pdf>.

ITU. **Minimum Requirements Related to Technical Performance for IMT-2020 Radiointerface(s)**. Geneva, 2017. 11 p. International Telecommunication Union. Online, accessed 26 apr. 2021. Available at: <https://www.itu.int/dms_pub/itu-r/opb/rep/R-REP-M.2410-2017-PDF-E.pdf>.

ITU. **Resolution 242 (WRC-19): Terrestrial Component of International Mobile Telecommunications in the Frequency Band 24.25-27.5 GHz**. 2019. International Telecommunications Union. Online, accessed 22 nov. 2023. Available at: <https://www.itu.int/dms_pub/itu-r/oth/0C/0A/R0C0A00000F0080PDFE.pdf>.

ITU. **Resolution 243 (WRC-19): Terrestrial Component of International Mobile Telecommunications in the Frequency Bands 37-43.5 GHz and 47.2-48.2 GHz**. 2019. International Telecommunications Union. Online, accessed 22 nov. 2023. Available at: <https://www.itu.int/pub/R-ACT-WRC.14-2019/en>.

ITU. **World Radiocommunication Conference 2019 (WRC-19) - Final Acts**. 2019. International Telecommunications Union. Online, accessed 22 nov. 2023. Available at: <https://www.itu.int/pub/R-ACT-WRC.14-2019/en>.

ITU. **Recommendation ITU-R P.676-13 - Attenuation by atmospheric gases and related effects**. 2022. International Telecommunications Union. Online, accessed 03 sep. 2023. Available at: <https://www.itu.int/dms_pubrec/itu-r/rec/p/R-REC-P.676-13-202208-I!!PDF-E.pdf>.

LIU, J. et al. Laser Powder Bed Fusion of 316L Stainless Steel: Effect of Laser Polishing on the Surface Morphology and Corrosion Behavior. **Micromachines**, MDPI, v. 14, 4 2023. ISSN 2072666X.

MA, J. et al. Invited Article: Channel Performance for Indoor and Outdoor Terahertz Wireless Links. **APL Photonics**, v. 3, p. 051601, feb. 2018.

MARCUS, M.; PATTAN, B. Millimeter Wave Propagation: Spectrum Management Implications. **IEEE Microwave Magazine**, v. 6, n. 2, p. 54–62, jun. 2005. ISSN 1557-9581.

MASKERY, I. et al. Mechanical Properties of Ti-6Al-4V Selectively Laser Melted Parts with Body-Centred-Cubic Lattices of Varying cell size. **Experimental Mechanics**, Springer New York LLC, v. 55, p. 1261–1272, 9 2015. ISSN 17412765.

MOREIRA, F. da S.; BERGMANN, J. Axis-Displaced Dual-Reflector Antennas for Omnidirectional Coverage With Arbitrary Main-Beam Direction in the Elevation Plane. **IEEE Transactions on Antennas and Propagation**, v. 54, n. 10, p. 2854–2861, oct. 2006. ISSN 1558-2221.

NGMN ALLIANCE. **5G White Paper**. 2015. Online, accessed 26 apr. 2021. Available at: <https://www.ngmn.org/work-programme/5g-white-paper.html>.

NTRA. **National Frequency Allocation Table**. 2021. National Telecommunications Regulatory Autority, Arab Republic of Egypt. Online, accessed 19 nov. 2023. Available at: <https://www.tra.gov.eg/wp-content/uploads/2021/06/EGY-NTRA-June21-NFAT-1.pdf>.

OFCA. **Hong Kong Table of Frequency Allocations**. 2023. Office of the Communications Authority. Online, accessed 19 nov. 2023. Available at: <https://www.ofca.gov.hk/filemanager/ofca/common/Industry/broadcasting/hk_freq_table_en.pdf>.

PASTERNACK. **PEWAN1133 Waveguide Omni-directional Antenna Datasheet**. 2019. Online, accessed 25 aug. 2023. Available at: <https://www.pasternack.com/images/ProductPDF/PEWAN1133.pdf>.

PATTANAYAK, D. K. et al. Bioactive Ti Metal Analogous to Human Cancellous Bone: Fabrication by Selective Laser Melting and Chemical Treatments. **Acta Biomaterialia**, Elsevier, v. 7, p. 1398–1406, 3 2011. ISSN 1742-7061.

PENCHEL, R. et al. GO Shaping of Omnidirectional Dual-Reflector Antennas with Arbitrary Main-Beam Direction in Elevation Plane by Connecting Conic Sections. **International Journal of Antennas and Propagation**, v. 2018, p. 1–9, mar. 2018.

PENCHEL, R. A.; BERGMANN, J. R.; MOREIRA, F. J. S. Main-Reflector Shaping of Omnidirectional Dual Reflectors Using Local Conic Sections. **IEEE Transactions on Antennas and Propagation**, v. 61, n. 8, p. 4379–4383, aug. 2013. ISSN 1558-2221.

PENCHEL, R. A. et al. Design of Wideband Omnidirectional Dual-Reflector Antennas in Millimeter Waves. **IEEE Antennas and Wireless Propagation Letters**, v. 18, n. 5, p. 906–910, may 2019. ISSN 1548-5757.

PHAM, D. A.; LEE, M.; LIM, S. High-Gain Conical-Beam Planar Antenna for Millimeter-Wave Drone Applications. **IEEE Transactions on Antennas and Propagation**, v. 69, n. 10, p. 6959–6964, 2021.

PI, Z.; KHAN, F. An Introduction to Millimeter-Wave Mobile Broadband Systems. **IEEE Communications Magazine**, v. 49, n. 6, p. 101–107, jun. 2011. ISSN 1558-1896.

PORTILLO, I. del. **ITU-Rpy: A Python Implementation of the ITU-R P. Recommendations to Compute Atmospheric Attenuation in Slant and Horizontal Paths.** GitHub, 2017. Online, accessed 03 sep. 2023. Available at: <https://github.com/inigodelportillo/ITU-Rpy/>.

RAPPAPORT, T. S. et al. Overview of Millimeter Wave Communications for Fifth-Generation (5G) Wireless Networks—With a Focus on Propagation Models. **IEEE Transactions on Antennas and Propagation**, v. 65, n. 12, p. 6213–6230, dec. 2017. ISSN 1558-2221.

SADIKU, M. A Simple Introduction to Finite Element Analysis of Electromagnetic Problems. **IEEE Transactions on Education**, v. 32, n. 2, p. 85–93, may 1989. ISSN 1557-9638.

WEI, L. et al. Key Elements to Enable Millimeter Wave Communications for 5G Wireless Systems. **IEEE Wireless Communications**, v. 21, n. 6, p. 136–143, dec. 2014. ISSN 1558-0687.

WELLS, J. Faster than Fiber: The Future of Multi-G/s Wireless. **IEEE Microwave Magazine**, v. 10, n. 3, p. 104–112, may 2009. ISSN 1557-9581.

WU, L. et al. 3-D Printed Wideband Millimeter-Wave Horn Antenna With Conical Radiation Pattern. **IEEE Antennas Wireless Propagation Letters**, v. 19, n. 3, p. 453–456, 2020.

ZANG, S. R.; BERGMANN, J. R. Analysis of Omnidirectional Dual-Reflector Antenna and Feeding Horn Using Method of Moments. **IEEE Transactions on Antennas and Propagation**, v. 62, n. 3, p. 1534–1538, mar. 2014. ISSN 1558-2221.

ZANG, S. R. et al. Análise de Estabilidade do Diagrama de Radiação ao Longo da Banda de Uma Corneta Coaxial TEM. In: **18 SBMO - Simpósio Brasileiro de Microondas e Optoeletrônica e 13 CBMAG - Congresso Brasileiro de Eletromagnetismo**. [S.l.: s.n.], 2018. p. 405–408.

ZHANG, Z.-Y.; LEUNG, K. W.; LU, K. Wideband High-Gain Omnidirectional Biconical Antenna for Millimeter-Wave Applications. **IEEE Transactions on Antennas and Propagation**, v. 71, n. 1, p. 58–66, 2023.

APPENDIX A – DETAILED RESULTS FROM THE ANALYSES OF THE APERTURE'S RADII, FOR $\mathbf{r_{a,o}} < 1\lambda$

Figure 38 – Reflection coefficients for analysed variations in the inner radius of the aperture ($r_{a,i}$), for an outer radius ($r_{a,o}$) of 0.80λ.

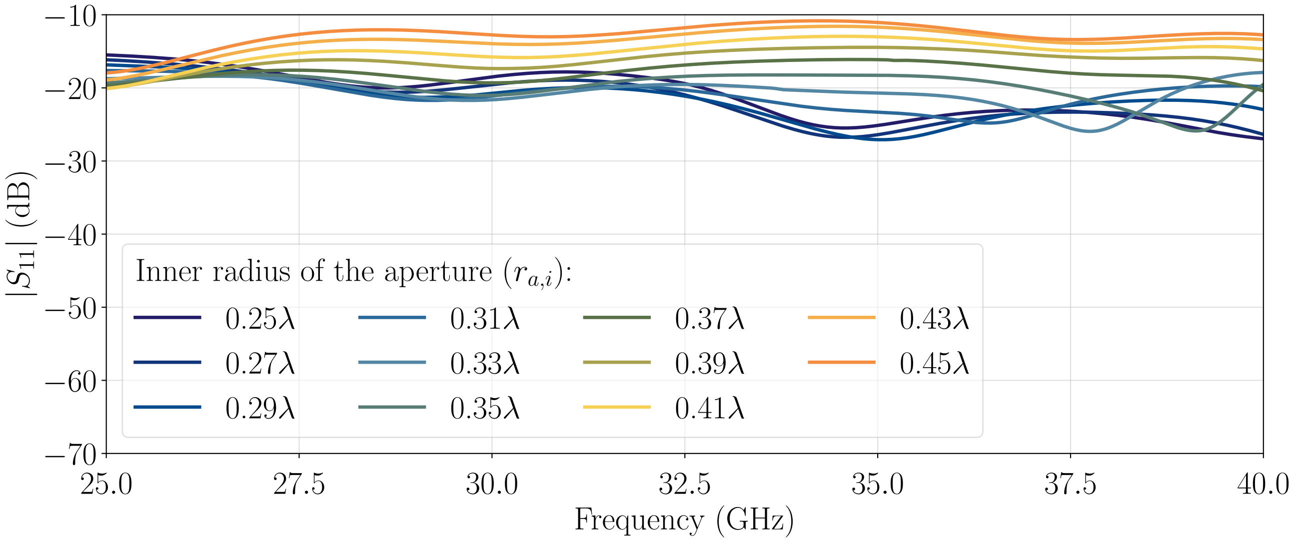

Source: Author.

Figure 39 – Reflection coefficients for analysed variations in the inner radius of the aperture ($r_{a,i}$), for an outer radius ($r_{a,o}$) of 0.84λ.

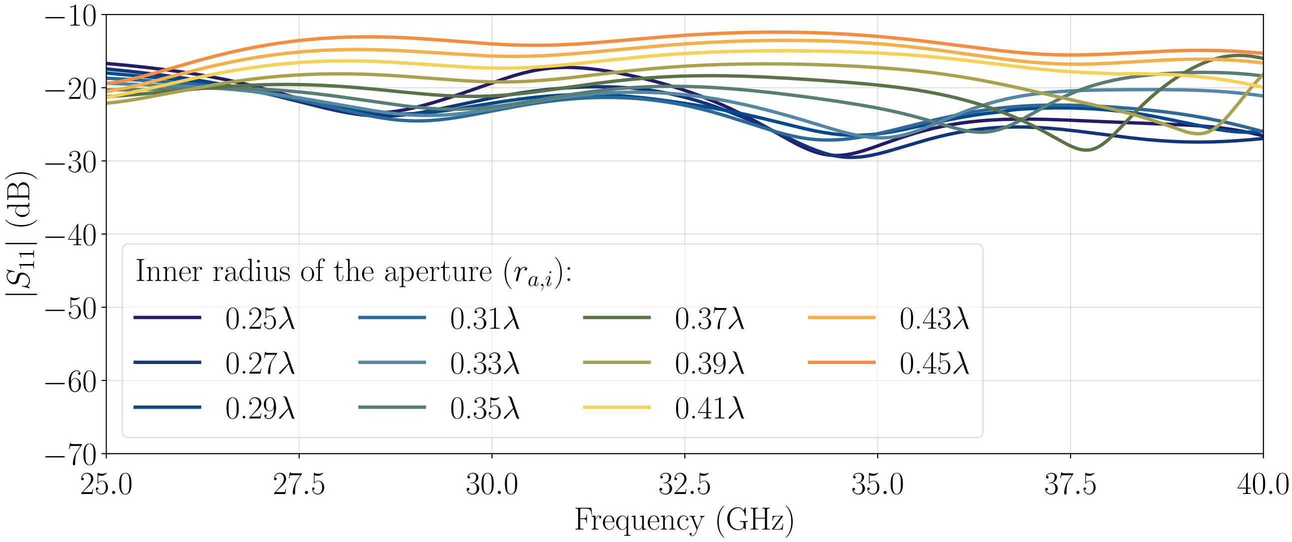

Source: Author.

Figure 40 – Reflection coefficients for analysed variations in the inner radius of the aperture ($r_{a,i}$), for an outer radius ($r_{a,o}$) of 0.88λ.

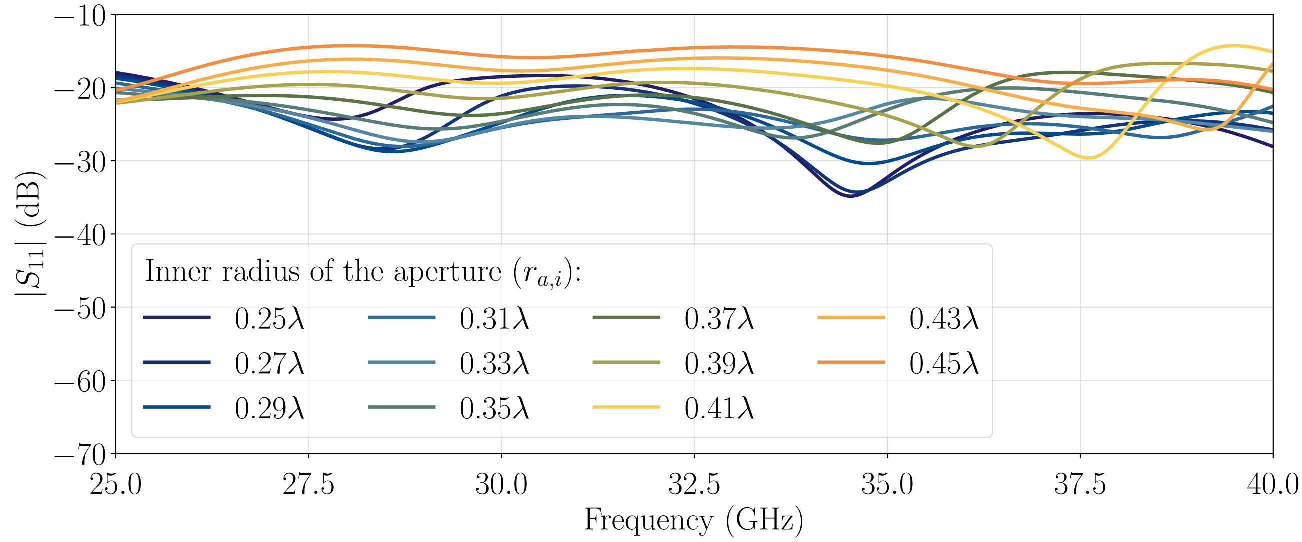

Source: Author.

Figure 41 – Reflection coefficients for analysed variations in the inner radius of the aperture ($r_{a,i}$), for an outer radius ($r_{a,o}$) of 0.92λ.

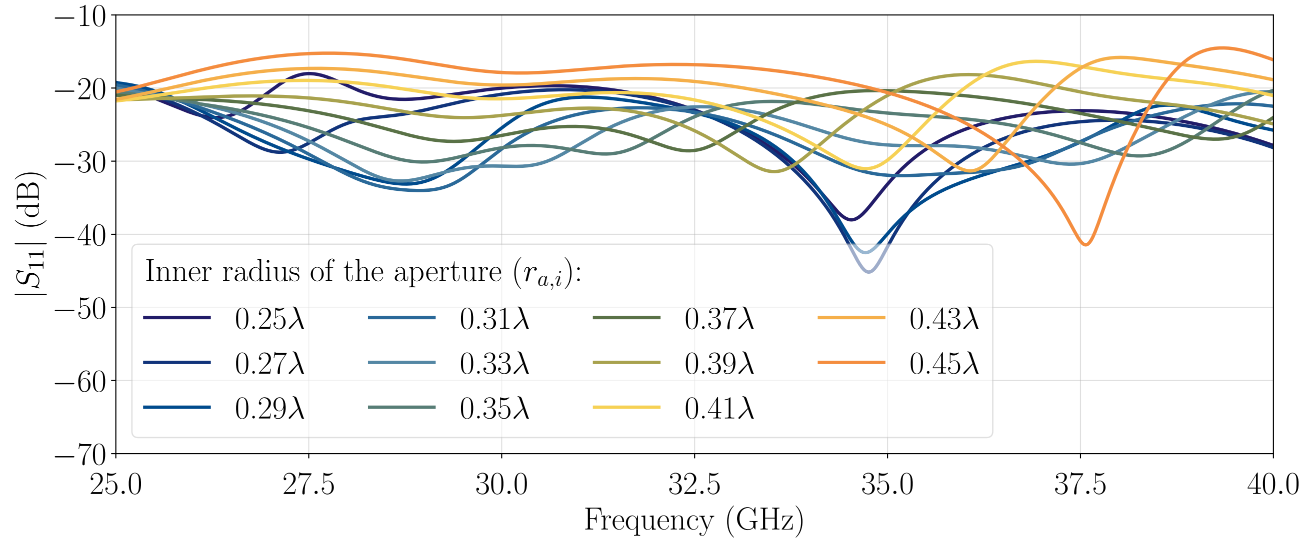

Source: Author.

Figure 42 – Reflection coefficients for analysed variations in the inner radius of the aperture ($r_{a,i}$), for an outer radius ($r_{a,o}$) of 0.96λ.

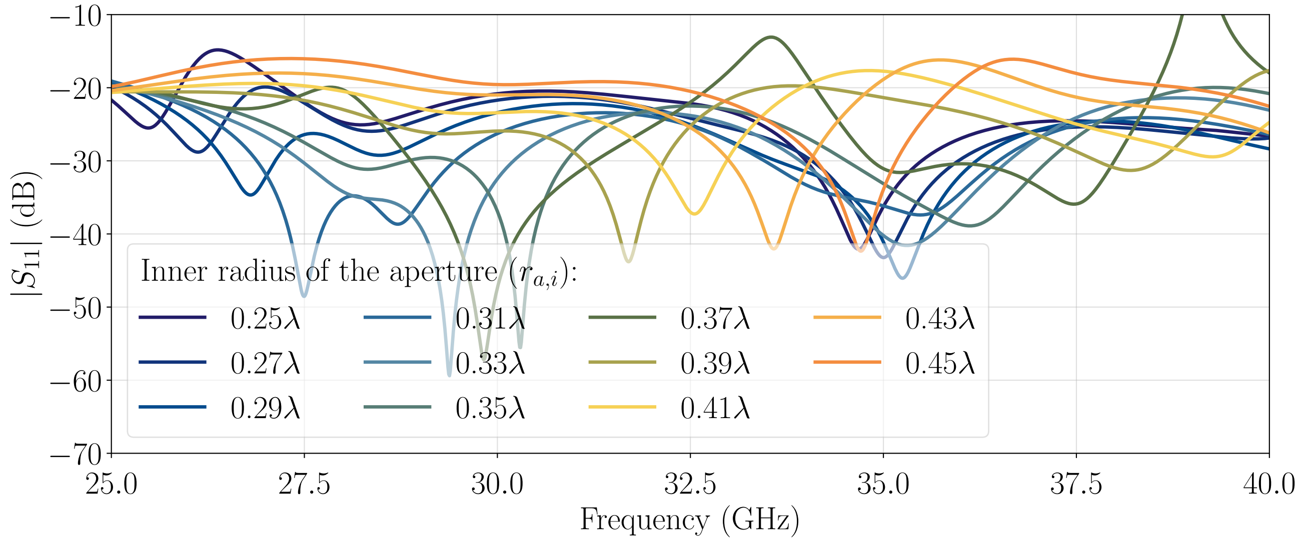

Source: Author.

Figure 43 – Reflection coefficients for analysed variations in the inner radius of the aperture ($r_{a,i}$), for an outer radius ($r_{a,o}$) of 0.98λ.

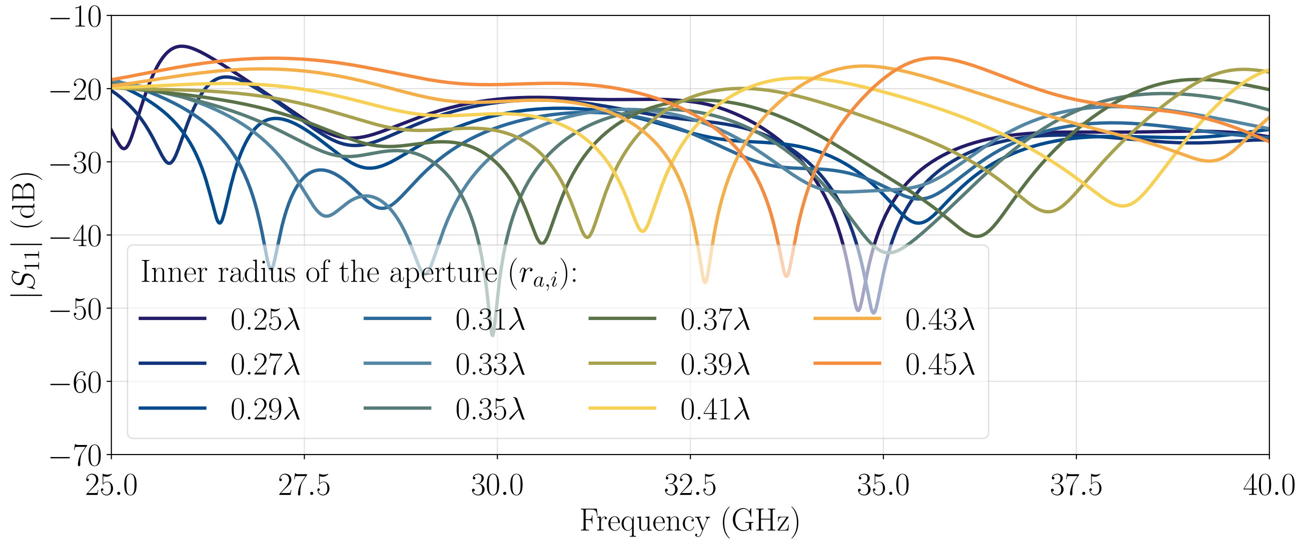

Source: Author.

Figure 44 – Radiation patterns for an inner radius of the aperture ($r_{a,i}$) of 0.25λ and an outer radius ($r_{a,o}$) of (a) 0.80λ, (b) 0.84λ, (c) 0.88λ, (d) 0.92λ, (e) 0.96λ, and (f) 0.98λ.

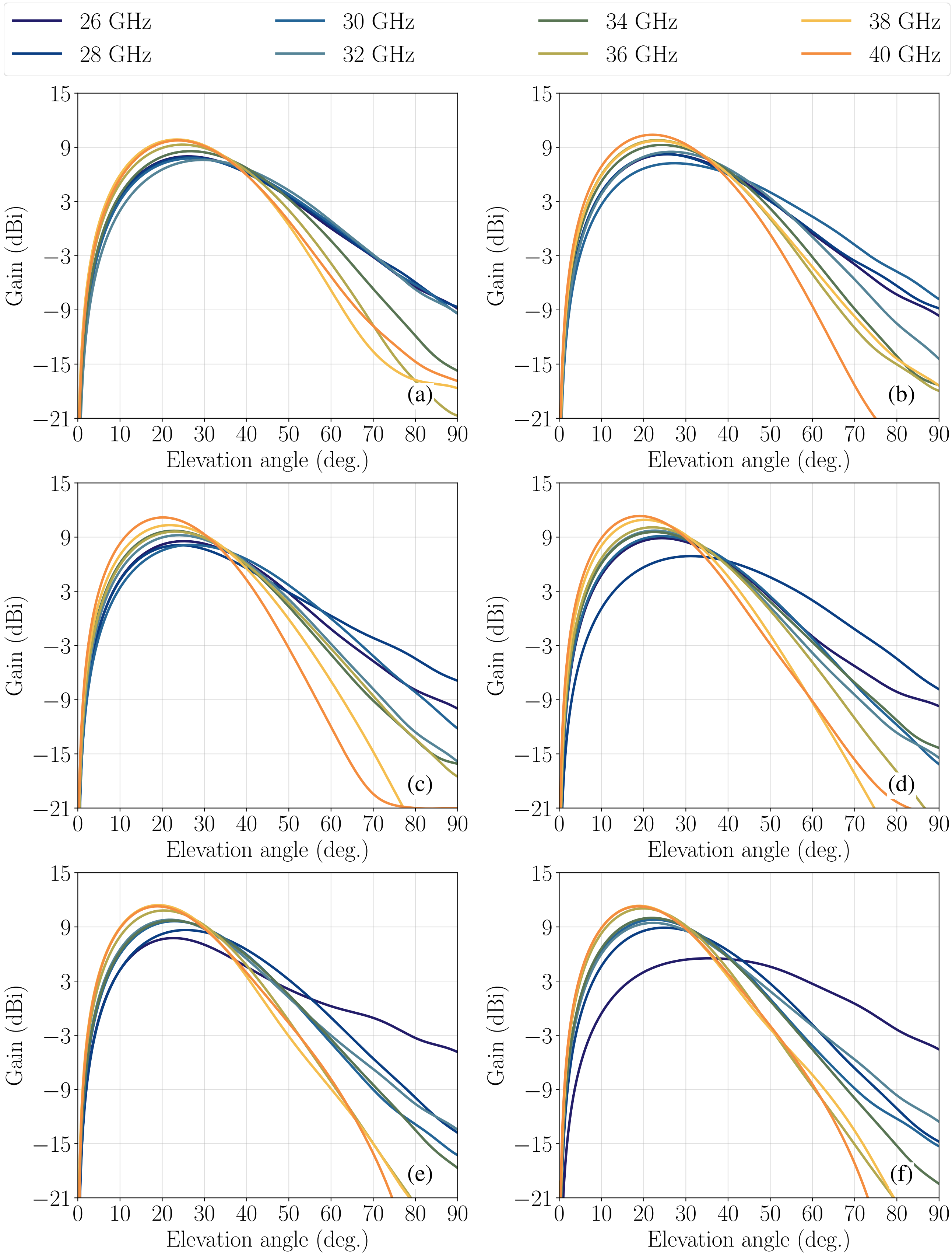

Source: Author.

Figure 45 – Radiation patterns for an inner radius of the aperture ($r_{a,i}$) of 0.35λ and an outer radius ($r_{a,o}$) of (a) 0.80λ, (b) 0.84λ, (c) 0.88λ, (d) 0.92λ, (e) 0.96λ, and (f) 0.98λ.

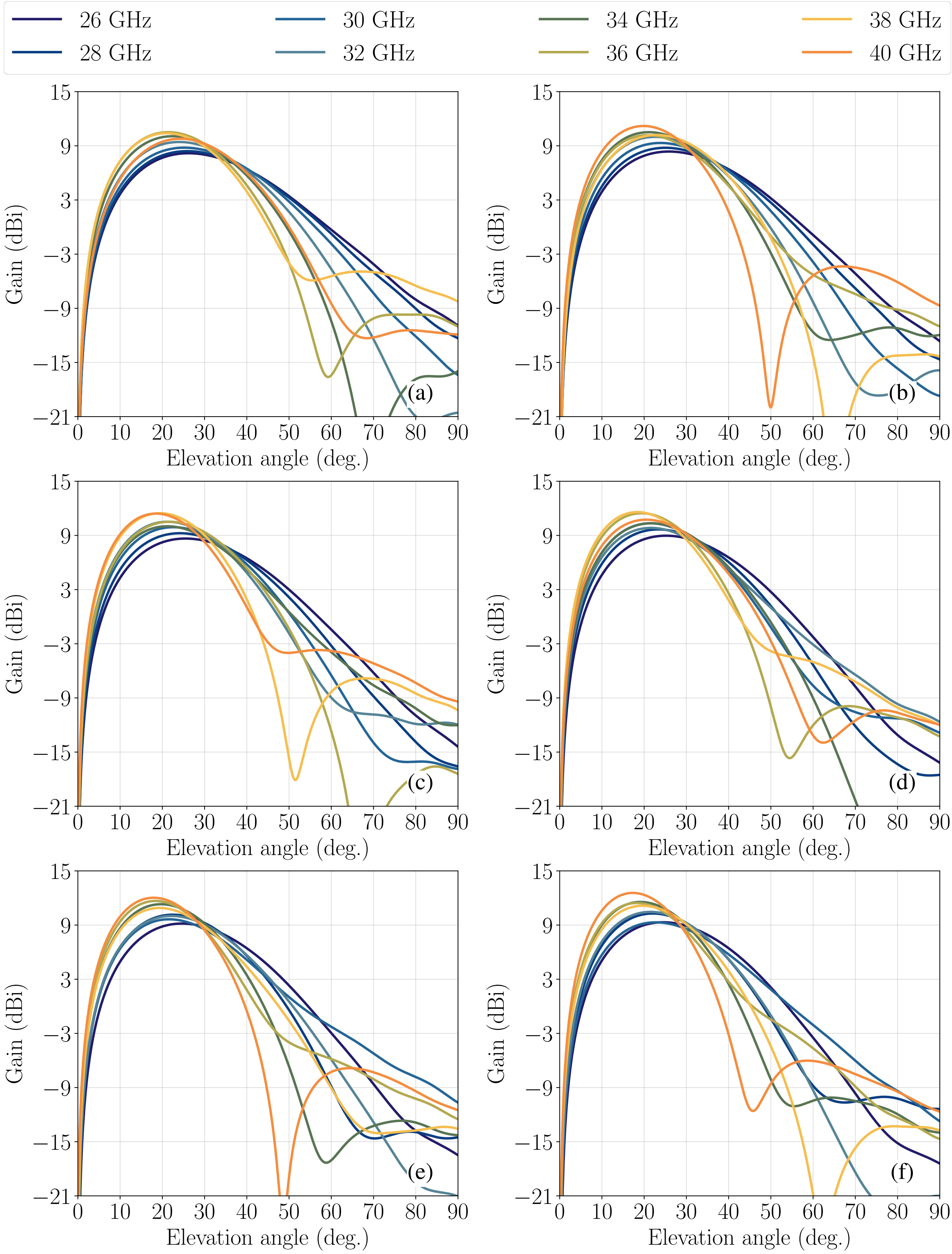

Source: Author.

Figure 46 – Radiation patterns for an inner radius of the aperture ($r_{a,i}$) of 0.45λ and an outer radius ($r_{a,o}$) of (a) 0.80λ, (b) 0.84λ, (c) 0.88λ, (d) 0.92λ, (e) 0.96λ, and (f) 0.98λ.

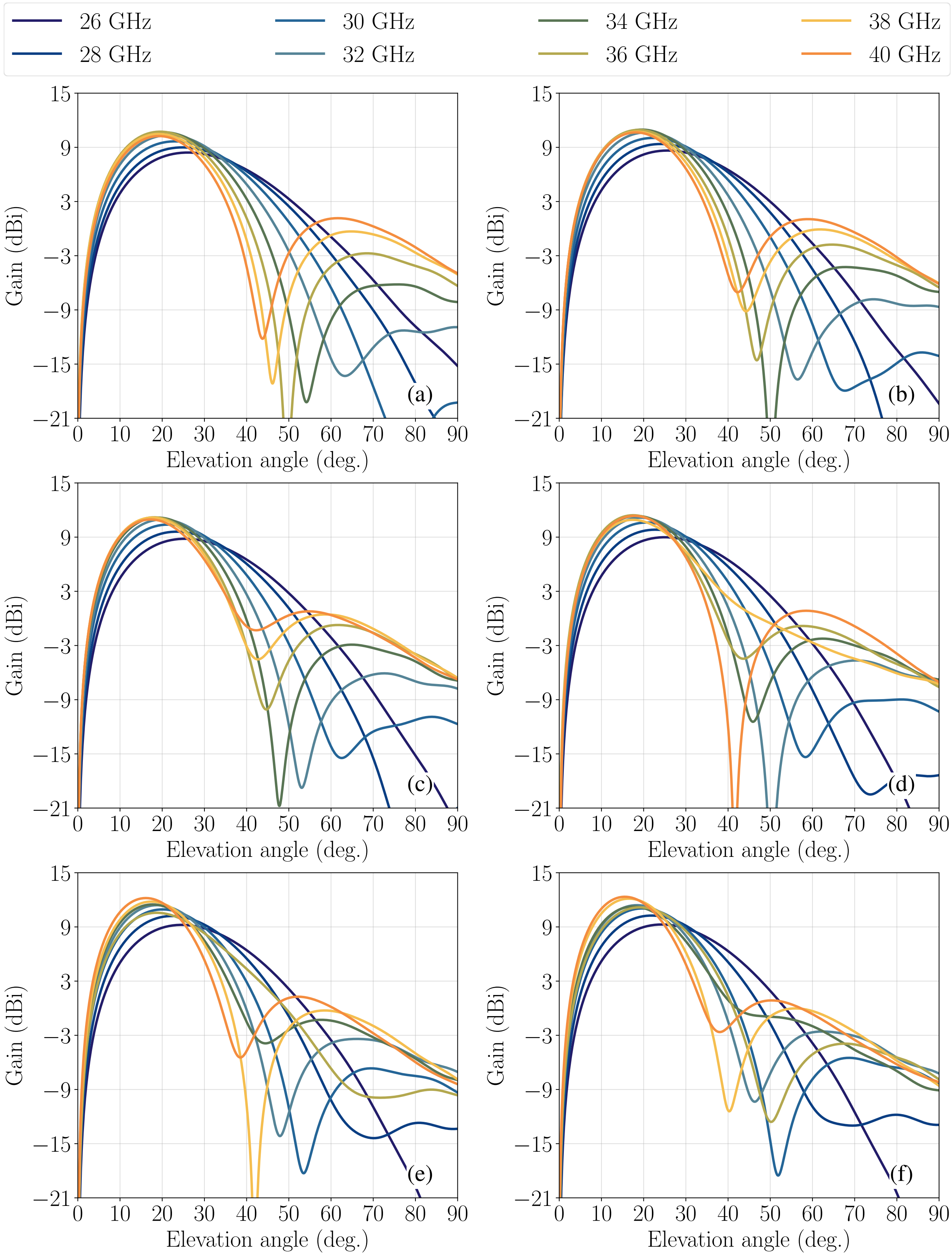

Source: Author.

APPENDIX B – DETAILED RESULTS FROM THE ANALYSES OF THE APERTURE'S RADII, FOR $\mathbf{r_{a,o}} > 1\lambda$

Figure 47 – Radiation patterns for an outer radius of the aperture ($r_{a,o}$) of (a) 0.96λ, (b) 1.10λ, (c) 1.25λ, (d) 1.40λ, (e) 1.55λ, (f) 1.70λ, (g) 1.85λ, and (h) 2.00λ.

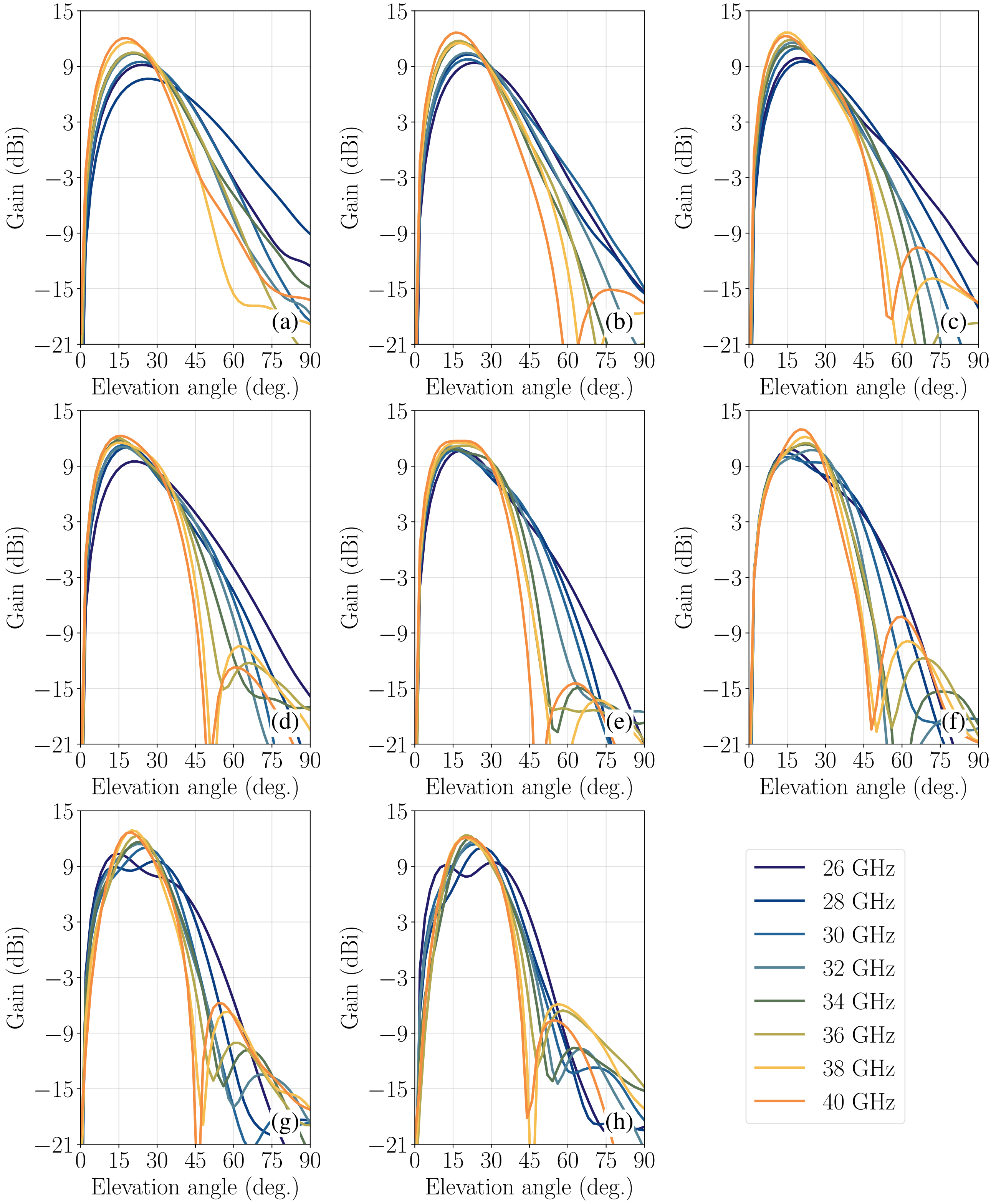

Source: Author.

Figure 48 – Radiation patterns for an outer radius of the aperture ($r_{a,o}$) of 1.10λ and an inner radius ($r_{a,i}$) of (a) 0.10λ, (b) 0.20λ, (c) 0.30λ, (d) 0.40λ, and (e) 0.50λ.

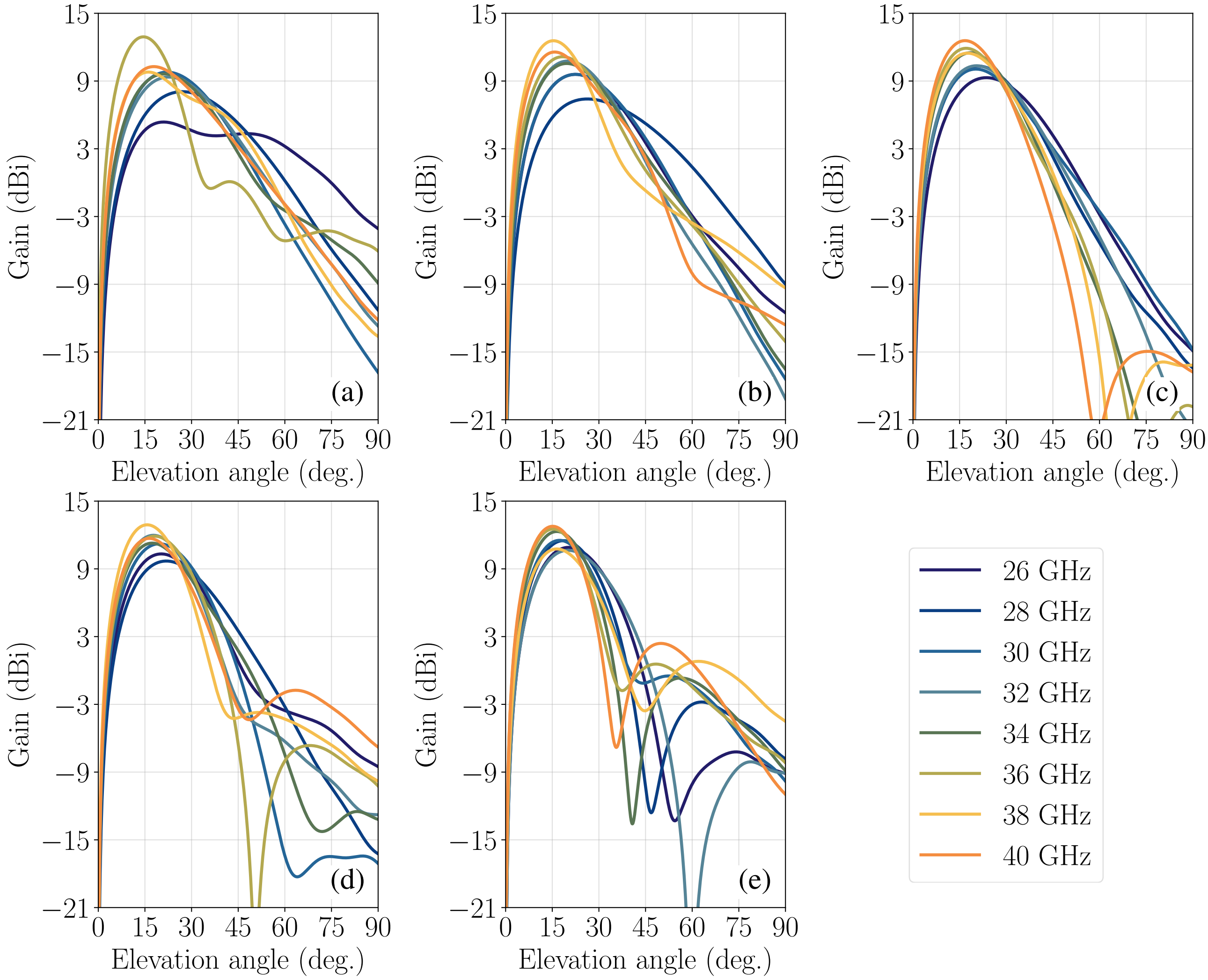

Source: Author.

Figure 49 – Radiation patterns for an outer radius of the aperture ($r_{a,o}$) of 1.25λ and an inner radius ($r_{a,i}$) of (a) 0.10λ, (b) 0.20λ, (c) 0.30λ, (d) 0.40λ, and (e) 0.50λ.

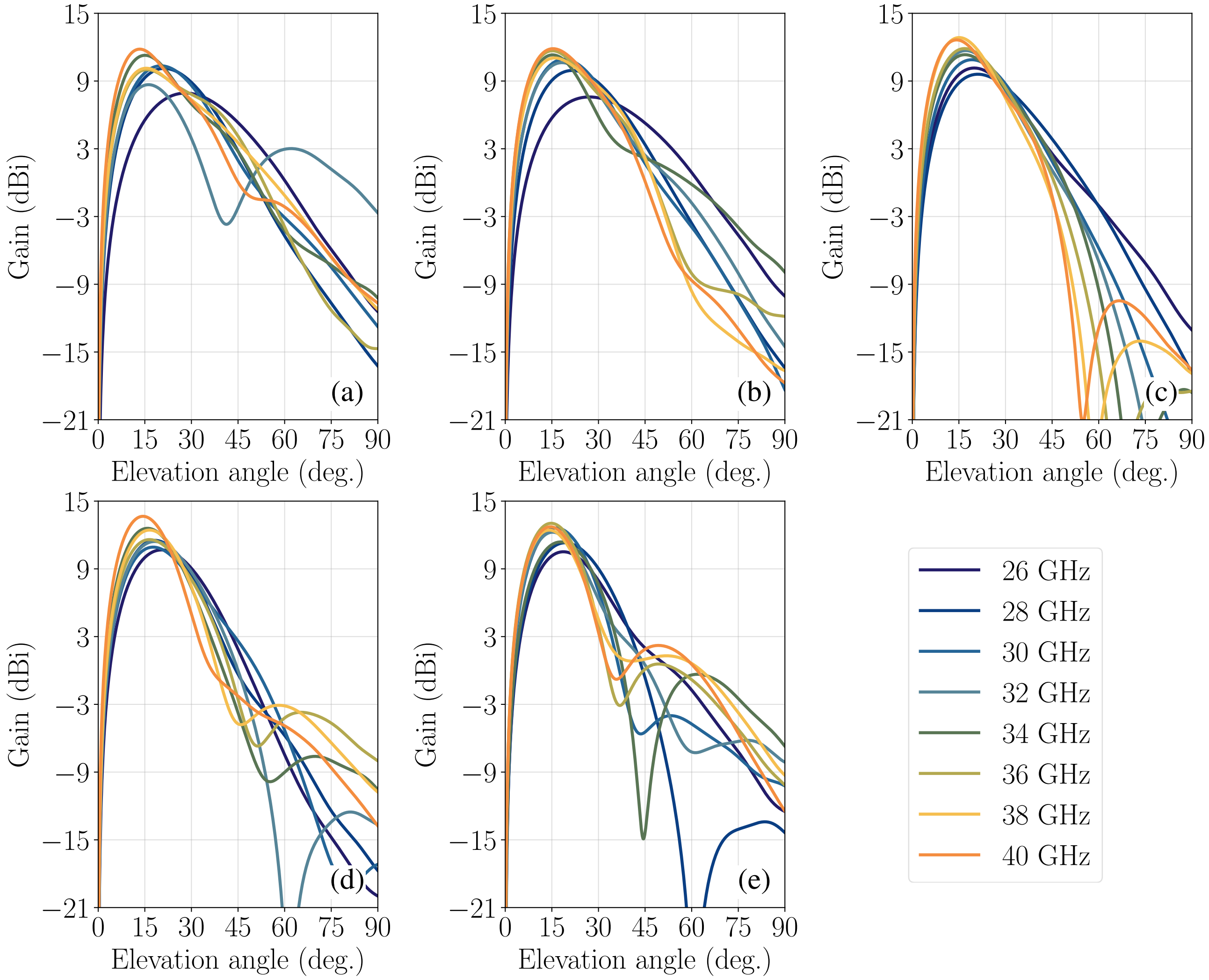

Source: Author.

Figure 50 – Radiation patterns for an outer radius of the aperture ($r_{a,o}$) of 1.40λ and an inner radius ($r_{a,i}$) of (a) 0.10λ, (b) 0.20λ, (c) 0.30λ, (d) 0.40λ, and (e) 0.50λ.

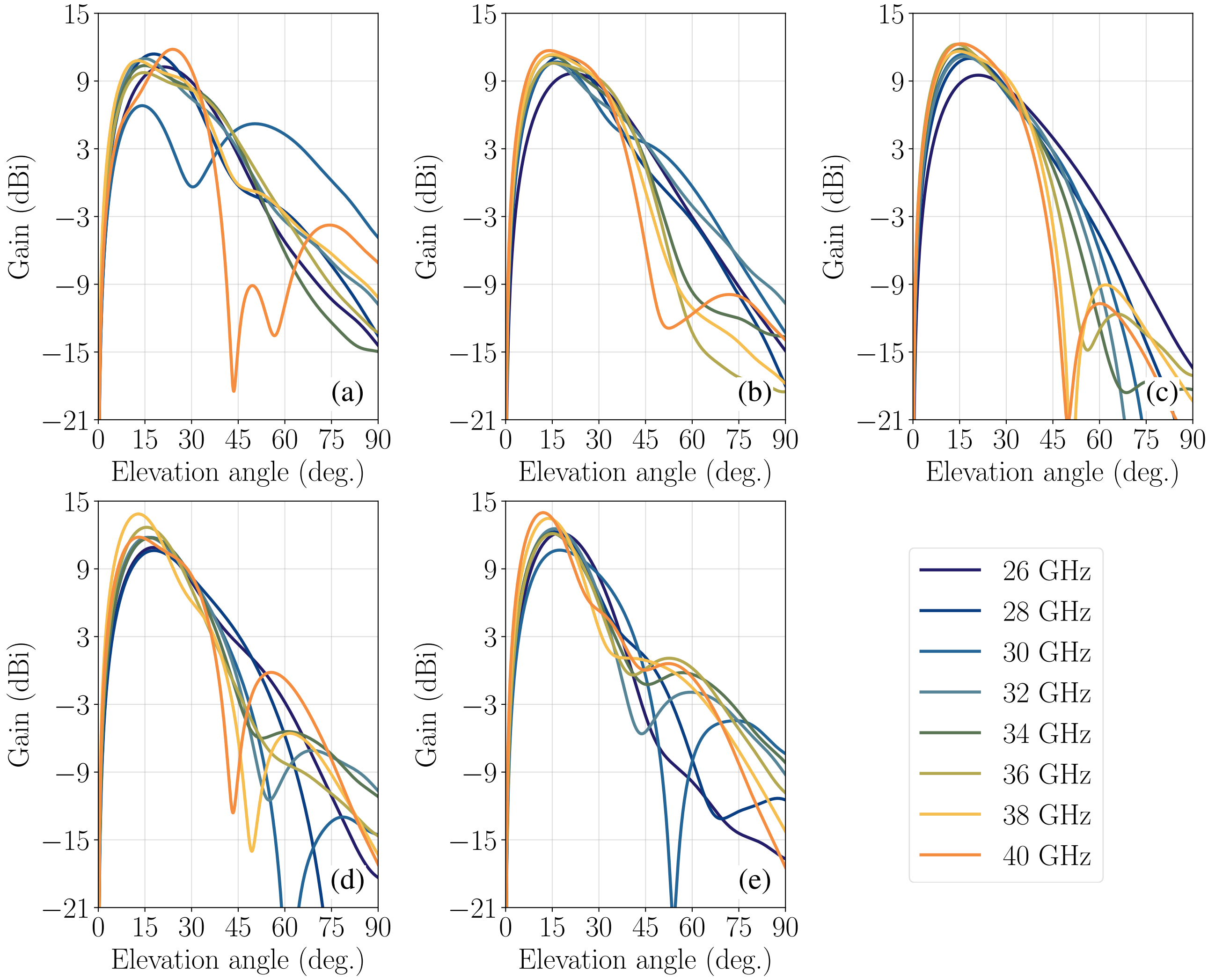

Source: Author.

Figure 51 – Radiation patterns for an outer radius of the aperture ($r_{a,o}$) of 1.55λ and an inner radius ($r_{a,i}$) of (a) 0.10λ, (b) 0.20λ, (c) 0.30λ, (d) 0.40λ, and (e) 0.50λ.

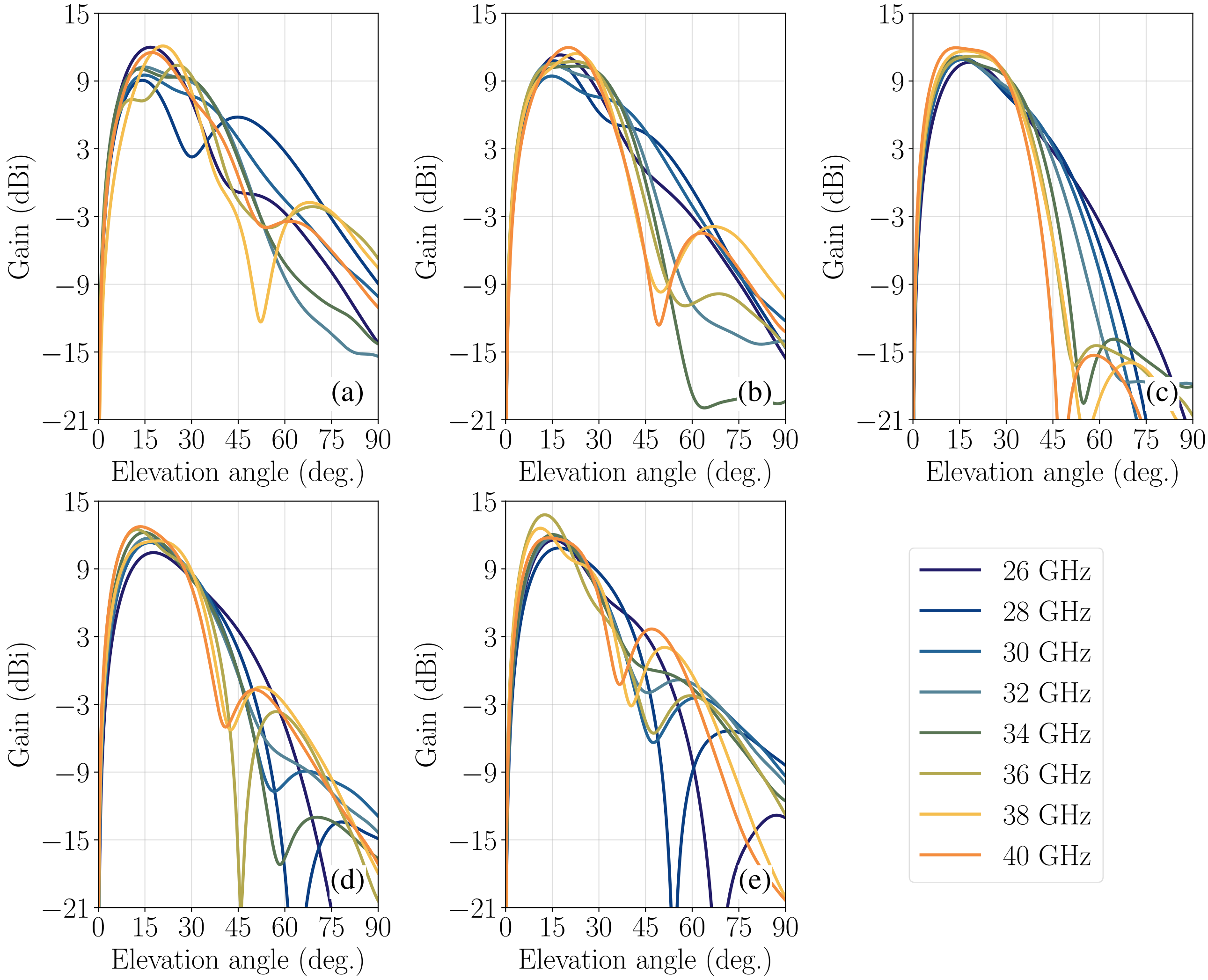

Source: Author.

APPENDIX C – DETAILED RESULTS FROM THE CHOKE-RING ANALYSIS

Figure 52 – Radiation patterns for a choke-ring depth (d) of (a) 1.45 mm, (b) 1.81 mm, (c) 2.17 mm, (d) 2.53 mm, (e) 2.89 mm, (f) 3.25 mm, (g) 3.61 mm, (h) 3.97 mm, and (i) 4.33 mm.

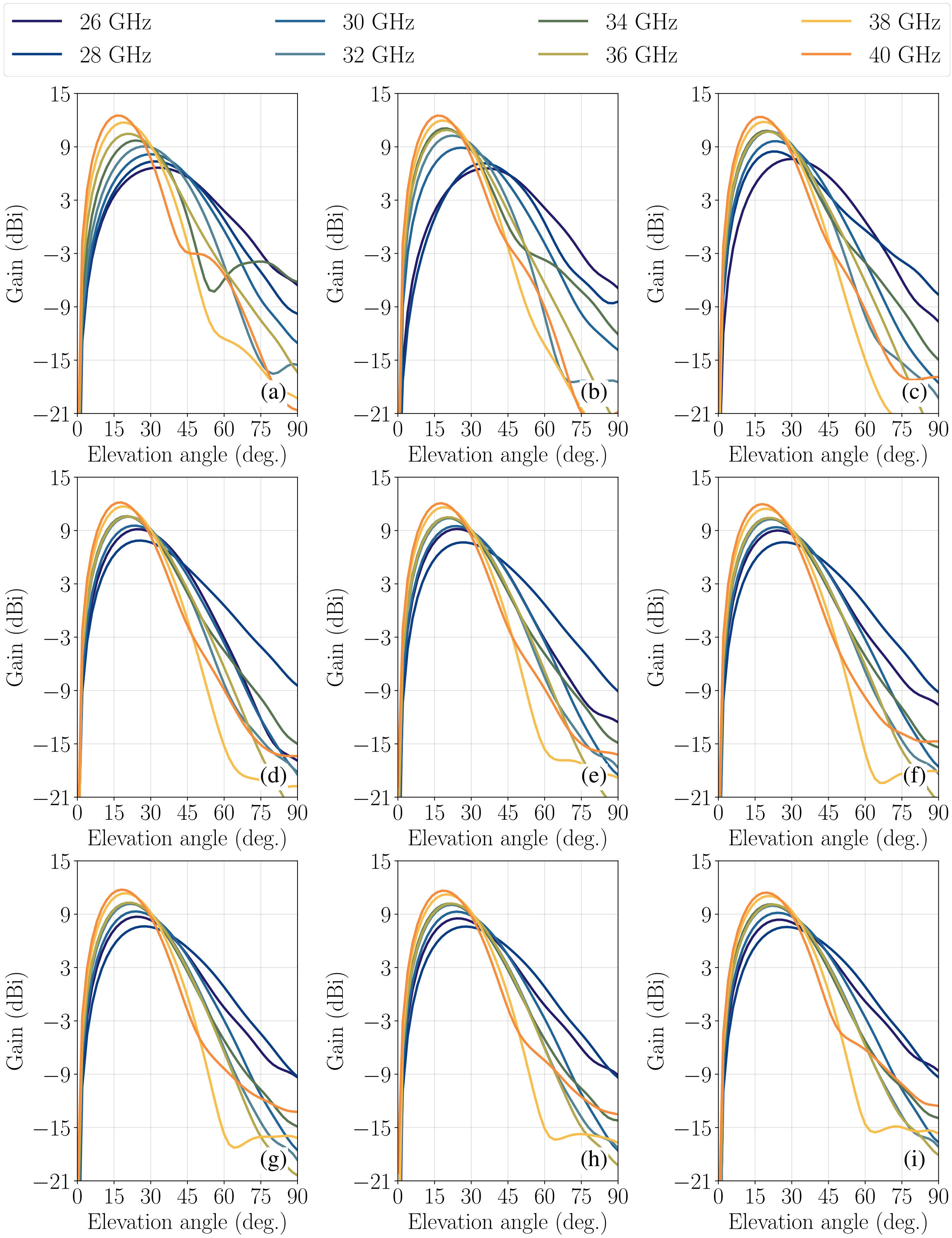

Source: Author.

Figure 53 – Radiation patterns for a width of the innermost section of the choke-ring (w_i) of (a) 0.2 mm, (b) 0.434 mm, (c) 0.6 mm, (d) 1 mm, (e) 1.4 mm, (f) 1.8 mm, (g) 2.2 mm, (h) 2.6 mm, and (i) 3 mm.

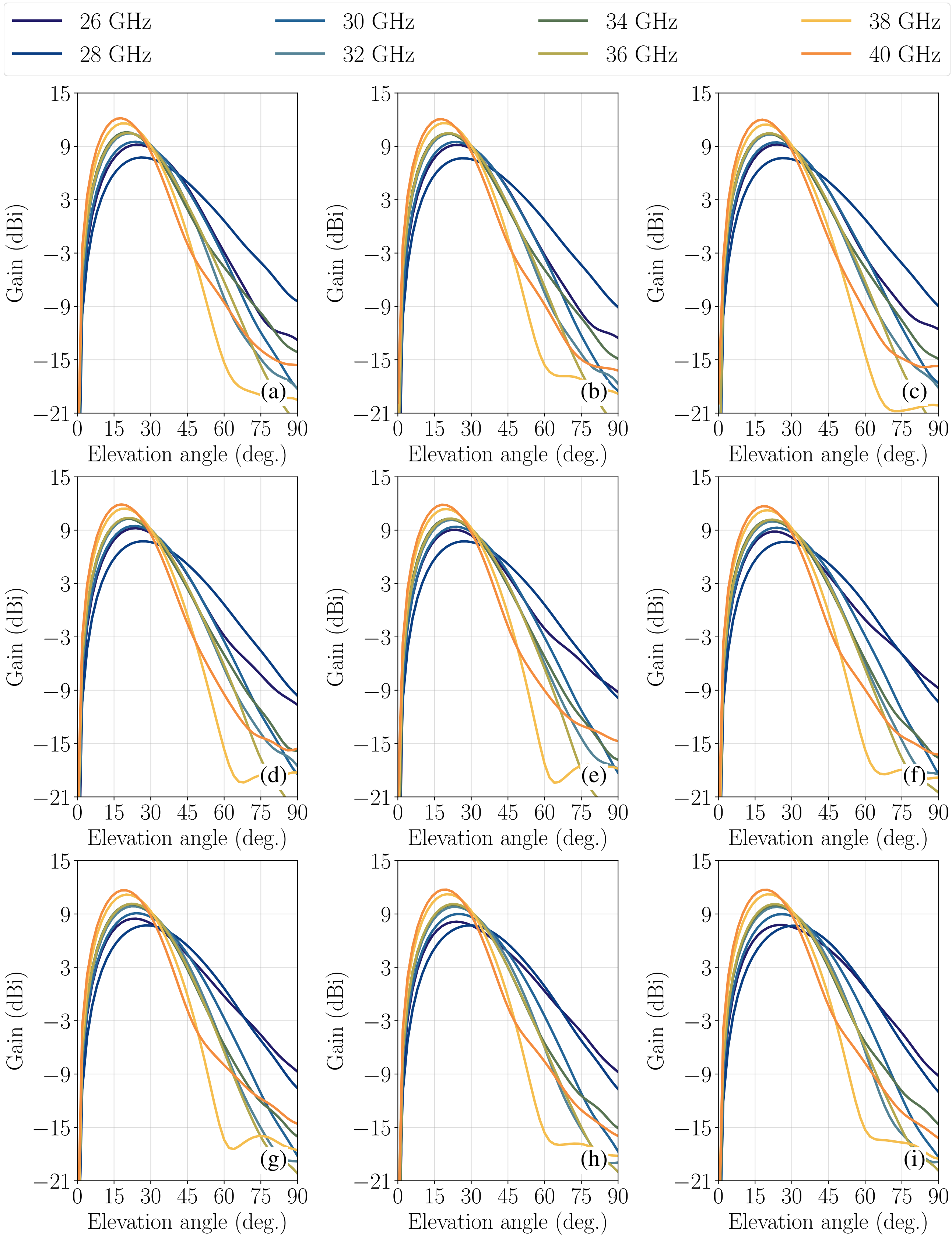

Source: Author.

Figure 54 – Radiation patterns for a width of the outermost section of the choke-ring (w_o) of (a) 0.6 mm, (b) 0.8 mm, (c) 1 mm, (d) 1.2 mm, (e) 1.232 mm, (f) 1.4 mm, (g) 1.6 mm, (h) 1.8 mm, and (i) 2 mm.

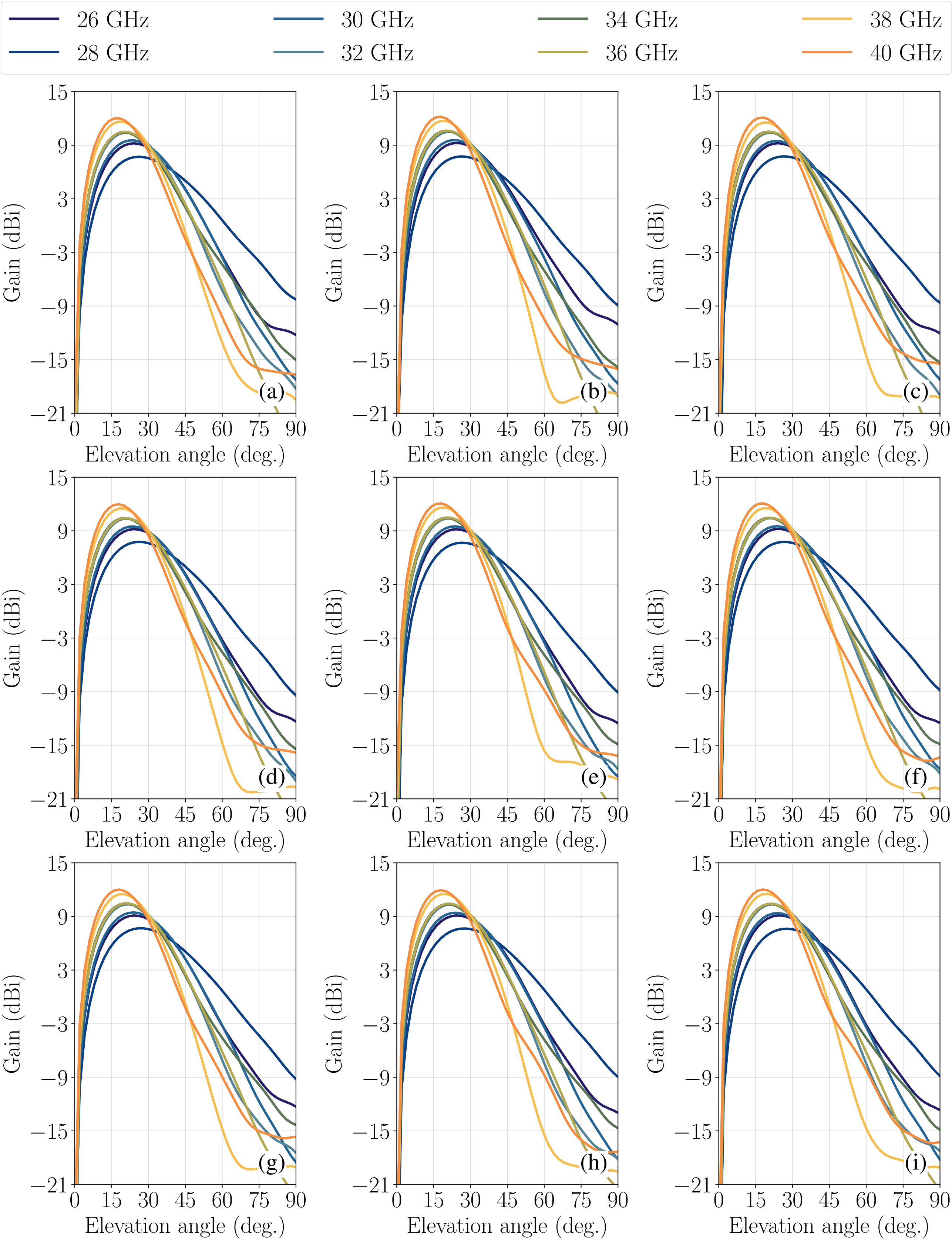

Source: Author.